Functional Soft Robotic Actuators Based on Dielectric Elastomers

THÈSE N^{O} 6855 (2016)

PRÉSENTÉE LE 29 JANVIER 2016

À LA FACULTÉ DES SCIENCES ET TECHNIQUES DE L'INGÉNIEUR
LABORATOIRE DE SYSTÈMES INTELLIGENTS
PROGRAMME DOCTORAL EN MICROSYSTÈMES ET MICROÉLECTRONIQUE

ÉCOLE POLYTECHNIQUE FÉDÉRALE DE LAUSANNE

POUR L'OBTENTION DU GRADE DE DOCTEUR ÈS SCIENCES

PAR

Jun SHINTAKE

acceptée sur proposition du jury:

Prof. S. Lacour, présidente du jury
Prof. D. Floreano, Prof. H. Shea, directeurs de thèse
Prof. S. Bauer, rapporteur
Prof. O. Brock, rapporteur
Prof. J. Paik, rapporteuse

ÉCOLE POLYTECHNIQUE
FÉDÉRALE DE LAUSANNE
Suisse
2016

Acknowledgements

I would like to thank my supervisors Prof. Dario Floreano and Prof. Herbert Shea. They gave me a great opportunity to work on the collaborative project, sensory-motor tissues for soft robots, between the Laboratory of Intelligent Systems and the Microsystems for Space Technologies Laboratory. During this four-year project, Dario and Herb were encouraging and supporting me with their supervision, ideas, and advises, and trying to patiently understand and solve problems together, while giving me a lot of freedom to work between the two labs. All the time they were believing me and positively thinking when my work did not progress.

I am grateful to Prof. Siegfried Bauer, Prof. Oliver Brock, and Prof. Jamie Paik for accepting to review and evaluate this thesis as the members of my jury, and Prof. Stéphanie Lacour for accepting to serve as the jury president.

I would like to thank Dr. Samuel Rosset and Dr. Bryan Schubert who helped me from the beginning of the project in many aspects. They were always stable like Swiss Alps when I was upset for facing research obstacles, and giving me ideas and suggestions countless times. We also had a lot of fun discussions including off research topics. I would also like to thank Dr. Stefano Mintchev for his kind support especially writing this thesis.

During the years, I got assistance from many people, and I would need another 100 pages to write everything. Particularly, I would like to thank Dr. Samin Akbari and Dr. Luc Maffli who trained me how to use equipment and to fabricate devices. I would also like to thank Dr. Subha Chakraborty who supported and taught me many things, not only research but also about life. I thank Dr. Oluwaseun Araromi and Dr. Daniel Courtney for their helpful and interesting discussions and advices that accelerated this project. I also thank Dr. Vinu Venkatraman for his help especially preparation until the midnight before the candidacy exam, and Philippe Vosseler at ACI for his cordial consultations about PCBs.

I thank my friends and lab members Felix, Trevis, Ramon, Iliya, Michal, Andrea, Géraud, Ludovic, Przemek, Greg, Joshua, Meysam, Giovanni, Nicolas, Julien, Maja, Basil, Alexandre C, Caglar, Ben, Kaustav, Tobias, Simon, Alexandre P, Nadine, Juan, Xiaobin, David, Dara, Yexian, Andres, Sara, Teru and many others for their help and the days we spent together. I also thank master students Geoffroy, William, and Benz who worked with me during semester projects. I am also grateful to Myriam Poliero, Michelle Wälti, Marie Halm, and Lucie Auberson for their kind help.

Finally, I would like to thank my parents and sisters for all the supports to get me here, and Naoko for her understanding, patience, and love.

Hamburg, October 1st 2015 J. S.

Abstract

Dielectric elastomer actuators (DEAs) are a promising soft actuator technology for robotics. Adding robotic functionalities—folding, variable stiffness, and adhesion—into their actuator design is a novel method to create functionalized robots with simplified actuator configurations. We first propose a foldable actuator that has a simple antagonistic DEA configuration allowing bidirectional actuation and passive folding. To prove the concept, a foldable elevon actuator with outline size of 70 mm × 130 mm is developed with a performance specification matched to a 400 mm wingspan micro air vehicle (MAV) of mass 130 g. The developed actuator exhibits actuation angles up to ± 26 ° and a torque of 2720 mN·mm in good agreement with a prediction model. During a flight, two of these integrated elevon actuators well controlled the MAV, as proven by a strong correlation of 0.7 between the control signal and the MAV motion. We next propose a variable stiffness actuator consisting of a pre-stretched DEA bonded on a low-melting-point alloy (LMPA) embedded silicone substrate. The phase of the LMPA changes between liquid and solid enabling variable stiffness of the structure, between soft and rigid states, while the DEA generates a bending actuation. A proof-of-concept actuator with dimension 40 mm length × 10 mm width × 1 mm thickness and a mass of 1 g is fabricated and characterized. Actuation is observed up to 47.5 ° angle and yielding up to 2.4 mN of force in the soft state. The stiffness in the rigid state is ~90 × larger than an actuator without LMPA. We develop a two-finger gripper in which the actuators act as the fingers. The rigid state allows picking up an object mass of 11 g (108 mN), to be picked up even though the actuated grasping force is only 2.4 mN. We finally propose an electroadhesion actuator that has a DEA design simultaneously maximizing electroadhesion and electrostatic actuation, while allowing self-sensing by employing an interdigitated electrode geometry. The concept is validated through development of a two-finger soft gripper, and experimental samples are characterized to address an optimal design. We observe that the proposed DEA design generates 10 × larger electroadhesion force compared to a conventional DEA design, equating to a gripper with a high holding force (3.5 N shear force for 1 cm^2) yet a low grasping force (1 mN). These features make the developed simple gripper to handle a wide range of challenging objects such as highly-deformable water balloons (35.6 g), flat paper (0.8 g), and a raw chicken egg (60.9 g), with its lightweight (1.5 g) and fast movement (100 ms to close fingers). The results in this thesis address the creation of the functionalized robots and expanding the use of DEAs in robotics.

Key words: dielectric elastomer actuators, functional actuators, robotics, soft robotics, aerial robots, grippers, folding, variable stiffness, adhesion

Résumé

Les actionneurs élastomères diélectriques (DEAs) sont une technologie prometteuse d'actionneurs souples pour la robotique. L'ajout de fonctionnalités telles que le pliage, la rigidité variable, et l'adhérence dans la conception de ces actionneurs est une nouvelle façon des créer des robots qui mène à des configurations simplifiées d'actionneurs. Tout d'abord, nous proposons un actionneur pliable qui a une simple configuration DEA antagoniste permettant un actionnement bidirectionnel et un pliage passif. Pour prouver le concept, un actionneur d'élevon pliable avec une taille extérieur de 70 mm × 130 mm est développé avec une spécification de performance adaptée à un micro véhicule aérien (MAV) de 400 mm d'envergure et d'une masse de 130 g. L'actionneur développé permet un angle d'actionnement jusqu'à ± 26 ° et un couple allant jusqu'à 2720 mN·mm en bon accord avec un modèle de prédiction. Lors d'un vol, deux de ces actionneurs intégrés d'élevons contrôlaient le MAV, comme le prouva une forte corrélation de 0.7 entre le signal de commande et le mouvement du MAV. Nous proposons ensuite un actionneur à rigidité variable constitué d'un DEA pré-étiré collé sur un alliage à faible point de fusion (LMPA) dans un substrat de silicone. Un actionneur pour prouver le concept est fabriqué et caractérisé avec des dimensions de 40 mm de longueur × 10 mm de largeur × 1 mm d'épaisseur et une masse de 1 g. L'actionnement a été observée jusqu'à 47.5 ° d'angle et donnant jusqu'à 2.4 mN de force dans l'état souple. A l'état rigide, la rigidité était 90× plus grand qu'un actionneur sans LMPA. Nous développons une pince robotique à deux doigts dans laquelle les actionneurs agissent comme les doigts. L'état rigide permet de un soulever un objet d'une masse de 11 g (108 mN) même si la force de serrage de l'actionnement est seulement de 2.4 mN. Enfin, nous proposons un actionneur électro-adhésif qui a une conception DEA maximisant simultanément l'électro-adhésion et l'actionnement électrostatique, tout en permettant une auto-détection. Le concept est prouvé par le développement d'un préhenseur souple à deux doigts, et des échantillons expérimentaux sont caractérisés pour avoir une conception optimale. Nous observons que la conception DEA proposé génère une force d'électro-adhésion 10× plus grand par rapport à une conception DEA conventionnelle, ce qui équivaut à une pince robotique avec une force de maintien élevée (3.5 N de force de cisaillement pour 1 cm^2) même si la force de préhension est encore faible (1 mN). Ces caractéristiques permettent à la simple pince robotique de manipuler une large gamme d'objets difficiles. Les résultats de cette thèse portent sur la création de robots fonctionnalisés et l'expansion de l'utilisation de DEAs en robotique.

Mots clefs : actionneurs élastomères diélectriques, actionneurs fonctionnels, robotique, robotique souple, robots aériens, pinces robotique, pliage, raideur variable, adhérence

Contents

List of Figures

List of Tables

1 Introduction

Dielectric elastomer actuators (DEAs) are a promising soft actuator technology for robotics. Their natural muscle like characteristics such as high compliance and large actuation strain encourages applying the technology to robots, and could make them bio-inspired and adaptable to human and unstructured environments. High energy density (or specific power) and efficiency are expected to enable lightweight, compact mobile robots with extended activity time. Fast response allows operation of those applications in a wide speed range, and smart characteristics such as self-sensing capability could lead to highly integrated systems. The structure of DEAs is simple, and with the high compliance, this feature could make actuation mechanisms and robots mechanically robust against shocks and over loads, compared to conventional approach that consists of rigid parts such as motors, gears, and linkages. The structural simplicity of DEAs has enabled their implementation to actuator configurations in many different ways, and accelerated developments.

Actuator configuration is essential for most of DEAs. Because DEAs are thin and compliant, a tailored configuration is necessary to output mechanical actuation that is effectively oriented, and/or to achieve required high stress (or force) where many DEA layers are stacked, as usually DEAs generate low stress. While most of the developed configurations have design only to perform an actuation, a novel approach is to add robotic functionalities into the actuator design, which contributes to enhance robot characteristics and performances while avoiding complexity.

Three representative robotic functionalities are considered: folding, variable stiffness, and adhesion. Folding functionality makes robots to reconfigure their shape [197]. Such foldable robots can self-assemble to automate their fabrication [212], and change their feature size or volume, so that compact for improving portability [231], or decreasing drag of a deployable wing in jump-glide transition [230]. The foldability also allows robots to perform different locomotion strategies adapted to environments [229]. Variable stiffness (or controllable stiffness) functionality enables safe human-robot interaction in conventional robots using electromagnetic motors and the rigid parts, by giving variable mechanical impedance [1]. In robotic systems based on soft actuators, variable stiffness functionality changes the elastic modulus of the structure, and is expected to allow the robots to exert intentional forces to environments, and withstand external loads while keeping their structural shape that usually passively deforms [255, 268]. An example of application is grippers, where the object (i.e.,

external load) heavier than the actuated grasping force can be held by stiffened fingers. Here, the essential effect of variable stiffness is alternating the high holding force, and minimizes the actuation force required to grasp the object. Adhesion functionality yields an attractive force at the interface between robots and external objects. Gecko-inspired robots and crawler robots are a good example [302, 297]. The presence of the adhesion force unleashes terrestrial robot from gravity constraint to move around vertical wall and ceiling. The adhesion also makes grippers to hold the object with minimized grasping force by relying on shear friction force [305, 299], which may allow the devices to handle for example sensitive objects.

In general, equivalent characteristics and performances of the functionalized robots described above may be achieved by additive strategies, without any specialized DEA configurations. For example, foldable robots could be constructed using actuators with a usual configuration and additional mechanisms enabling folding like joints. Desired holding force of grippers could be achieved by stacking many DEA layers. However, those additive applications and actuator configurations may be bulky, resulting in difficulty and complexity on designing (e.g., shape and size) and fabrication. Adding functionalities directly to the actuator design simplifies the configurations therefore their applications. Obviously, an intrinsically foldable actuator does not require the additional mechanisms for folding. As previously mentioned, variable stiffness and electroadhesion allow to minimize the actuated grasping force while ensuring a high holding force. This functional feature allows DEA configurations with simplified form, because the same force provided from many DEA layers could be achieved by a few or a single layer.

Actuators with the three robotic functionalities—folding, variable stiffness, and adhesion—will expand the use of DEAs in robotics as a method to create the functionalized robots with simplified actuator configurations. This thesis is to investigate functional soft robotic actuators based on DEAs through the development of three actuators corresponding to each functionality. An actuator should address its practical use for real application. For every actuator, we propose, fabricate, characterize, and test in a specific application.

1.1 Contributions

This thesis builds on the field of DEAs.

- Chapter 2 reviews and discusses on the state of the art of soft actuator technologies. The technologies considered are shape memory alloys, pneumatic elastomeric actuators, ionic polymer-metal composites, and DEAs.
- Chapter 3 reviews the operating principles of DEAs and discusses the state of the art.
- Chapter 4 develops an actuator with folding functionality. State of the art of folding functionality in robotics is reviewed and discussed. The actuator concept is validated through development of a fixed wing micro air vehicle (MAV), in which two folding actuators are used as elevons. Concept, an analytical model, and fabrication of the actuator are described. Actuation characteristics of the fabricated elevon actuator such as displacement and torque are reported and discussed. MAV design, system, and control strategy are detailed. Evaluation result of the actuator in terms of the controllability of the MAV during a flight is reported and discussed. Potential robotic applications based on the developed technology is also discussed.
- Chapter 5 develops an actuator with integrated variable stiffness functionality. State of the art of variable stiffness functionality for soft robotics is reviewed and discussed. Concept, working principle, and fabrication of the actuator are described. Actuation characteristics of the fabricated actuator such as stroke, force, their repeatability, and stiffness (spring constant) are reported and discussed. A two-finger gripper developed for demonstration of a practical use of the actuator is detailed, and evaluation result on handling of an object is reported. Potential robotic applications based on the developed technology is discussed.
- Chapter 6 develops an actuator with electroadhesion functionality. The actuator concept is validated through development of a two-finger soft gripper. State of the art of robotic grippers focused on their versatility, and electroadhesion and other adhesion technologies are reviewed and discussed. Concept and working principle of the actuator are described. Fabrication of experimental samples and the gripper is detailed. Active characteristics of the experimental samples such as local and total electroadhesion forces, stroke, mechanical force are reported and discussed. The developed gripper is detailed, and evaluation result on handling objects of different types is reported and discussed. Potential robotic applications based on the developed technology is also discussed.
- Chapter 7 concludes all the results and addresses future work.

2 Soft Actuator Technologies

This chapter reviews and discusses on the state of the art of soft actuator technologies. A number of actuators exist, but most of robotic applications are based on three soft actuator technologies: shape memory alloys (SMAs), pneumatic elastomeric actuators, and electroactive polymers (EAPs). SMAs recover their original shape from a plastic deformation in response to a thermal stimulus. There are also shape memory polymers (SMPs) that have similar characteristics. However, SMPs are not employed for primary actuation of robotic systems. They are used as a variable stiffness mechanism [267] and the one-time folding of some robotic structures [212]. Pneumatic elastomeric actuators change their shape or size in response to fluidic pressure. EAPs are polymers that exhibit deformations in response to an electric stimulus. The deformations result from coulomb forces, electric fields, or relocation of ions. Two categories exist for EAPs: ionic EAPs and electronic EAPs. Ionic EAPs such as ionic polymer-metal composites (IPMCs), as well as electronic EAPs such as dielectric elastomer actuators (DEAs) are the primary EAPs that have been used for robotic applications. Consequently, other EAPs such as conducting polymers, ionic polymer gels, piezoelectric polymers, electrostrictive polymers, and liquid-crystal elastomers will be omitted from further discussion.

2.1 Shape Memory Alloys (SMAs)

Shape memory alloys (SMAs) [2] work by transformation of their crystal structure in response to temperature. At low temperature, they have a martensitic structure that changes to an austenite structure at high temperature. When the alloy is deformed at low temperature, the material returns to its original shape upon heating (Figure 2.1). This phenomenon is called the shape memory effect, and can be used as a form of actuation.

SMAs exhibit high stress (e.g., 230 MPa [4]) with substantial strains up to 5 % [4]. Nickel titanium (NiTi) is the most commonly used alloy in this type of actuator. NiTi alloys have a high elastic modulus (28-41 GPa for martensite, and 83 GPa for austenite [6]). However, as shown in Figure 2.2(a), when it is formed into a spring with a wire diameter of 25-500 μm, SMAs can provide compliance and a large actuation strain (e.g., 50 % linear contraction reported [7]). Behavior of the SMA spring is shown in Figure 2.1. NiTi alloys are conductive, allowing direct Joule-heating, and they are also biocompatible. The response speed is relatively slow (~10 Hz) due to the thermally-activated phase change, and there is hysteresis across actuation cycles. SMAs can be driven with low voltage, but they require high current and provide low efficiency.

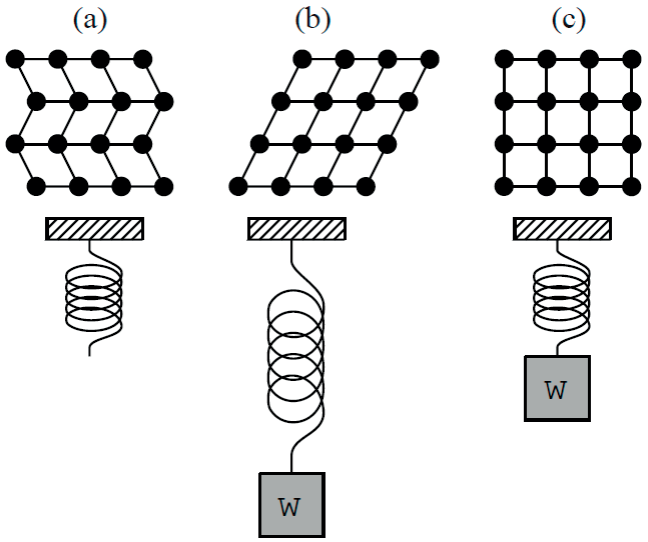

Figure 2.1 – Working mechanism of SMAs, adopted from [3]. Top row shows crystal structure of the material at different states. (a) Undeformed SMA spring at low temperature in martensite state. (b) Deformed SMA spring at low temperature in martensite state. (c) SMA apring at high temperature in austenite state.

The thermoelastic behavior of SMAs may also be affected by the external environment. In addition, SMAs have self-sensing capability [5].

SMAs have been widely applied in robotic applications from an underwater walker [8] to a miniature flying robot [9]. Many bio-inspired robots have been developed. They are mimicking the motions of inchworms [10, 11], fish [12], octopus-arms [13], jellyfish [14], manta rays [15], turtles [16], and bat-wings [17]. Figure 2.2(b) shows an inchworm robot consisting of a mesh tube surrounded by an SMA spring. The compliance of the spring shows a resistance to external shock. Figure 2.2(c) is a jellyfish robot. SMAs are integrated in the silicone-based bell. The high actuation stress of the actuator enables jumping [18], even from the water's surface [19]. The small size of SMAs allows their implementation in millimeter-scale robots [217], low-profile robots [220], and endoscopes [20] as well as manipulation devices such as a robotic hand [21].

2.2 Pneumatic Elastomeric Actuators

Pneumatic artificial muscles [38] (PAMs, also known as McKibben artificial muscles) linearly contract like human muscle when pressurized due to the radial change of an inextensible mesh surrounding a rubber inner bladder. Recently, a new class of pneumatic actuators, pneumatic elastomeric actuators, have been developed. This type of actuator has a homogeneous silicone matrix with embedded chambers (PneuNets [315]), a paper origami structure [201], or reinforcing fibers [39]. Depending on their structural configuration, different actuation behaviors can be achieved, such as bending, contraction, and extension. Figure 2.3 shows the working mechanism of PneuNets actuators. The actuator is often combined with an

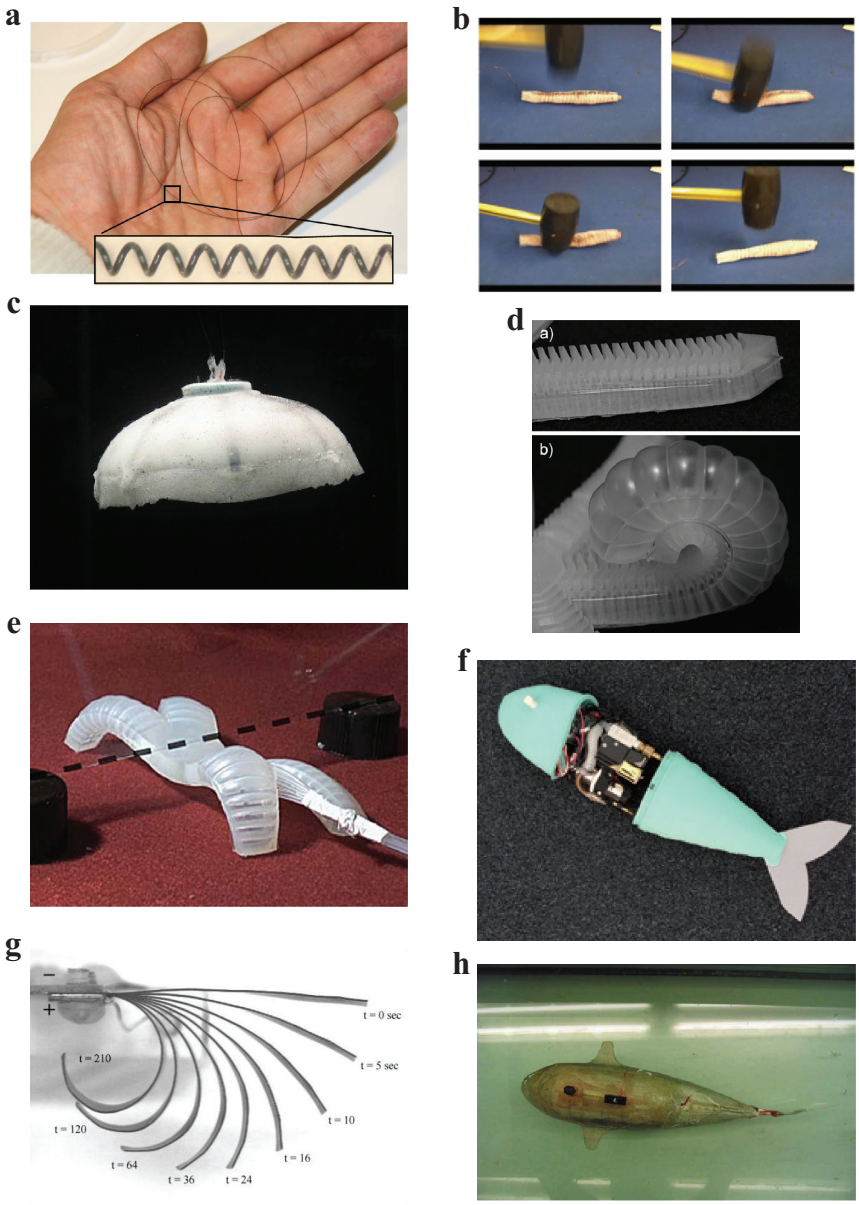

Figure 2.2 – Soft actuator technologies and their robotic applications. (a) An SMA spring actuator (NiTi) [7]. (b) An inchworm robot using an SMA spring actuator [11]. The robot consists of a mesh tube surrounded by the actuator, and it exhibits resistance to external shock. (c) A jellyfish robot using SMA [14]. (d) A pneumatic elastomeric actuator showing bending motion [315]. The actuator shown here is the finger of a 9 cm diameter gripper. (e) A legged robot using a pneumatic elastomeric actuator [326] (~15 cm long). The robot is able to crawl through a narrow gap by changing its gait pattern. (f) An untethered fish robot using pneumatic elastomeric actuators [46]. (g) An IPMC actuator exhibiting bending motion (applied voltage 3 V) [26]. (h) An untethered fish robot using an IPMC actuator. The actuator is placed in the root of the tail [28].

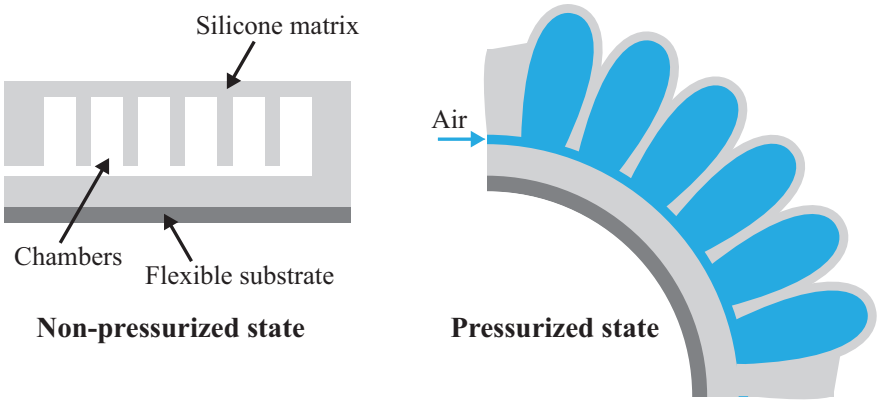

Figure 2.3 – Working mechanism of a pneumatic elastomeric actuator (PneuNets). Pressuring the structure inflates the chambers anisotropically, leading to a bending motion.

inextensible, flexible substrate. When pressured with fluid (mostly air), the chambers inflate, resulting in an anisotropic bending motion. Figure 2.2(d) shows a real PneuNets actuator exhibiting bending motion [315].

Pneumatic elastomeric actuators can be formed with varied geometries and materials, and their actuation characteristics change from one type to another with driving pressure. It is difficult to have representative characteristics for comparison with other soft actuator technologies. However, pneumatic elastomeric actuators exhibit high compliance (~1 MPa elastic modulus) and force (e.g., 7 N at 414 kPa [39]), large actuation strokes (e.g., over 200 ° bending angle at 150-350 kPa [39]), and fast movements (50 ms to bend circular from a linear shape at 345 kPa [40]). The use of elastomers should result in a wide thermal tolerance (-100 to 250 °C in silicone [99]). One setback to this actuation technology is the need of compressors, pumps, and air cylinders. They are big, leading to a bulky untethered structure, hindering mobility and the miniaturization of such robots. Pneumatic elastomeric actuators do not have self-sensing capability as the structure is a homogeneous silicone matrix. However, they can exhibit color change (camouflage) capability by injecting colored fluids into embedded channels [41]. It has been reported that the actuators are resistant to puncture and self-seal when combined with a fibrous material (e.g., Kevlar); however, the mechanism is not yet fully understood [42].

To date, several robots using pneumatic actuators have been demonstrated. Figure 2.2(e) is a legged robot that can perform different gait patterns by inflating certain combinations of body parts [326]. Changing the gait pattern enables it to go through narrow gaps. A larger version of this robot has been made untethered, equipped with a compressor and controller [44]. There have also been untethered systems such as a rolling robot using a series of pneumatic bending actuators [45], and a bio-inspired fish robot that can perform escape maneuvers in addition to forward swimming (Figure 2.2(f) [46]). Meanwhile, manipulation devices have been developed, such as, grippers [315], a dexterous hand [317], a discrete robotic arm [47], and tentacles [48]. The same technology has also been applied on a glove for hand rehabilitation [49].

2.3 Ionic Polymer-Metal Composites (IPMCs)

Ionic polymer-metal composites (IPMCs) [22] consist of an electrolyte-swollen polymer membrane (thickness 100-300 μm) sandwiched between two thin metallic layers. Figure 2.4 shows the working mechanism of IPMCs. The polymer is negatively charged and balanced by added mobile cations. When a voltage bias is applied to the electrodes, the cations relocate towards the cathode side. The relocation results in swelling the negative side of the membrane, causing a bending motion of the entire structure toward the positive side. Figure 2.2(g) shows the bending motion of an IPMC actuator.

IPMCs are compliant and are able to provide large bending strokes with low actuation voltages. Encapsulation enhances actuation performance in dry environments [23]. However, their response speed is slow (e.g., an IPMC actuator took 3.5 minutes to achieve ~270 deg of bending angle [26], Figure 2.2(h)), and their actuation characteristics exhibit hysteresis. Moreover, the output stress and the efficiency are low. Their slow motion makes them unsuitable to be applied to devices that require fast movements. IPMCs are capable of self-sensing [24] and energy harvesting [25].

The inherent need of water for IPMCs has accelerated their use in underwater robots. Researchers have demonstrated bio-inspired robots mimicking a sea-snake [27], fishes (caudal fin prop. [28], pectoral fin prop. [29]), manta ray [30], turtle [31], and jellyfishes [32, 33] (Figure 2.2(h)). Figure 2.2(g) shows an untethered fish robot where IPMCs are integrated into the root of the tail. Not confined to aquatic environments, terrestrial IPMC robots have been developed. Examples include worm-like [34] and deformable robots [35] that can crawl on the ground, as well as grippers [36, 37].

2.4 Dielectric Elastomer Actuators (DEAs)

Dielectric elastomer actuators (DEAs) are reviewed and discussed in detail in Chapter 3. A DEA consists of an elastomer membrane sandwiched between two compliant electrodes. Applying a voltage creates opposing charges on the electrodes. These charges attract each other and squeeze the elastomer membrane, resulting in thickness reduction and area expansion.

DEAs have high compliance (~1 MPa elastic modulus), large actuation strokes (up to 85 % of linear strain on a silicone elastomer [92]), fast response speeds (response time less than 200 μs [101]), and theoretically high electromechanical efficiency (maximum 90 % [102]). In a silicone elastomer, the hysteresis in a cycle is relatively small due to low viscoelasticity [100]. In addition, a silicone elastomer also has a wide thermal tolerance (-100 to 250 °C [99]). When carefully insulated, DEAs are able to work in an underwater environment [189], and are expected to be used in space [318]. However, DEAs usually generate low stresses, and a high voltage is necessary for driving them (typically a few kV), which requires the use of DC/DC converters. Recent developments suggest solutions to these problems. stacking methods (Section 3.5) can be used to improve the actuation stress. Commercially available miniaturized DC/DC converters (e.g., EMCO Q series [55], weight 4.25 g, volume 2.05 cm^3) improve the mobility of robots and their miniaturization.

DEAs have self-sensing capability [50]. Depending on the configuration, they can possess further capabilities, such as, self-healing [53], switching [51], energy harvesting [52], and color

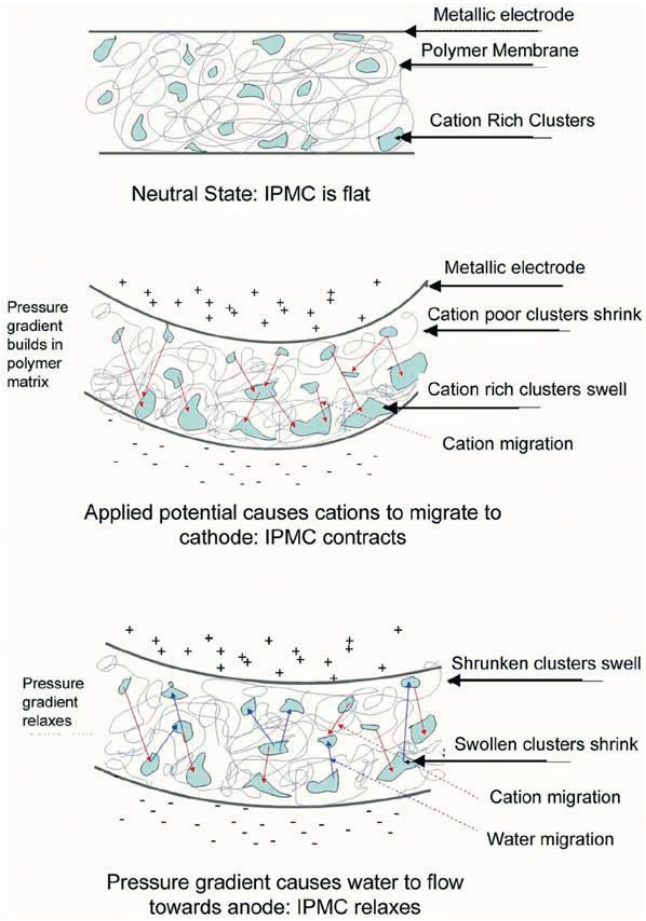

Figure 2.4 – Working mechanism of IPMCs, adopted from [99]. Applying a voltage bias relocates mobile cations toward the cathode side, causing the cathode side to swell and leading to a bending motion.

change [54]. The simple structure of DEAs has exploited a number of actuator configurations, and a wide range of robotic applications. Those are reviewed and discussed in detail in Chapter 3.

2.5 Concluding Remarks

Compared to other soft actuator technologies, DEAs are fast, potentially efficient, and exhibit small hysteresis and comparable or larger actuation strain. DEAs have weaknesses such as low stress and the need of high actuation voltages. However, recent developments show solutions to these problems. Small power sources can improve the mobility of DEA-based robots, and support their miniaturization. DEAs are able to work under dry and underwater environments at wide temperature ranges, and can be potentially used in space. They are also able to exhibit more smart capability than the others. Numerous existing actuator configurations and robotic applications prove that DEAs can be applied to many different desired actuator concepts and applications.

3 Dielectric Elastomer Actuators

This chapter reviews the operating principles of dielectric elastomer actuators and discusses the state of the art.

3.1 Actuation Principle

Dielectric elastomer actuators (DEAs) are a class of electroactive polymers (EAPs) [102, 195, 196]. While electrically induced deformation of a solid material was discovered in the late 18th century [56], the current working principles of DEAs were established in the late 1990s [294].

A DEA consists of an elastomer membrane sandwiched between two compliant electrodes, forming a soft capacitor as represented in Figure 3.1. When a voltage is applied (typically a few kV), opposing charges are induced on the electrodes. The opposite charges create an electric field inside the elastomer membrane in the direction normal to the surface, and their attraction generate an electrostatic pressure. This electrostatic pressure, known as the Maxwell stress, compresses the elastomer membrane, resulting in electrostatic actuation: a reduction in thickness, and an expansion in area. The Maxwell stress expresses the most fundamental equation that characterizes DEA actuation [294]. Let us assume that the DEA shown in Figure 3.1 is an elastomer with ideal electrodes (with no effect on the actuation, and their presence can be ignored), and that it is a closed thermodynamic system. The first law of thermodynamics is stated as [57]

$$dU = \delta Q - \delta W, \tag{3.1}$$

where δQ is the amount of heat added to the system, and δW is the work done by the system. The actuation of DEAs is an adiabatic process, and the Maxwell pressure p performs work on the elastomer through the surface A to result in a change in thickness of dz. Therefore,

$$\delta Q = 0, \tag{3.2}$$

and,

$$\delta W = -pAdz. \tag{3.3}$$

By substituting Equations 3.2 and 3.3 into Equation 3.1, we obtain

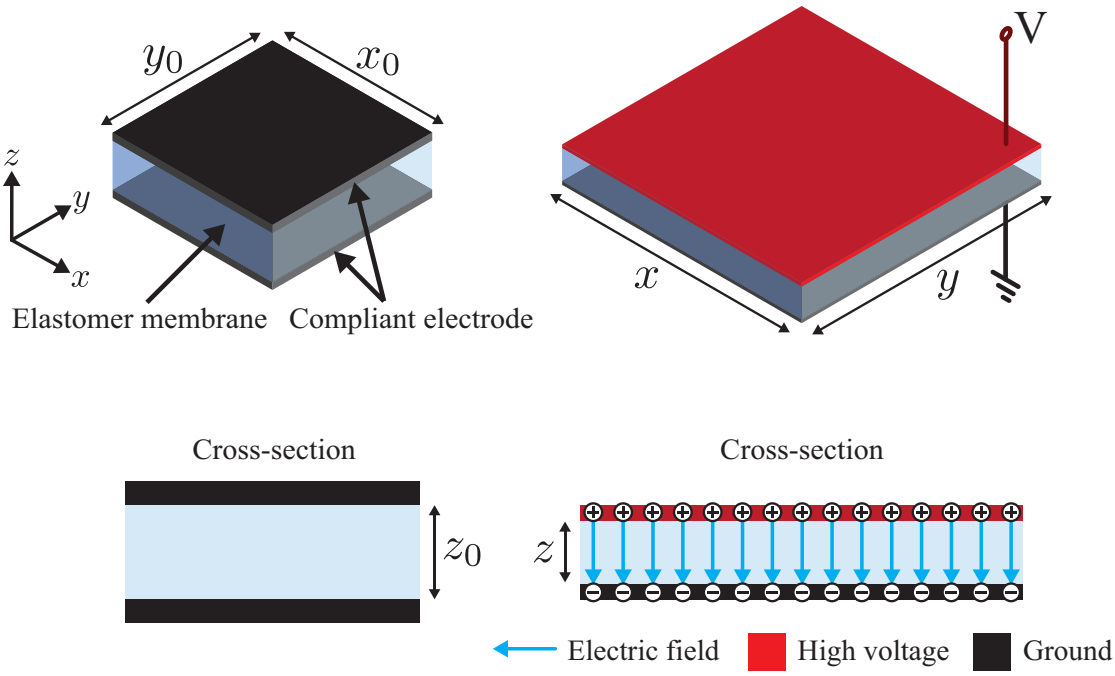

Figure 3.1 – Working principle of DEAs. A DEA consists of an elastomer membrane sandwiched between two compliant electrodes. Applying a voltage induces opposing charges on the electrodes, which generate an electrostatic pressure from the electric field in the direction normal to the surface. The electrostatic pressure squeezes the elastomer membrane, resulting in electrostatic actuation in the form of thickness reduction and area expansion.

$$\begin{aligned} dU &= pAdz, \\ \therefore p &= \frac{dU}{Adz}. \end{aligned} \tag{3.4}$$

The electrostatic energy of the elastomer forming a soft capacitor subject to an applied voltage V is

$$U = \frac{1}{2}CV^2 = \frac{1}{2}\varepsilon_0\varepsilon_r\frac{A}{z}V^2, \tag{3.5}$$

where C is the capacitance, ε_0 the permittivity of free space, ε_r the relative permittivity of the elastomer, and z is the thickness of the elastomer. The change in the electrostatic energy dU is given as the total differentiation of U with respect to z and A

$$dU = \frac{\partial U}{\partial z}dz + \frac{\partial U}{\partial A}dA. \tag{3.6}$$

Elastomers are known as an incompressible material (their Poisson's ratio is very close or equal to 0.5). This means the volume of the elastomer Vol is constant regardless of deformations

$$Vol = x_0 y_0 z_0 = xyz = Az = \text{constant}, \tag{3.7}$$

where x and y are the lateral lengths of the elastomer, x_0 and y_0 are their initial length, and z_0 is the initial thickness. From Equation 3.7, we find

$$\frac{dA}{A} = -\frac{dz}{z}. \tag{3.8}$$

Equation 3.8 represents an area expansion resulting in a thickness reduction. From this equation, Equation 3.6 becomes

$$dU = \left(-\frac{1}{2}\varepsilon_0\varepsilon_\mathrm{r}\frac{A}{z}V^2\right)dz + \left(-\frac{1}{2}\varepsilon_0\varepsilon_\mathrm{r}\frac{A}{z}V^2\right)dz = -\varepsilon_0\varepsilon_\mathrm{r}\frac{A}{z}V^2dz. \tag{3.9}$$

Substituting Equation 3.9 into Equation 3.4, we find

$$p = -\varepsilon_0\varepsilon_\mathrm{r}\frac{V^2}{z^2} = -\varepsilon_0\varepsilon_\mathrm{r}E^2, \tag{3.10}$$

where $E = V/z$ is the electric field. Since the Maxwell stress is in the compressive direction, the sign is negative.

Equation 3.10 shows that the Maxwell stress of DEAs is twice the magnitude of the electrostatic stress generated between two rigid parallel electrodes. This is due to the fact that the electrodes are expandable, which contributes as dA in the second term in Equation 3.6 [294]. Equation 3.10 suggests that the Maxwell stress is proportional to the square of the electric field, and relative permittivity ε_r. For DEAs, usually elastomers with an ε_r between 2 and 5 are used. DEA elastomers have a thickness typically several tens of microns before the application of an actuation voltage, which leads to high electric fields of 50-400 V/μm [233]. The literature has shown that ε_r can be increased when elastomers are chemically modified by adding grafting dipoles [58, 59, 60], fillers [63, 64, 65, 66, 67, 68], encapsulating fillers [61], and interpenetrating polymer networks with two or more polymers [62].

The Maxwell stress leads to deformation of the elastomer in the thickness and the lateral directions. The Maxwell stress (Equation 3.10) can be equalized with the mechanical stress in the thickness direction following from Hooke's law:

$$\begin{aligned} -\varepsilon_0\varepsilon_\mathrm{r}E^2 &= Y s_z, \\ \therefore s_z &= -\frac{\varepsilon_0\varepsilon_\mathrm{r}V^2}{Y z^2}, \end{aligned} \tag{3.11}$$

where s_z is the strain in the thickness direction, and Y is the elastic modulus (Young's modulus) of the elastomer. Under free boundary conditions, based on s_z, strains in the lateral directions

s_x and s_y are given with consideration of the incompressibility:

$$\begin{aligned} &x_0(1+s_x)y_0(1+s_y)z_0(1+s_z) = Vol, \\ &(1+s_x)(1+s_y)(1+s_z) = 1, \\ &\therefore s_x = s_y = (1+s_z)^{-\frac{1}{2}} - 1. \end{aligned} \tag{3.12}$$

For small strains less than 10%, z in Equation 3.11 can be approximated as the initial thickness z_0. However, in many cases the strain of DEAs is larger than 10%. In this case, a more precise form of Equation 3.11 has to be used, that is

$$\begin{aligned} &s_z = -\frac{\varepsilon_0 \varepsilon_\mathrm{r} V^2}{Y {z_0}^2 (1+s_z)^2}, \\ &(z = z_0(1+s_z)). \end{aligned} \tag{3.13}$$

Equation 3.13 leads to the solution

$$\begin{aligned} &s_z = -\frac{2}{3} + \frac{1}{3}\left(f(s_{z0}) + \frac{1}{f(s_{z0})}\right), \\ &f(s_{z0}) = \left[2 + 27 s_{z0} + \frac{\left\{-4 + (2+27s_{z0})^2\right\}^{\frac{1}{2}}}{2}\right]^{\frac{1}{3}}, \\ &s_{z0} = -\frac{\varepsilon_0 \varepsilon_\mathrm{r} V^2}{Y {z_0}^2}, \end{aligned} \tag{3.14}$$

where s_z takes on a real value. A sample calculation [69] shows that the small strain approximation (Equation 3.11 with $z = z_0$) gives an acceptable value of up to -6 %, suggesting the use of Equation 3.13 for higher strains. The model also predicts the pull-in instability for strains lower than -33 %, which triggers electrical breakdown. The pull-in instability occurs when the increasing electric field thins the elastomer, which in turn increases the electric field. This positive feedback loop drastically increases the local electric field beyond the breakdown field [70, 71].

Equation 3.13 assumes that the elastic modulus Y is constant, but in practice elastomers exhibit hyperelastic, non-linear stress-strain behavior. There are several hyperelastic models that describe the stress-strain behavior of elastomers: Neo-Hookean [330], Mooney-Rivlin [73, 74], Ogden [72], Yeoh [240], Arruda-Boyce [75], and Gent [76] (their comparison can be seen in [77, 78]). In these hyperelastic models, the strains of elastomers are represented as the stretch ratios. The stretch ratio is defined as the ratio between the length of a deformed line element and its initial length.

$$\lambda_x = \frac{x}{x_0},\ \lambda_y = \frac{y}{y_0},\ \lambda_z = \frac{z}{z_0}, \tag{3.15}$$

where λ_x, λ_y, and λ_z are the stretch ratios in the lateral directions and thickness direction, respectively. These stretch ratios are related to the strains defined in Equation 3.12:

$$\lambda_x = 1 + s_x,\ \lambda_y = 1 + s_y,\ \lambda_z = 1 + s_z. \tag{3.16}$$

The incompressibility of the elastomer is then expressed as

$$\lambda_x \lambda_y \lambda_z = 1. \tag{3.17}$$

DEA actuation mechanisms have been discussed based on the hyperelastic models of Neo-Hookean [82, 79, 80], Mooney-Rivlin [81, 82, 83], Ogden [82, 84, 83], Yeoh [83, 85, 86], Arruda-Boyce [87, 97, 98], and Gent [239, 88, 234, 92].

3.2 Pre-stretch

Stretching elastomers prior to their actuation is called pre-stretch. To date, most DEA devices have pre-stretch. Pre-stretch thins the elastomer, improving actuation performance (i.e., the Maxwell stress) as suggested in Equation 3.10 in Section 3.1. Other than that, the advantages of pre-stretching elastomers are: (1) it increases breakdown strength, (2) it suppresses the pull-in instability, and (3) it can create a preferred direction of actuation strain. Higher breakdown strength and suppression of the pull-in instability drastically improve actuation performance of DEAs. Researchers have observed that pre-stretch significantly increases breakdown field, for example, from 18 to 218 V/μm with 500% × 500% biaxial pre-stretch in acrylic elastomers [90], and from 100 to 250 V/μm with 275% × 275% biaxial pre-stretch in silicone elastomers [92]. The mechanism behind the increase in breakdown strength is however not yet fully understood.

When subjected to a pre-stretch, the elastic modulus of the elastomer increases. This stiffening shifts the stress-strain behavior of the elastomer, improving resistance to the pull-in instability. As a result, the actuation strain of the elastomer can be beyond the strain where the instability occurs [91, 239, 87]. It should be mentioned that in principle stiffening elastomers leads to lower actuation strain at a given applied voltage as can be seen in Equation 3.13 in Section 3.1. This suggests (1) pre-stretch may not be preferred for low actuation strain, and (2) there is an optimal pre-stretch to maximize actuation strain [87, 92, 88]. Additionally, the stiffening improves mechanical efficiency and response speed of elastomers [93], regardless of the slight reduction in relative permittivity that can occur with pre-stretch [94].

Pre-stretch is also important for defining the orientation of actuation strain. It has been shown that DEAs tend to produce greater actuation strain in the direction perpendicular to pre-stretch [233, 92]. This characteristic is effective when actuation in a preferred direction is necessary (e.g., a bending actuator [157] or a cell stretcher [96]). The potential disadvantage of pre-stretch is the need for a frame or other semi-rigid structure to keep the elastomer in tension. This added complexity leads to a reduction in the total performance of the DEA device such as work density and power to mass ratio [195].

3.3 Dielectric Elastomers

Elastomers used for DEAs include acrylics, silicones, fluoroelastomers, polyurethane, polybutadiene, and polyisoprene [81, 233], in which acrylics and silicones are the two most commonly used. The most common acrylic elastomer in use is VHB, a commercially available adhesive product (3M VHB4905/4910, Figure 3.2(a)) that have been used for most of acrylic elastomer based DEAs. VHBs generate large actuation strains, and since they are available in rolls, there is no need to pre-fabricate the elastomer, and DEA device production can be easy and fast. However, their limited choice of available thicknesses (0.5 mm and 1.0 mm) prevents the selection of preferred combinations of pre-stretch and thickness. In addition, the high viscoelasticity of VHB acrylics lowers response speed and reliability, and their narrow thermal tolerance (-10 to 90 °C [99]) may limit its application in some environments [102, 243, 100].

Silicone elastomers, on the other hand, exhibit a high response speed [243] (response time less than 200 μs [101]), have low viscoelasticity, and a wide thermal tolerance [102, 100] (-100 to 250 °C [99]), although their actuation strains are relatively small. There are many products in this class of elastomers, which differ in terms of material properties such as elastic modulus, viscoelasticity, maximum strain, and relative permittivity. They are usually supplied in the non-polymerized liquid state (Figure 3.2(b)(i)), allowing for casting of the elastomers at the desired thickness.

Their liquid state also allows modification of material properties such as relative permittivity (by adding filler, described in Section 3.1) and elastic modulus (curing temperature [308, 103] or amount of solution [104]). These features of silicone elastomers encourage the development of fast and reliable DEA applications with a wide array of elastomer characteristics. In this thesis, silicone elastomers are used for fabrication of DEAs. As shown in Figure 3.2(b)(ii-iv), the elastomer is mixed with a curing agent (depending on the type of elastomer, a solvent is also mixed), and the mixture is blade-casted on a film substrate using a variable gap applicator which is moved with a film applicator coater. After curing, silicone elastomers with desired thicknesses are fabricated.

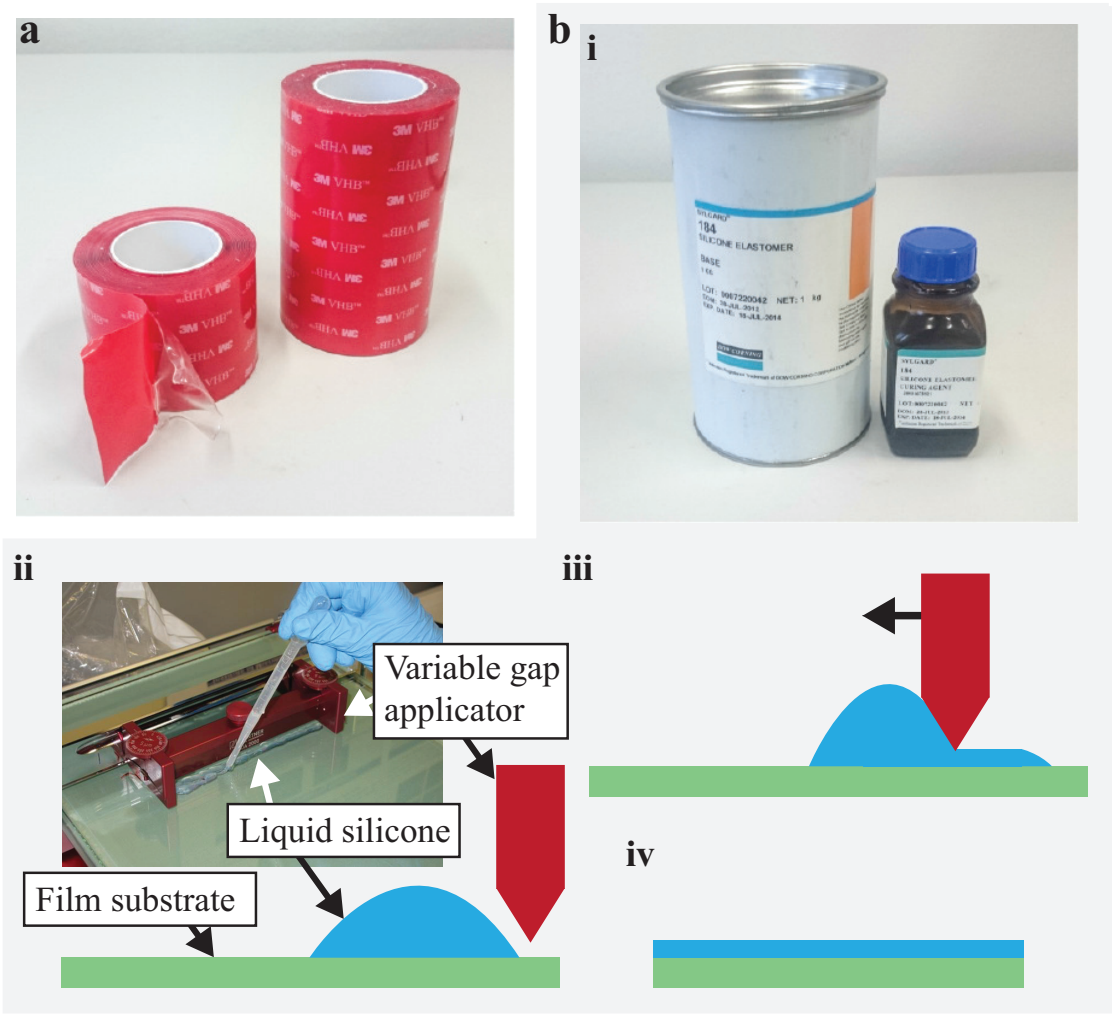

Figure 3.2 – Available products of acrylic and silicone elastomers. (a) 3M VHB4905 acrylic elastomer. The elastomer is provided as a rolled sheet. (b)(i) A silicone elastomer (Dow Corning Sylgard 184). The elastomer is provided as liquid silicone in a pot (left). For polymerization, a curing agent is mixed (right). (ii) The elastomer is mixed with the agent (depending on type of elastomer, solvent is also mixed), and the solution is placed on a film substrate. (iii) The solution is blade-casted using a variable gap applicator and a film applicator coater. (iv) After curing, a silicone elastomer with desired thickness is fabricated. The picture is adopted from [126].

3.4 Electrodes

In DEAs, electrodes serve to hold charges, but they may also exhibit passive characteristics. This means that the electrode stiffness may contribute a resistance to the actuation of DEAs. The mechanical resistance of the electrodes depends on the stiffness and dimension (in most cases the thickness) of the electrodes, where the desired electrical conductivity of the electrodes often determines the minimum required thickness. Therefore, ideal electrodes should be compliant, thin, and electrically conductive as much as possible [294]. The electrodes should also be able to be patterned to accurate dimensions. In addition, mechanical and electrical stability over time, a high number of attainable actuation cycles, and resistance to the external environment (e.g., light, temperature, humidity, physical damage, etc.) are important electrode characteristics to sustain reliable actuation performance over the duration of applied use. Interestingly, DEAs can be activated without electrodes by spraying charges directly to the elastomer membrane surface [105]. However, removal of the charges from the elastomer surface is difficult. The use of electrodes make DEAs easier to be operated with faster charging and discharging.

Two main categories exist for DEA electrodes: metallic based electrodes and carbon based electrodes [106]. In metallic based electrodes, a widely used method is to form thin metal layers. However, metallic layers significantly lower the actuation strain due to their elastic modulus several orders of magnitude higher than that of elastomers. Cracks created during actuation lowers the conductivity, and can limit the actuation strain to only 2-3% [107]. Metallic layers can be more stretchable when formed in a buckling shape [108] or corrugated shape [109, 110, 111], although strain is still small (up to 23 % [108] and 33 % [109] before the electrode loses conductivity or breaks). Metallic wires with zig-zag or horseshoe shapes make the electrode stretchable by up to 80 % strain before losing conductivity [81]. In this case an additional low conductivity layer is necessary to distribute charges on the elastomer surface, adding complexity to the DEA structure.

Another method of producing metallic based electrodes is to "shoot" metallic particles into elastomers. In this approach, implanted metallic clusters are formed in the several tens of nanometers below the elastomer surface. This technology is called filtered cathodic vacuum arc [107] and supersonic cluster beam implantation [112]. It has been shown that electrodes based on this method achieve large strain before losing conductivity (175 % [107] and 100 % [112]). Also, the impact on the stiffness is low; a 25 μm-thick elastomer membrane with elastic modulus of 1 MPa showed 100 % relative increase after the implantation [107]. However, this method requires plasma generation in a vacuum environment, leading to the need of a customized setup. Pumping time could make fabrication slow, and chamber size limits the size of the DEA. These constraints also lead to a difficulty for producing a large number of samples in a reasonable time. A bigger setup may solve the problem, but would bring drastically increased cost. Recently, the use of liquid metal has also been explored [113, 114]. However, encapsulation of the metal may lead to non-negligible amounts of passive elements in the DEA.

In carbon electrodes, carbon black [121] (carbon nanoparticles, also known as carbon powder) is commonly used as a conductive material, while carbon nanotubes and graphene

are less commonly used [117, 115, 116]. The easiest way to form these electrodes is to deposit the carbon black directly on the elastomer surface [118]. In principle, this method does not mechanically resist the actuation of the DEA, as the carbon particles are free to move. However, for the same reason, these electrodes can be collapsed and removed very easily by damages. This creates difficulties in handling; the fabrication environment can become easily contaminated, and it is hard to pattern such electrodes to accurate dimensions. Carbon grease, a mixture of carbon black and oil, has better adhesion compared to the direct deposition of the particles. The liquid-like form of carbon grease does not resist the actuation of DEAs, and eases the application. However, accurate patterning is not established yet (usually a paint brush is used [119, 120]). Also, this greasy electrode rubs off with any physical contact, leading to further contamination.

Instead of oil, carbon black can be mixed with a non-polymerized silicone to form a carbon black-filled elastomer [121, 122, 123]. In principle, other carbon materials such as carbon nanotube and graphene can be used [124]. When it is cured, electrodes based on carbon black-filled elastomers have good robustness to physical damage and strong adhesion to the elastomer surface. However, the stiffening impact of the elastomeric electrode on DEA actuation is not negligible, as it is a passive elastomer layer. Therefore, the electrode has to be made thin enough. For this purpose, pad-printing [182, 125] realizes thin elatomeric electrodes with accurate dimension. Pad-printing uses a stamping machine in which non-cured carbon black-filled elastomer is treated as "ink".

The ink is filled into an etched relief with the desired geometry on a steel plate, and transferred by a silicone pad to the elastomer. As shown in Figure 3.3(a), the pad stamps the ink onto the DEA elastomer surface. Instead of using the etched plate, the desired electrode geometry can also be realized by placing a shadow mask made from a thin film (e.g., PET: polyethylene terephthalate and PI: polyimide) onto the DEA elastomer surface (As shown in Figure 3.3(b)). In this case, the pad that stamps the ink has a diameter larger than the length of the desired electrode geometry. The pad deforms according to the mask geometry; due to this deformation, the resulting electrode dimension is slightly smaller than that of the mask.

Pad-printing patterns the electrode to a thickness of about 1-4 μm [126, 125], which is negligible given the thickness of the DEA elastomer (typically several tens of microns). With this method, a minimum feature dimension of 100 μm is realized. Figure 3.3(c) shows a DEA with pad-printed electrodes. The electrodes show a strong resistance to damages. So far, the pad-printed electrode is not fully characterized, but it exhibits sufficient actuation strain up to 85 % in linear stretch [92]. In this thesis, a carbon black-filled elastomer and pad-printing with a mask (Figure 3.3(b)) are used for fabrication of DEA electrodes. For pad-printing, a stamping machine (Teca-Print, TPM-101) is used.

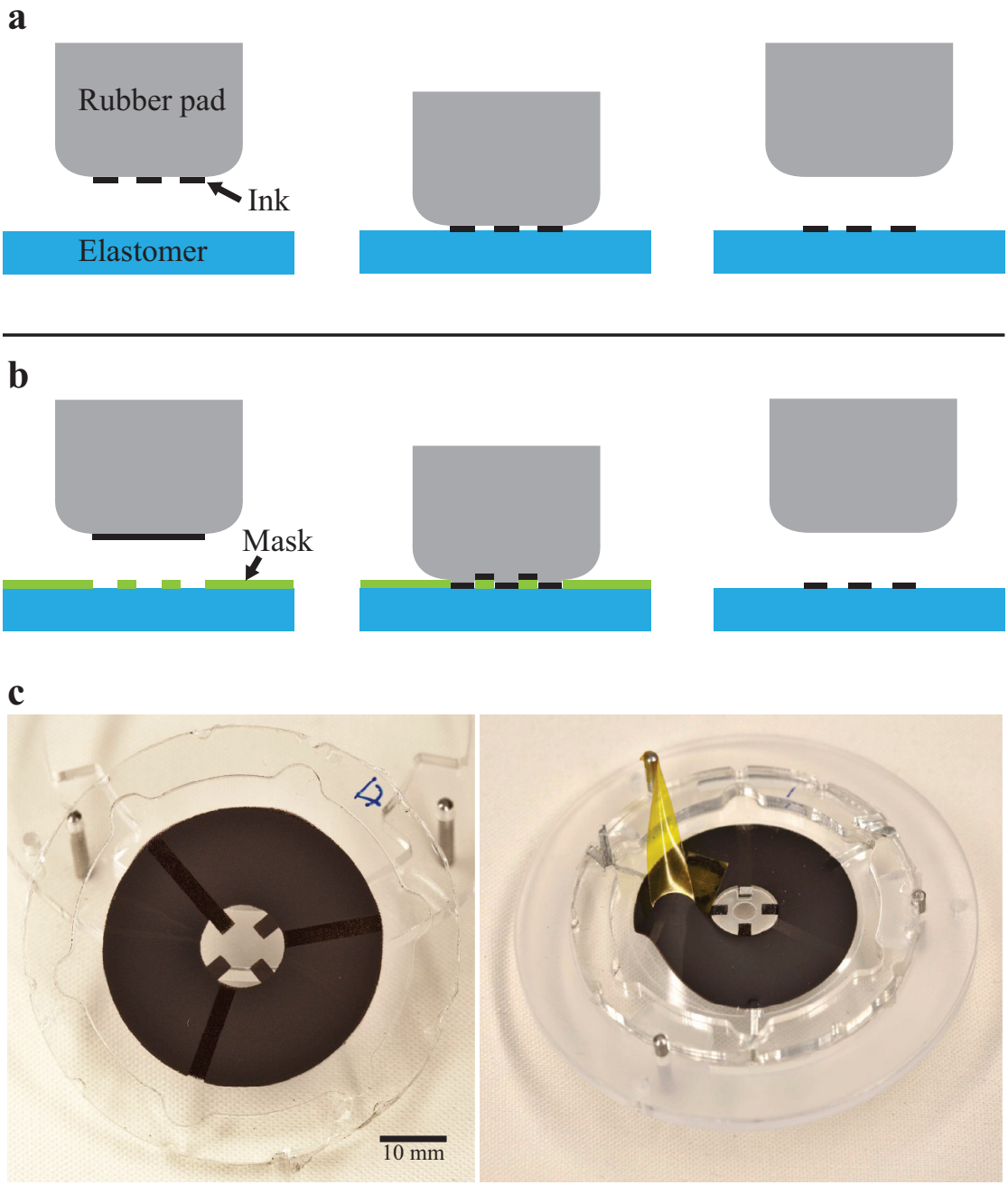

Figure 3.3 – Patterning of elastomeric electrodes by pad-printing. (a) The pad transfers ink with the desired electrode geometry from an etched steel plate. The ink is then stamped onto the elastomer surface. After curing, electrodes with thickness of 1-3.5 μm are formed on the surface. (b) Instead of using an etched plate, a shadow mask can also be used. In this case, the pad stamps the ink with dimension larger than the desired electrode geometry. The pad deforms according to the mask geometry. Due to this deformation, the resulting electrode dimension is slightly smaller than that of the mask. (c) (left) A DEA with pad-printed electrodes. (right) The electrodes show a strong resistance to damage (a Kapton tape is adhered and removed with no exfoliation). The pictures are adopted from [182].

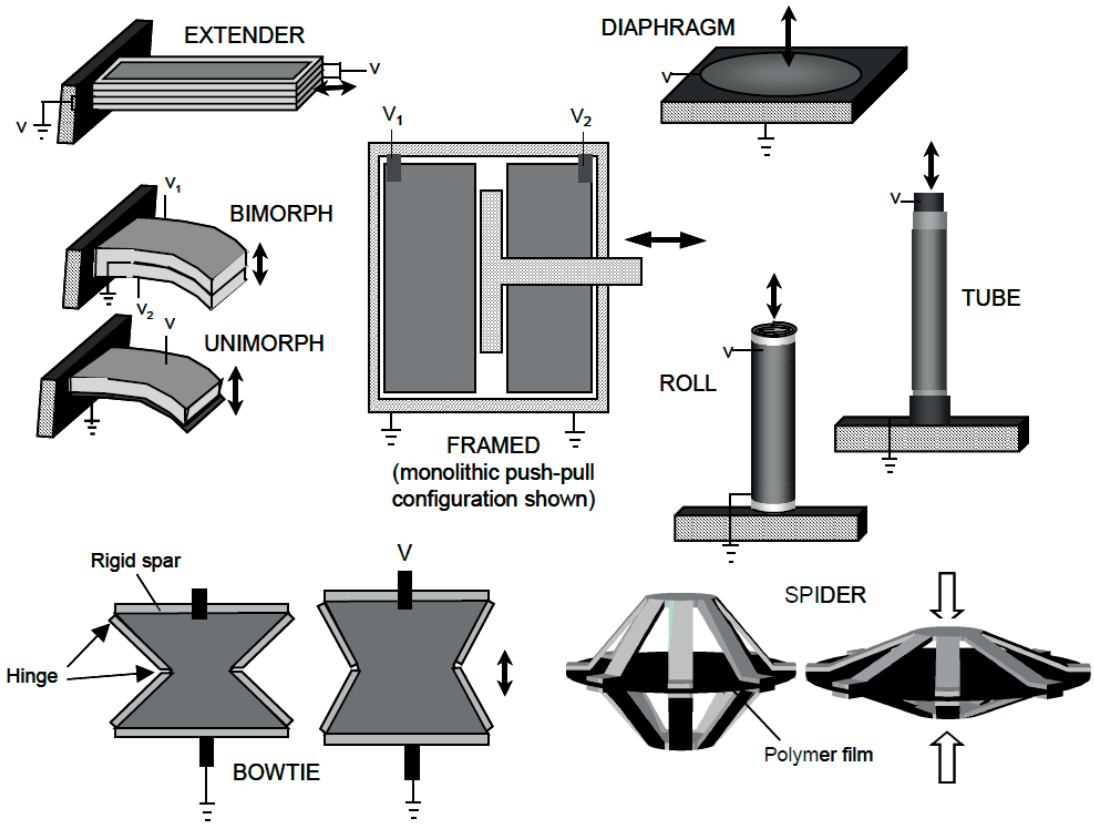

Figure 3.4 – Basic DEA configurations (adopted from [128]).

3.5 Actuator Configurations

Actuator configuration is important to orient the actuation of DEAs from thickness reduction and area expansion of an elastomer membrane to desired practical actuation behavior for applications. Figure 3.4 summarizes basic DEA configurations demonstrated at the early stage of developments (in the late 1990s-early 2000s) [128]: an extender, unimorph, bimorph, framed, bowtie, spider, roll and tube. An extender elongates the structure composed of several stacked DEAs by fixing one end. Stacking of DEA layers is an effective method to achieve the required performance such as force and actuation stroke in a given actuator dimension. An example of an extender can be seen in a variable mechanical impedance actuator for hand rehabilitation [127]. When a DEA is laminated to a flexible substrate, the elongation leads to a bending actuation (unimorph). A unimorph is simplest configuration that performs out-of-plane actuation. An example can be seen in an actuator intended to be used as active origami [206]. Similarly, attaching another DEA on the other side of a unimorph results in a bimorph configuration.

A framed configuration generates in-plane linear actuation. The schematic shown in Figure 3.4 is an example of a framed configuration, where the two DEAs generate push-pull actuation of the center part by activating them independently. When the frame is equipped with a hinge or compliant joint, the area expansion of the DEA is transmitted to frame move-

ments (bowtie). The characteristics of the movements depends on frame configuration such as shape, position, and number of hinges. An example of a bowtie configuration can be seen in actuators designed for binary robotic system with high degrees-of-freedom [135, 136, 137]. Figure 3.5(a) shows one of those actuators [136].

The area expansion of the DEA triggers a bistable mechanism integrated in the frame. A spider is another form of the bowtie configuration, where the frame forms an out-of-plane shape and generates contracting linear actuation perpendicular to the DEA surface. In the diaphragm configuration, the DEA generates out-of-plane displacement due to fixed boundary conditions. Figure 3.5(b) is an example in which several diaphragm DEAs are integrated. This actuator is designed as a module of an inchworm robot shown in Figure 3.7(c). Tube configurations generate linear actuation by elongation of the structure, similar to an extender. An example of this configuration are DEA fiber actuators [132, 133, 134]. Roll configurations generate linear actuation by elongation of the structure, similar to extenders. The roll configuration allows for easier fabrication of a stacked linear actuator than for the extender (just wrap a DEA sheet). An example of this configuration can be seen in [129], and integration of corrugated electrodes has been reported [130].

Since then, many different actuator configurations have been developed, including modification and upgrade of those basic configurations described above. The spring roll configuration (Figure 3.5(c)) is an improved version of the roll [131, 194]. In this actuator, the elongation of a wrapped DEA stack is transferred to relaxation of the compressed spring, resulting in efficient mechanical performance. This configuration has been further developed to perform multi-degrees-of-freedom (DOF) actuation (2-DOF: elongation and bending) by segmented electrodes [172]. Multi-DOF actuation has also been realized in framed conical actuators (5-DOF [138, 139]. Figure 3.5(d) represents 5-DOF movement schematically as actuation stroke in the z-direction, and translational and rotational actuation in the x- and y-directions.

Segmentation of the electrodes enables local activation of DEAs, which has led to rotational actuation [139, 140, 141]. The device shown in Figure 3.5(e) is a motor driven by activating the segmented electrodes periodically with phase. This actuation strategy is presented as the driving method of the rolling robot shown in Figure 3.7(h). Local activation of DEAs has showed possibility to realize complicated deformations in a gas-inflated diaphragm actuator ([142], Figure 3.5(f)).

A gas-inflated configuration has also been employed in tube actuators [143, 144] to improve their actuation performance, in spherical actuators [147], to achieve eye-ball motions [148], the rolling actuation of bulged structure [149], and large strain and giant deformations in diaphragm actuators [145, 146]. Figure 3.5(g) is a diaphragm actuator exhibiting giant deformation due to the snap-through instability [146].

Not only gas, but also fluid has been used to mechanically couple the active and passive parts, so that mechanical impedance is variable against load [150]. Figure 3.5(h) shows the cross-section of a hydro coupled DEA, with a picture implying the use in haptic devices. Since then, the use of fluid has enabled enhanced breakdown strength in a tube actuator [151] and giant deformation in diaphragm actuators [152, 153].

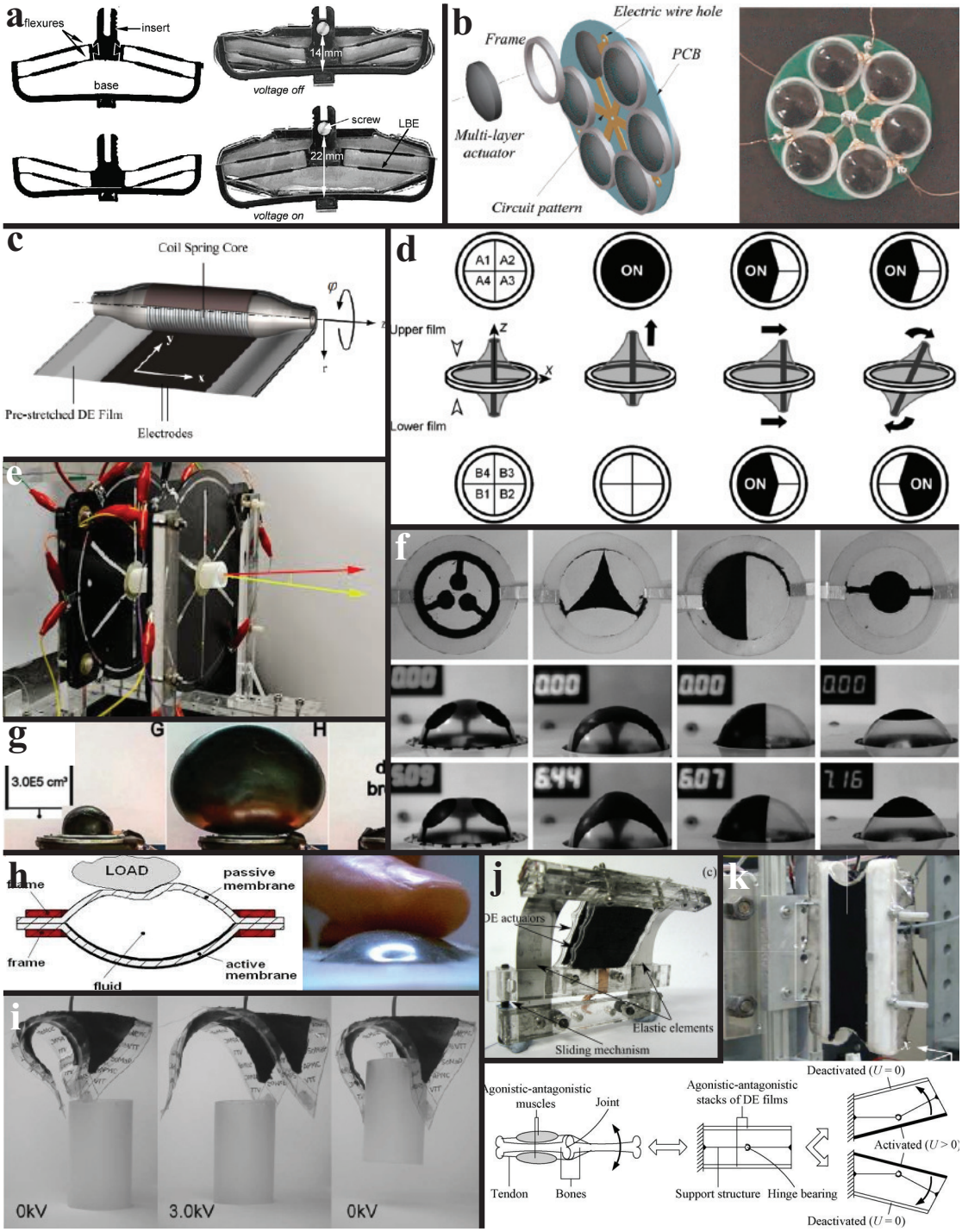

Figure 3.5 – Developed DEA configurations. (a) Bistable actuator for binary robotic system [136]. (b) Modular actuator with integrated diaphragms [176]. (c) Spring roll actuator [194]. (d) 5-DOF conical actuator [139]. (e) DEA motor [140]. (f) Diaphragm actuator with local activation [142]. (g) Diaphragm actuator showing giant deformation [146]. (h) Fluidically coupled actuator [150]. (i) Triangular DEMES acting as fingers [272]. (j) Bistable DEMES [273]. (k) Antagonistic actuator [236].

Meanwhile, the self-organized, dielectric elastomer minimum energy structure (DEMES) [154, 272] has been proposed as a new class of DEA configurations that consists of a pre-stretched DEA attached on a flexible frame. At zero voltage, a DEMES exhibits a curled shape where the internal stress of the DEA and the bending moment of the frame are balanced. Activation of the DEA releases the bending moment and uncurls the frame. Depending on the design parameters such as frame geometry and pre-stretch direction, DEMES exhibit various shapes from a simple bending actuator to complicated 3D active structures [179]. Figure 3.5(i) is a DEMES whose frame geometry is initially a triangle, but the pre-stretch of the DEA make the vertexes as gripper fingers [272]. DEMESs have been further developed to achieve improved actuation performance with frame reinforcement [155], bistable actuation (Figure 3.5(f)) [273], longer shape with segmented electrodes [318], translational movement [156], and higher compliance based on soft material [271], followed by studies on modeling [157, 89].

Other than DEMES, the use of pre-stretch has been a standard for different configurations enabling antagonistic actuation in a hinge segment actuator [236], a shell-like actuator [158], and a bending actuator with a microstructural substrate [159]. Figure 3.5(k) shows an antagonistic actuator with its schematics [236]. The actuator is designed based on the bioinspiration of musle agonist antagonist movement, and is a module of a multi-DOF manipulator [160]. Bistable actuation has also been demonstrated in conical actuators [161], flip-flop actuators [237], and high voltage pulse induced buckling actuators [162]. In addition to pre-stretch, fiber stiffening that constraints the actuation strain of DEAs in a specific direction [88], has shown large actuation stroke in a roll configuration [235], and capability to generate different bending shapes [319] in a soft actuator.

All the configurations described above essentially rely on the area expansion of DEAs. When thickness reduction is employed as the primaryactuation principle, the actuator exhibits muscle-like linear contraction, as shown in Figure 3.6(a). For this purpose, several stacking methods have been demonstrated based on helical [163], folding [164], and multilayer stack geometries [165, 166, 167]. Helical and folding configurations are shown in Figure 3.6(b)(right) and Figure 3.6(c), respectively. These methods can realize stacked actuators with just one continuous DEA (Figure 3.6(c)), resulting in relatively easy fabrication. Figure 3.6(d) shows fabricated actuators based on a foled stack, and represents the applicability of this method on different sizes and geometries. A multilayer stack, shown in Figure 3.6(c)(left), requires lamination of independent DEA layers, resulting in a relatively complicated fabrication setup and difficulty in realization of electrical connection. Figure 3.6(e) is an example of an actuator based on multilayer stacking [165]. This 21 mm long actuator performed lifting up a 1 kg mass with 10 % contraction. For linear contractile actuators, the use of rigid electrodes has also been demonstrated [168]. DEAs with a combination of rigid and compliant electrodes have performed actuated surface patterns, such as creasing [169]. The same principle has demonstrated bio-inspired fluorescent patterning [170].

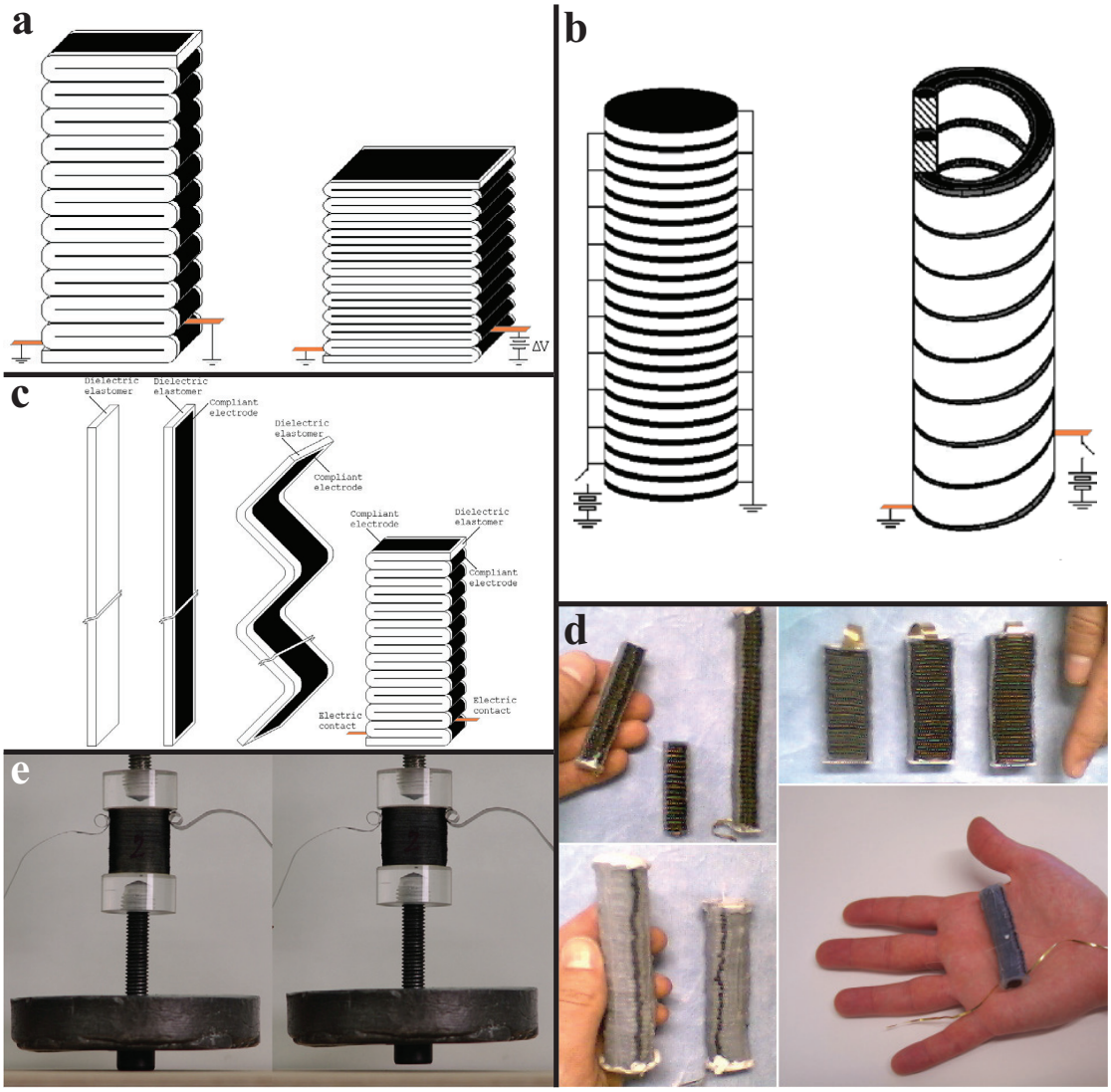

Figure 3.6 – Stacked DEAs and their fabrication method. (a) Stacked DEA exhibits muscle-like linear contraction. (b)(left) DEA configuration with the multilayer stack method. (right) DEA configuration with helical stack method. (c) DEA configuration with folded stack method. The stacked actuator can be realized with one continuous DEA. The same applies to the helical stack method. (d) Fabricated actuators based on the folded stack method. (a)-(d) are adopted from [164]. (e) Multilayer stacked actuator lifting up a mass of 1 kg [165].

3.6 Robotic Applications

Robotic applications based on DEAs have been widely explored. Figure 3.7(a) is a legged robot consisted of six 2-DOF spring roll actuators [172]. Bending actuation of each leg moves the robot in different directions. For this type of legged robot, employing linear contractile actuators could mimic the movements of animals. Figure 3.7(b) is a quadruped in which each leg has 2 linear actuators to perform animal-like 2-DOF motion [208]. Other legged robots can be seen in [171, 173]. Biomimetic ground locomotion based on extension or undulation of its body has also been realized in the form of an inchworm [171, 176, 177, 178] or snake [172, 179]. Figure 3.7(c) shows an inchworm robot that can extend and contract segments of its body to locomote, thanks to the actuated displacements of modular connected diaphragm actuators (Figure 3.5(b)). A similar mechanism can be seen in the snake-like robot shown in Figure 3.7(d) in which several DEMESs are integrated [179].

Hopping or jumping is a useful capability of robots to explore cluttered terrain in search and rescue missions. Figure 3.7(e) is a jumping robot composed of 3 framed actuators [174]. Activation of the DEAs lead to sudden movement of tilted legs which strike the ground and the reaction force makes the robot jump. Figure 3.7(f) is another example where the area expansion of the DEA acts as a trigger to release the stored elastic energy in a bistable leg [175]. Rolling is another way to use a robot body for terrestrial movements. Demonstrated DEA rolling robots can be seen in [180, 181, 182]. Figure 3.7(g) shows an inflated robot performing rolling locomotion by actuating each segmented electrode [181]. When the rotational axis of the DEA motor (Figure 3.5(e)) is fixed at its transnational movements, activation of each segmented electrode shifts the center of mass and entire actuator can rotate. Such movement can be directly used for a rolling robot, as shown in Figure 3.7(h).

Their thin and lightweight characteristics have inspired the use of DEAs in aerial vehicles. Researchers have developed fish-like airships [183, 184] and flapping mechanisms [185, 186], and analytically investigated aerodynamic control using active membrane wing [187] and wing morphing [188]. Figure 3.7(i) is a DEA driven airship (8 m long) where the actuators are placed on both sides of the body and also on the root of the tail [184]. The actuation results in a biomimetic swimming motion consisting of body undulation and tail displacement. Meanwhile, mobility underwater has also been demonstrated in a jellyfish like form [189], as shown in Figure 3.7(j), where a bulged diaphragm actuator changes its volume, allowing buoyancy control. The actuation also serves to eject water, producing a propulsion force.

Not only restricted to mobile robots, the inherent compliance of DEAs has encouraged their use in soft grippers [272, 318, 319] and manipulators [160]. Figure 3.7(k) shows a fiber stiffened actuator performing soft grasping of an object [319]. The same characteristics have inspired human assistive devices, leading to the discussion on upper limb prosthetics [190]. Figure 3.7(l) is an active bandage to improve venous blood return [192]. The compliance of the DEA allows better conformation and has low mechanical impact on the human body. The active hand shown in Figure 3.7(m) is another example in which linear contraction helps in finger rehabilitation [191]. Additionally, demonstrations of android eye-balls [193] and an arm wrestling robot [194] imply the use of the technology in human-robot interactions. In these devices, the spring roll actuator (Figure 3.5(c)) is used.

Figure 3.7 – Robotic applications based on DEAs. (a) Legged robot using 2-DOF spring roll actuators [172]. (b) Quadruped using linear contractile actuators [208]. (c) Inchworm robot using modular diaphragm actuators [176]. (d) Snake-like robot using DEMESs [179]. (e) Hopping robot using framed actuators [174]. (f) Jumping robot using a bistable actuator [175]. (g) Rolling robot using an inflated actuator [181]. (h) Rolling robot using DEA motor [182]. (i) Fish-like airship [184]. (j) Jellyfish-like robot using inflated actuator [189]. (k) Soft gripper using fiber stiffened actuator [319]. (l) Active bandage. (m) Active hand for finger rehabilitation [191]. (n) Android eye-ball [193] and (o) arm wrestling robot using spring roll actuators [194].

3.7 Concluding Remarks

Numerous actuators based on DEAs and robotic applications have been developed. However, functional actuators with folding, controllable stiffness, or adhesion, and their robotic applications have not been investigated and demonstrated. In the rest of this thesis, those functional actuators are investigated based on silicone elastomers and pad-printed compliant electrodes consisting of a carbon black-filled elastomer.

4 Foldable Antagonistic Dielectric Elastomer Actuator

This chapter develops an actuator with folding functionality based on dielectric elastomers. The actuator consists of 2 sets of pre-stretched DEAs forming a simple antagonistic configuration that enables bidirectional actuation and passive folding. In order to validate the actuator concept through a specific application test, a foldable elevon actuator with outline size of 70 mm × 130 mm is developed with angular displacement range and torque specifications matched to a 400 mm wingspan micro air vehicle (MAV) of mass 130 g. A closed-form analytical model of the actuator is constructed to guide the actuator design. The developed actuator exhibits voltage-controllable angular displacement up to ± 26 ° and torque of 2720 mN·mm. Two elevon actuators are integrated into the MAV, which is successfully flown, with the foldable actuators providing stable and well controlled flight. The actuator is evaluated in terms of the controllability of the MAV by calculating the correlation between the control signal and the MAV motion. As the result, a strong correlation in roll axis of over 0.7 is obtained.

4.1 Introduction

Folding technology in robotics has been explored as a means of programmable shape change [197, 198], locking and variable transmission mechanisms [226, 228], and self-assembling of mobile robots [209, 212, 214], grippers [211, 215], and other robotics parts such as structures [210], electric devices [213], and propellers [216]. Moreover, the same technology has also enabled several functionalities in aerial robots such as multi-modal locomotion [229], deployable wing [230], improved portability [231], and robustness to collision [232]. As a method to building robots, folding architecture has been applied for passively foldable robots [222], legged robots [225], worm robots [219, 223], millimeter-scale robots [217, 218, 221], low-profile robots [220], a manipulation system [224], and a robot with deformable wheel [227]. The same architecture has been employed in soft actuators as structure to orient their actuation behavior (EAPs [199, 202, 205, 206], SMAs [200], and pneumatic elastomeric actuators [201, 203, 204]) or as fabrication method (EAPs [207, 208], also known as stacking method).

There are two approaches to achieve folding functionality: traditional mechanical ap-

This chapter is adapted from the article:
J. Shintake, S. Rosset, B. Schubert, D. Floreano and H. Shea, "A foldable antagonistic actuator," *IEEE/ASME Transactions on Mechatronics*, vol. 20, no. 5, pp. 1997-2008, 2015.

proach and the use of soft actuators. In traditional mechanical approach, folding is achieved with dedicated mechanisms including mechanical parts like gears and linkages, and in some cases additional actuators dedicated to folding [229]. This may lead to increasing complexity of the structure, which results in increased design difficulty and fragility to external shocks and overload. The use of soft actuators remove the need for complex mechanical assemblies and additional actuators, thus simplifying the structure. In particular, when formed as a folding actuator, DEAs are expected to create a compliant actuated joint that can passively fold. The high compliance of DEAs also gives robustness to external shocks and overload, and their highly elastic behavior allows for structures that self-deploy through the release of stored elastic strain energy. Such a DEA based folding actuator could bring robots that are passively foldable, self-deployable, mechanically robust, and portable.

The aim of the work in this chapter is to develop a foldable actuator based on dielectric elastomers. First, the concept of a foldable actuator is presented and then validated through an application test. A fixed wing micro air vehicle (MAV) is developed as the application in which the actuator is used as an elevon (control surface). After the characterization of the elevon actuator, the actuator is evaluated in terms of the controllability of the MAV using the motion data obtained during flight. Finally, the results obtained in this chapter are discussed.

4.2 Working Mechanism

The actuator concept has an antagonistic configuration with two sets of stacked (or single) DEAs that allow bidirectional actuation and passive folding. Figure 4.1 represents the mechanism of the actuator, in which Figure 4.1(a) shows the non-actuated state. The actuator consists of rigid parts formed with two arms connected via elastic hinges that are symmetrically placed across the spacer and the DEAs. The DEAs are attached at their end points to the arms while their centers are connected to the spacer such that they form an antagonistic configuration across the horizontal plane. All the DEAs have the same pre-stretch. The stretch in direction 1 is constant regardless of the actuation, and it is higher than the stretch in direction 2. Due to the pre-stretch, each DEA has an internal stress that keeps the actuator in its rest state.

According to the literature [233, 92, 234], the higher pre-stretch in direction 1 is expected to produce a large actuation stretch laterally perpendicular to its axis. This method has been applied to a cylindrical DEA configuration [235], which has shown a large actuation stroke. While several mechanisms using an antagonistic configuration of DEAs have been developed [236, 237], our concept uses elastic hinges for supporting the folding of the structure and as an additional design parameter. The actuator output characteristics, such as the angular displacement and the torque, vary with the material properties or the geometry of the hinge. The characteristics can further be adjusted by changing the material properties or the geometry of the DEA. However, since many parameters are strongly related, it is often difficult to adapt a parameter in the DEA while keeping other parameters optimal (e.g., the thickness to maximize the electrostatic pressure or the pre-stretch to enlarge the actuation).

As shown in Figure 4.1(b), when a voltage is applied to only the top or the bottom DEA of the actuator whose one tip is fixed, the electrostatic pressure in the DEA reduces the internal

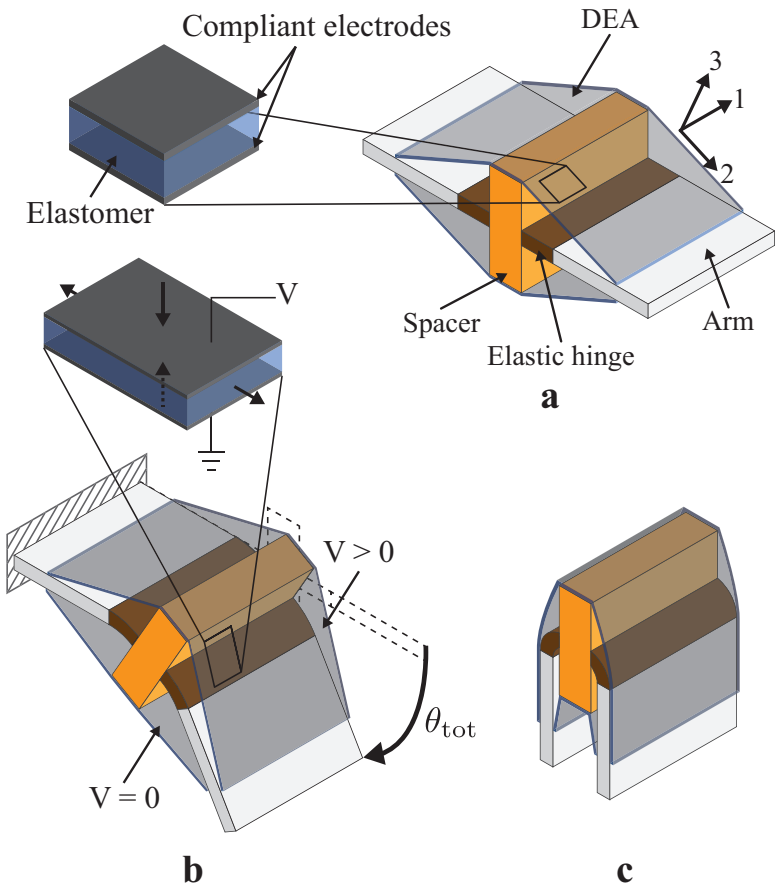

Figure 4.1 – Working mechanism of the foldable antagonistic actuator. (a) The actuator consists of two rigid arms connected via elastic hinges placed symmetrically across the spacer, and two sets of stacked (or single) DEAs forming an antagonistic configuration. (b) When a voltage is applied to only the top or the bottom DEA, the electrostatic pressure causes a biased stress between the DEAs, resulting in a bending movement of the actuator. The stable position is determined by the angle at which the moment generated by the internal stresses in the DEAs and the counter moment in the hinges are equal. (c) The actuator can be passively folded where the internal stress of the DEA and the counter moment in the hinges generate a restoring force.

stress, and causes a biased stress between the DEAs. The biased stress leads to a bending movement of the actuator. The stable position is determined by the angle at which the moment generated by the internal stresses in the DEAs and the counter moment in the hinges are equal. The amount of angular displacement depends on the voltage, the material properties, and the geometry of both the DEAs and the hinges. When the required performance cannot be achieved with a single DEA with fixed geometry, stacking of multiple DEA layers can be used to increase the actuator performance such as the actuation stroke and the force. In Figure 4.1(b), the total angular displacement at the free tip θ_{tot} is twice the displacement obtained around a single hinge.

The force produced at the free tip is determined only by the torque generated in the hinge closest to the fixed boundary, that is, the hinge closest to the free tip does not contribute to the force produced. Therefore the output torque equals the moment of a single hinge with respect to its angular displacement. Due to the antagonistic configuration, the actuation can be done not only by a single voltage input, but also by a combination of voltages on the DEAs on both sides. This suggests that variable mechanical impedance [238] can be achieved where an angular displacement is provided with different output force.

As shown in Figure 4.1(c), the actuator can be passively folded around the hinges. The DEA on the upper side is stretched and its internal stress is used as a restoring force towards the flat state. The counter moment in the hinges also contributes to the restoring force.

4.3 Model

A closed-form analytical model to predict the behavior of the actuator has been constructed based on the total potential energy in the system. The model outputs the total angular displacement θ_{tot} at an equilibrium state for a constant applied voltage V_{s}. From this, the torque is obtained using the torsional spring constant of the elastic hinge. The subscript of variables s stands for either side of the actuator (s = a or b). The subscripts a and b stand for the upper side and the lower side of the actuator across the horizontal line, respectively. As previously mentioned, actuation can be done by a combination of voltages on the DEAs on both sides. However, for the rest of this chapter, the case of a single voltage input is considered ($V_{\text{a}} > 0$ and $V_{\text{b}} = 0$, or $V_{\text{a}} = 0$ and $V_{\text{b}} > 0$). As shown in Figure 4.2, only half of the actuator is considered for the model since the structure is symmetric. The angular displacement θ is determined by calculating the local minimum of the total potential energy U_{tot}.

$$\frac{\partial U_{\text{tot}}}{\partial \theta} = 0, \text{and } \frac{\partial^2 U_{\text{tot}}}{\partial \theta^2} > 0, \tag{4.1}$$

U_{tot} consists of the potential energy of the DEA $U_{\text{DEA\_s}}$ and the elastic energy of the hinge U_{hinge}. Two energies are involved in $U_{\text{DEA\_s}}$: the strain energy of the DEA $U_{\text{strain\_s}}$, and the electrostatic potential energy $U_{\text{electric\_s}}$.

$$U_{\text{tot}} = U_{\text{strain\_a}} + U_{\text{strain\_b}} + U_{\text{electric\_a}} + U_{\text{electric\_b}} + U_{\text{hinge}}, \tag{4.2}$$

where $U_{\text{strain\_s}}$ is a function of the stretch of the DEA elastomer, in which the material property and the geometry are involved. To calculate $U_{\text{strain\_s}}$, the elastomer is assumed to be incompressible (Section 3.1)

$$\lambda_1 \lambda_2 \lambda_3 = \lambda_{1\text{s}} \lambda_{2\text{s}} \lambda_{3\text{s}} = 1, \tag{4.3}$$

where λ_1, λ_2, and λ_3 are the stretch ratios of the elastomer on the direction of 1, 2, and 3 respectively. The stretch ratio is defined as the ratio between the length of a deformed line element and its initial length. For each DEA, direction 1 and direction 2 refer to the planar directions of the DEA, and direction 3 is along the thickness direction. To achieve the constant

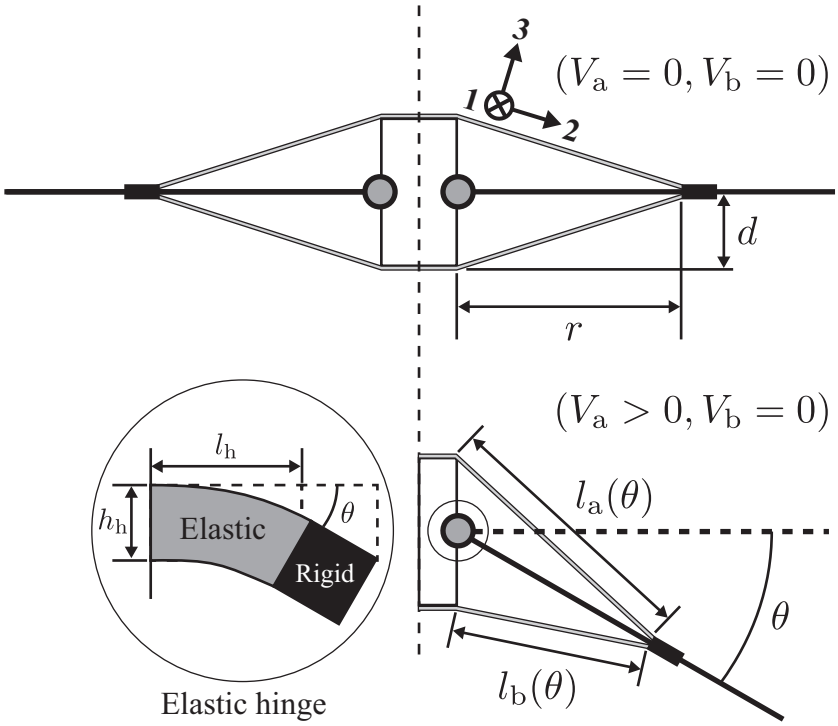

Figure 4.2 – Actuator model schematic. Due to symmetric structure, only half of the actuator is used for the model while the elastic hinge is considered as a pivot.

stretch in direction 1, during the fabrication an elastomer with initial length l_0, initial width w_0, and initial thickness h_0 is pre-stretched uniaxially along direction 1 before attaching to the actuator structure. In this pre-stretched state, the geometry of the DEA is expressed as

$$l'_s = \frac{l_0}{\sqrt{\lambda_{1p}}},\ w'_s = w_0\lambda_{1p},\ h'_s = \frac{h_0}{\sqrt{\lambda_{1p}}}, \tag{4.4}$$

where l'_s, w'_s, and h'_s are the length, the width, and the thickness of the DEA, respectively, pre-stretched in direction 1 with a ratio of λ_{1p}. Since the stretch ratio in direction 1 is constant regardless of the actuation

$$\lambda_{1s} = \lambda_{1p} = \text{constant}. \tag{4.5}$$

The DEA is then attached to the actuator structure with a stretch along direction 2, resulting in the assembled state shown as Figure 4.2. From the figure and Equation 4.4, λ_{2s} is obtained as the total stretch applied in both the pre-stretched state and the assembled state along its

direction, that is:

$$\lambda_{2a}(\theta) = \frac{l_a(\theta)}{l'_s} \cdot \frac{l'_s}{l_0} = \frac{l_a(\theta)}{l_0} = \frac{\sqrt{r^2 + d^2 + 2dr\sin\theta}}{l_0},$$
$$\lambda_{2b}(\theta) = \frac{l_b(\theta)}{l'_s} \cdot \frac{l'_s}{l_0} = \frac{l_b(\theta)}{l_0} = \frac{\sqrt{r^2 + d^2 - 2dr\sin\theta}}{l_0}, \tag{4.6}$$

where $l_a(\theta)$ and $l_b(\theta)$ are the length of the DEA elastomer on each side, r the arm length, and d is the height of the spacer from the arm. The stretch ratio along the thickness direction λ_{3s} is obtained by substituting Equations 4.5 and 4.6 into Equation 4.3

$$\lambda_{3s}(\theta) = \frac{1}{\lambda_{1p}\lambda_{2s}(\theta)}. \tag{4.7}$$

The Yeoh hyperelastic model [240] is used as a strain energy density function W to incorporate the stretch ratios in $U_{\text{strain\_s}}$,

$$W = \sum_{i=1}^{3} C_i (I_1 - 3)^i, \tag{4.8}$$

where C_i are material constants, and $I_1 = \lambda_1^2 + \lambda_2^2 + \lambda_3^2$. By substituting Equations 4.5, 4.6, and 4.7 into Equation 4.8, we get $U_{\text{strain\_s}}$ as

$$U_{\text{strain\_s}}(\theta) = N_s \cdot Vol \cdot W_s(\theta) = N_s \cdot Vol \cdot \sum_{i=1}^{3} C_i (I_{1s}(\theta) - 3)^i,$$
$$I_{1s}(\theta) = \lambda_{1p}^2 + \{\lambda_{2s}(\theta)\}^2 + \left\{\frac{1}{\lambda_{1p}\lambda_{2s}(\theta)}\right\}^2, \tag{4.9}$$
$$Vol = l_0 w_0 h_0,$$

where Vol is the volume of each DEA. Since the DEA can be stacked, the number of DEAs on each actuator side is taken into account as N_s.

As the DEA can be considered as a capacitor, the electrostatic potential energy $U_{\text{electric\_s}}$ is derived as

$$U_{\text{electric\_s}} = -N_s \frac{1}{2} C_s V_s^2 = -N_s \frac{1}{2} \varepsilon_0 \varepsilon_r \frac{A_{\text{e\_s}}}{h_s} V_s^2, \tag{4.10}$$

where C_s is the capacitance, ε_0 the permittivity of free space, ε_r the relative permittivity of the elastomer, $A_{\text{e\_s}}$ the area of the electrode, and h_s is the thickness of the elastomer. $U_{\text{electric\_s}}$ is negative because the voltage-controlled case [272] is taken into account. As the actuator

moves with θ, $A_{\mathrm{e\_s}}$ and h_{s} change corresponding to the stretch ratios, that is

$$\begin{aligned} A_{\mathrm{e\_s}}(\theta) &= l_{\mathrm{e\_s}}(\theta)\, w_{\mathrm{e}} = l_{\mathrm{e0}} \lambda_{2\mathrm{s}}(\theta)\, w_{\mathrm{e}}, \\ h_{\mathrm{s}}(\theta) &= h_0 \lambda_{3\mathrm{s}}(\theta) = \frac{h_0}{\lambda_{1\mathrm{p}} \lambda_{2\mathrm{s}}(\theta)}, \end{aligned} \tag{4.11}$$

where $l_{\mathrm{e\_s}}$ and w_{e} are the length of the electrode and its width, respectively, and l_{e0} is the electrode initial length. By substituting Equation 4.11 into Equation 4.10, $U_{\mathrm{electric\_s}}$ is represented as a function of θ:

$$U_{\mathrm{electric\_s}}(\theta) = -N_{\mathrm{s}} \frac{1}{2} \varepsilon_0 \varepsilon_{\mathrm{r}} l_{\mathrm{e0}}\, w_{\mathrm{e}} \lambda_{1\mathrm{p}} \{\lambda_{2\mathrm{s}}(\theta)\}^2 \frac{V_{\mathrm{s}}^2}{h_0} \tag{4.12}$$

The elastic energy of the hinge, U_{hinge}, is obtained using the torsional spring stiffness k and θ,

$$U_{\mathrm{hinge}}(\theta) = \frac{1}{2} k \theta^2, \tag{4.13}$$

where k can be derived based on the small-length flexural pivot approximation from elementary beam theory [241, 242]

$$k = \frac{E_{\mathrm{h}} I_{\mathrm{h}}}{l_{\mathrm{h}}} = \frac{E_{\mathrm{h}}\, w_{\mathrm{h}} h_{\mathrm{h}}^3}{12 l_{\mathrm{h}}}, \tag{4.14}$$

where E_{h} and l_{h} are the elastic modulus of the hinge and its length, respectively, and I_{h} is the second moment of area. I_{h} is calculated using the width of the hinge w_{h} and its thickness h_{h}.

As the energies $U_{\mathrm{strain\_s}}$, $U_{\mathrm{electric\_s}}$, and U_{hinge} are functions of θ, Equation 4.1 becomes a differentiation of U_{tot} with respect to θ, that is

$$\frac{dU_{\mathrm{tot}}}{d\theta} = \frac{dU_{\mathrm{strain\_a}}}{d\theta} + \frac{dU_{\mathrm{strain\_b}}}{d\theta} + \frac{dU_{\mathrm{electric\_a}}}{d\theta} + \frac{dU_{\mathrm{electric\_b}}}{d\theta} + \frac{dU_{\mathrm{hinge}}}{d\theta} = 0 \tag{4.15}$$

By differentiating Equations 4.9, 4.12, and 4.13 with respect to θ, each term in Equation 4.15 is derived as

$$\begin{aligned} \frac{dU_{\mathrm{strain\_a}}}{d\theta} &= 2N_{\mathrm{a}} \frac{w_0 h_0}{l_0} \left(1 - \frac{1}{\lambda_{1\mathrm{p}}^2 \{\lambda_{2\mathrm{a}}(\theta)\}^4}\right) \\ &\quad \times \left\{C_1 + 2C_2(I_{1\mathrm{a}} - 3) + 3C_3(I_{1\mathrm{a}} - 3)^2\right\} dr \cos\theta \end{aligned} \tag{4.16}$$

$$\begin{aligned} \frac{dU_{\mathrm{strain\_b}}}{d\theta} &= -2N_{\mathrm{b}} \frac{w_0 h_0}{l_0} \left(1 - \frac{1}{\lambda_{1\mathrm{p}}^2 \{\lambda_{2\mathrm{b}}(\theta)\}^4}\right) \\ &\quad \times \left\{C_1 + 2C_2(I_{1\mathrm{b}} - 3) + 3C_3(I_{1\mathrm{b}} - 3)^2\right\} dr \cos\theta \end{aligned} \tag{4.17}$$

$$\frac{dU_{\text{electric\_a}}}{d\theta} = -N_{\text{a}} \frac{\varepsilon_0 \varepsilon_{\text{r}} l_{\text{e0}} w_{\text{e}}}{l_0^2 h_0} \lambda_{1\text{p}} V_{\text{a}}^2 dr \cos\theta \tag{4.18}$$

$$\frac{dU_{\text{electric\_b}}}{d\theta} = N_{\text{b}} \frac{\varepsilon_0 \varepsilon_{\text{r}} l_{\text{e0}} w_{\text{e}}}{l_0^2 h_0} \lambda_{1\text{p}} V_{\text{b}}^2 dr \cos\theta \tag{4.19}$$

$$\frac{dU_{\text{hinge}}}{d\theta} = \frac{E_{\text{h}} w_{\text{h}} h_{\text{h}}^3}{12 l_{\text{h}}} \theta \tag{4.20}$$

By solving Equation 4.15, we find θ as a function of the applied voltage V_{s}, that is, $\theta = \theta(V_{\text{s}})$. As described in the previous subsection, the total angular displacement of the actuator θ_{tot} is twice the displacement obtained around a single hinge, therefore, $\theta_{\text{tot}}(V_{\text{s}}) = 2\theta(V_{\text{s}})$.

The torque τ equals the moment in a single hinge and is a function of V_{s} in the case where the actuator tip is free to move.

$$\tau(V_{\text{s}}) = k\theta(V_{\text{s}}) \tag{4.21}$$

When the tip is blocked with a fixed angular displacement ϕ, τ is obtained as

$$\tau(V_{\text{s}}, \phi) = k\left\{\theta(V_{\text{s}}) - \phi\right\} \tag{4.22}$$

In Equation 4.22, τ is assumed that it can be approximated to the value in the case of the free tip.

4.4 Fabrication

The desired specifications of performance and geometry of the actuator are obtained from the design process of the MAV described in Section 4.6. The actuator is used as an elevon in the MAV and consists of a control surface and a base fixed onto the MAV airframe, which correspond to the arm parts shown in Figure 4.1(a).

Here the fabrication process is presented. The materials used for the fabrication are selected due to their lightweight property to minimize effects of both gravity and accelerations on the actuator movement. Firstly a silicone elastomer (NuSil Technology, CF19-2186) is chosen for the DEA membrane. The elastomer is mixed with a solvent (iso-octane) at a 2:1 weight ratio respectively, and the mixture is coated on a film substrate using an automatic film applicator coater (Zehntner, ZAA2300) with a thickness given by a universal applicator (Zehntner, ZUA2000). After curing for 12 hours at room temperature, an elastomer membrane with thickness of approximately 125 μm is formed on the substrate.

The membrane is then cut into 80 mm long by 80 mm wide sections, peeled from the substrate, adhered to two rigid holders, and pre-stretched uniaxially to a ratio of 2, as shown in Figure 4.3(a). After that the sample is held by a supporting rack. The electrodes are subsequently patterned onto the membrane surface (Figure 4.3(b)) using the pad-printing method. The compliant electrodes are consist of carbon nanoparticles (Cabot black pearls 2000, and AkzoNobel Ketjenblack EC-300J) mixed with a soft silicone (Bluestar Silicones Silbione LSR 4305, 0.2 MPa of elastic modulus [126]) at a mass ratio of 1:10. This electrode composition is used for the other actuators described in Section 5 and Section 6. The sample is cured for 1 hour at 75 °C after patterning one side, and the process is repeated on the other side of the membrane.

After curing, frames made of a 0.2 mm thick fiberglass plate are attached to the membrane surface (Figure 4.3(c)) using a silicone adhesive film (Adhesives Research, ARclear-8932) to keep the pre-stretched state. One of the frame parts has a hole to make an electrical contact to the electrode. Additionally, a silicone glue is put on the edge of the frames to prevent the membrane from peeling. The sample is then cut from the supporting rack, and attached to the actuator frame (Figure 4.3(d)). The actuator frame is composed of two fiberglass plates of thickness 0.2 mm and 1 mm, which are used as the arms (a control surface and a base) and the spacer, respectively, and a 50 μm thick polyimide (PI) film (UBE, UPILEX-50S) as the elastic hinges. The silicone adhesive film is used to attach them. The electrical contact is made via the hole of the frame, using a conductive lacquer (amepox, ELECTON 40AC) and a conductive tape.

Figure 4.4(a) shows the fabricated elevon actuator. The actuator consists of a control surface and a base as the arm parts. Figure 4.4(b) shows the actuator in integrated state. The base part is connected to the MAV airframe. Figure 4.4(c) shows the folded state of the actuator. The design parameters used for the actuator are summarized in Table 4.1 together with the specifications. In this table, the material constants C_i used in Equations 4.16 and 4.17 are determined by fitting Equation 4.8 to the experimental stress-strain curve obtained from a uniaxial pull test (Noorwood, Instron 3343).

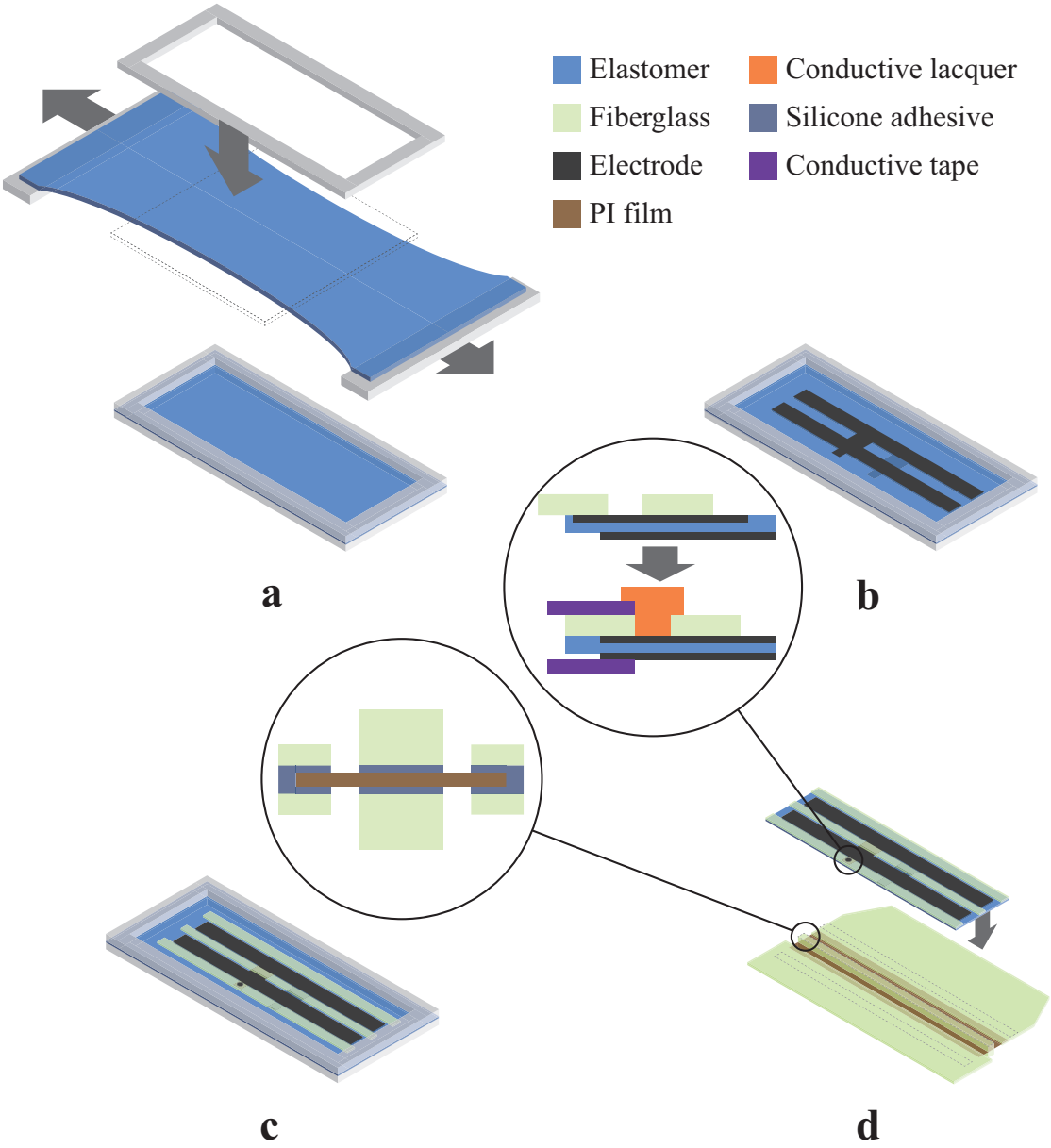

Figure 4.3 – Fabrication process of the actuator. (a) The elastomer is cut and peeled from a film substrate, pre-stretched uniaxially to a ratio of 2, and held by a supporting rack. (b) The electrodes are patterned on both side of the membrane via a stamping method. (c) Frames made of a fiberglass plate are attached on to the surface to keep the pre-stretched state. One of the frames has a hole for electrical contact. (d) The sample is then cut from the supporting rack and attached onto the actuator frame. The electrical contact is realized via a hole filled with a conductive lacquer and a conductive tape.

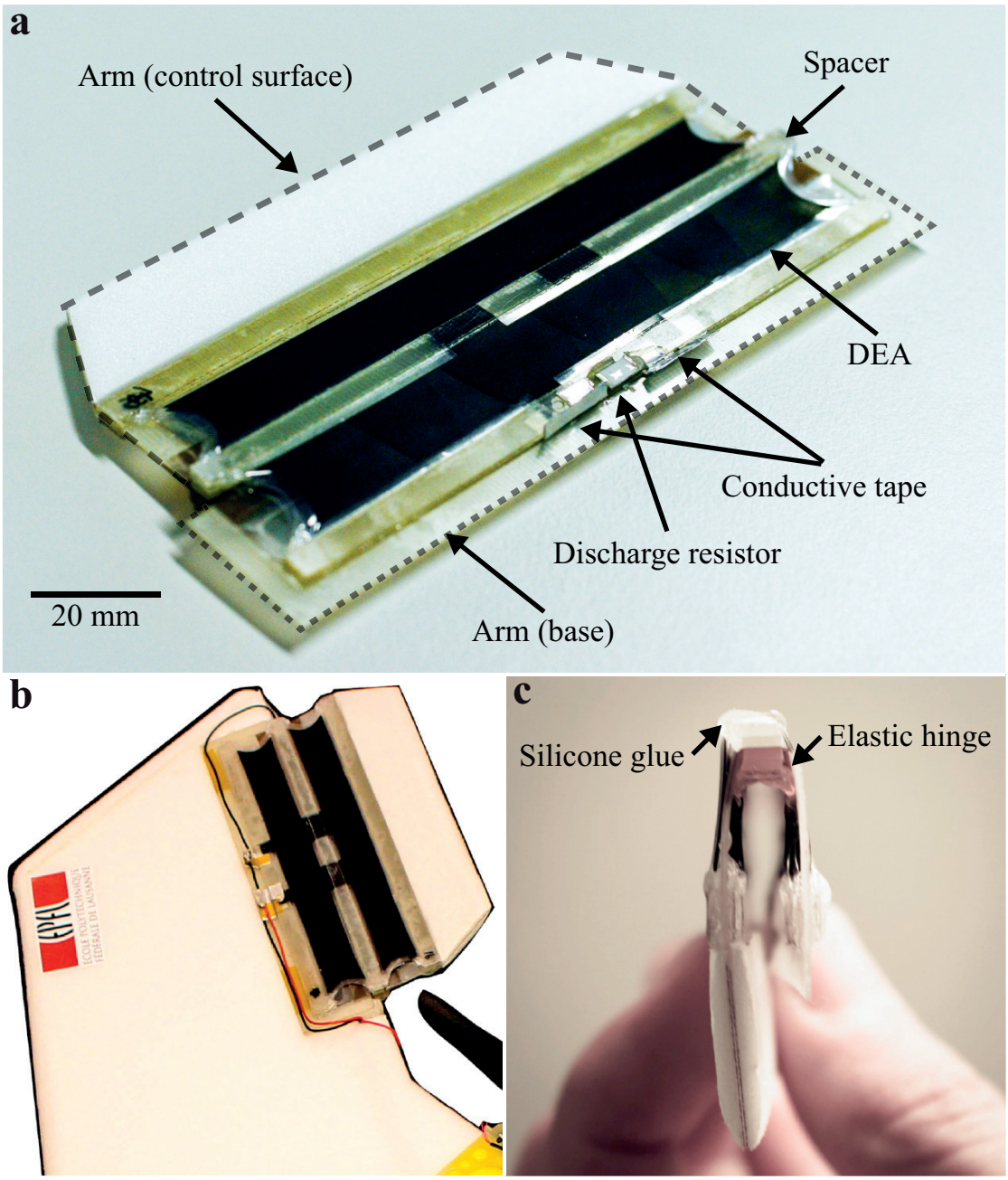

Figure 4.4 – Fabricated elevon actuator. (a) The actuator frame consists of two arm parts across the spacer: a control surface and a base. A resistor is connected between the conductive tape to discharge the DEA. (b) Integrated state of the actuator. The base part is connected to the MAV airframe. (c) Folded state of the actuator. Silicone glue put on the frame edge prevents peeling of the DEA membrane.

Table 4.1 – Design parameters and specifications of the elevon actuator

Design parameter	Value
Dimensions	
DEA (half part)	
Initial length l_0	14.1 mm
Initial width w_0	60 mm
Initial thickness h_0	125 µm
DEA electrode (half part)	
Initial length l_{e0}	11.3 mm
Width w_e	112 mm
Frame	
Arm length r	14.5 mm
Spacer height d [*1]	1.840 mm (1 DEA)
	2.025 mm (2 DEAs)
Spacer area (length × width)	4 mm × 120 mm
Elastic hinge	
Length l_h	1.0 mm
Width w_h	120 mm
Thickness h_h	50 µm
Silicone adhesive film	
Thickness	40 µm
Material property	
DEA elastomer	
Relative permittivity ε_r	2.8 [233],[243]
Material constant C_1	0.105 MPa
Material constant C_2	0.00332 MPa
Material constant C_3	1.44×10^{-13} MPa
Elastic hinge	
Elastic modulus E_h [*2]	9.1 GPa
Other parameter	
Pre-stretch ratio λ_{1p}	2.0
Permittivity of free space ε_0	8.85×10^{-12} F/m
Specifications	
Mass	14.4 g
Base area (length × width)	24 mm × 130 mm
Control surface area (length × width)	40 mm × 120 mm

[*1] Values are calculated as a composite of the fiberglass plate and the silicone adhesive film. The value of 2 DEAs is taken from the medium height between both the DEAs.

[*2] According to the property of UPILEX-S presented on the manufacturer's web site: http://www.ube.com/

4.5 Characterization

4.5.1 Experimental Setup

Two types of actuator samples are prepared: one consists of 1 DEA on each side, and the other has 2 DEAs (in Equations 4.16 - 4.19, $N_s = 1$ and $N_s = 2$). For each type, 3 samples are prepared and the average of the measured value is taken. During the characterization, the total angular displacement θ_{tot} ($= 2\theta$ in the model) and the blocked torque τ (in Equation 4.22, $\phi = 0$) are measured. The samples are fixed at the base with the direction minimizing gravity effects as shown in Figure 4.5(a) inset. The displacement of the control surface tip is measured as the angular displacement. A CMOS camera (Point Grey, FMVU-13S2C) with image processing is used to measure the tip angle, and the torque is obtained by measuring the blocked force at the actuator tip using a load cell (FUTEK, LRF400). As shown in Figure 4.5(b) inset, the probe of the load cell is attached to the tip prior to activating the actuator. The torque τ is then calculated from the measured force F and the moment arm length R as $\tau = R \cdot F$. Since the structure of the actuator is symmetric, only one side of the DEA is actuated with a voltage up to 5 kV using a high-voltage DC supply (Auckland Biomimetics Lab, EAP controller).

4.5.2 Results

The measured angular displacements from the initial position, and the model predictions as functions of the applied voltage are shown in Figure 4.5(a). The observed angular displacement at 5 kV is 16.9 ± 1.5 ° for the 1 DEA actuator, and 26.1 ± 1.6 ° for the 2 DEAs actuator. Figure 4.5(b) shows the measured blocked torque and the model prediction as functions of the applied voltage. The observed torque at 5 kV is 1480 ± 60 mN · mm for the 1 DEA actuator, and 2720 ± 260 mN · mm for the 2 DEAs actuator.

In these figures, as the model predicted, the actuator performance changes with the applied voltage non-linearly, and the number of DEAs on each side affects the performance directly. The model prediction shows good agreement to the measured data. The error between the model prediction and measured data may have resulted from the fact that the model does not account for the Mullins effect [244, 245], the softening of the elastomer due to the pre-stretch and the actuation stretch. The presence of the electrode elastomer, which is not accounted for in the model, would also decrease the actuation stretch. Furthermore, the actuator frame is not perfectly rigid so it may buckle when actuated, which could reduce the blocked force measured and therefore the torque. The error is larger in the case of the 2 DEAs actuator. This may have resulted from the fact that the geometry of each DEA is slightly different due to fabrication error, which would increase the error with number of DEAs attached to the actuator. Also, alignment error of those DEAs may raise the deviation between the model prediction and the measured data.

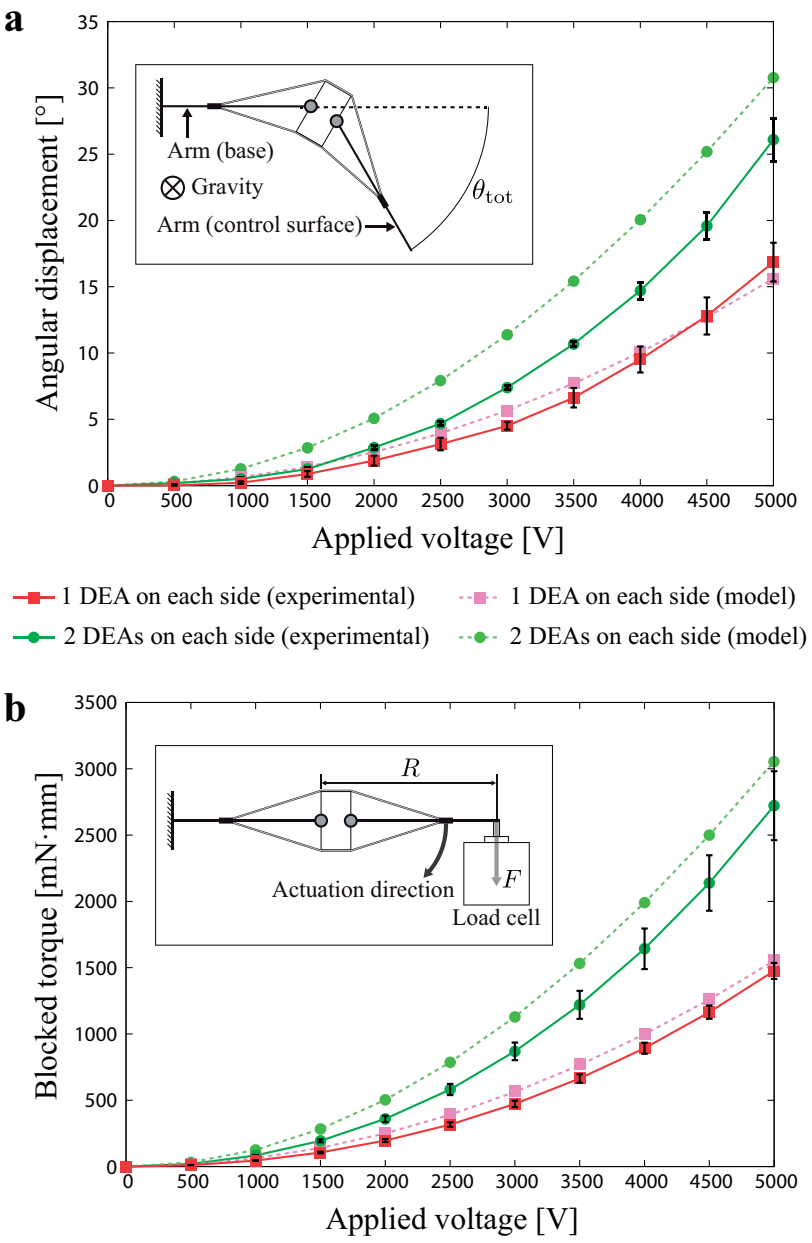

Figure 4.5 – Characterization results of two types of actuator samples: one consists of 1 DEA on each side, and the other has 2 DEAs. Only one side of the DEA is actuated for all the samples. (a) Measured total angular displacement of one tip fixed condition and model prediction. The inset shows the measurement condition. The total angular displacement θ_{tot} (= 2θ in the model) is obtained as the angular displacement of the control surface tip. The base tip is fixed. The observed angular displacement at 5 kV is 16.9 ± 1.5 ° for the 1 DEA actuator, and 26.1 ± 1.6 ° for the 2 DEAs actuator. (b) Measured blocked torque (in Equation 4.22, $\phi = 0$) and model prediction. The inset shows the measurement condition. The blocked torque is obtained by measuring the blocked force. At a non-actuated state, the probe of the load cell is attached to the tip and subsequently the actuation voltage is applied. From the measured force, the torque is calculated using the moment arm length R (in Equation 4.22, $\phi = 0$). The observed torque at 5 kV is 1480 ± 60 mN · mm for the 1 DEA actuator, and 2720 ± 260 mN · mm for the 2 DEAs actuator.

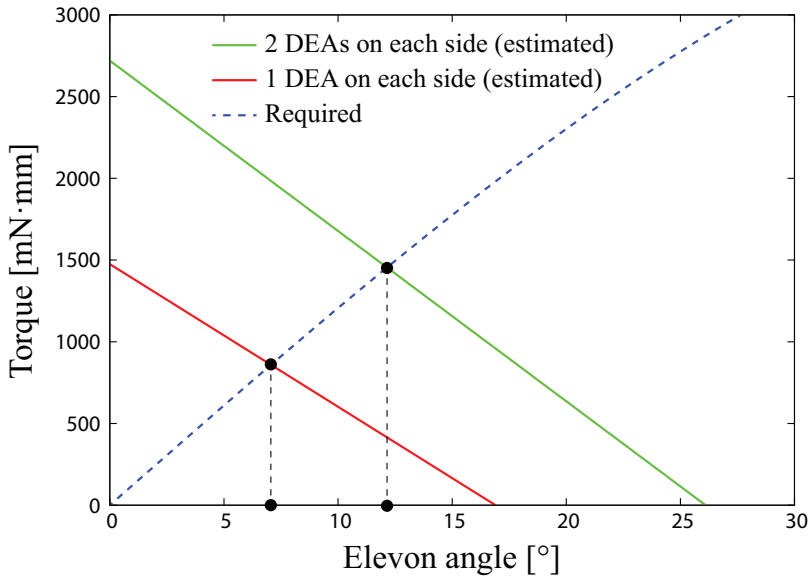

Figure 4.6 – Estimated torque as a function of the elevon angle at the applied voltage of 5 kV for the 1 DEA and the 2 DEAs actuators. The required torque as a function of the elevon angle is also plotted. The intersection of these lines gives the maximum elevon angle that can be achieved by the actuator during a flight.

The result is evaluated to see if the actuator satisfies the required torque of 1780 mN · mm with elevon angle of 15 ° obtained in the following Section 4.6. The torque characteristics are assumed to be the same regardless of load condition (airflow). This assumption is expressed in Equation 4.22 in Section 4.3. In this case, the torque generated at an elevon angle and a fixed applied voltage is represented as a linear function of the evevon angle. The slope is defined as the measured value of both the torque and the elevon angle. Figure 4.6 plots the torque as a function of the elevon angle at the applied voltage of 5 kV for the 1 DEA and the 2 DEAs actuators. The requid torque as a function of the elevon angle, obtained from Equation 4.27 in Section 4.6, is also presented in this figure. The intersection of those lines gives the maximum elevon angle that can be achieved by the actuator during a flight. For the MAV, the actuator composed of 2 DEAs on each side is used. Because it is assumed that flight of the MAV can be performed with this actuator, as it is expected to generate ~12.5 ° of the elevon angle, which is only slightly lower than the required value.

4.6 Micro Air Vehicle

A remotely controlled fixed wing MAV is developed as an application to validate the actuator. The actuator is used as an elevon and evaluated in terms of the controllability of the MAV. The correlation between the control signal and the angular velocity of the MAV motion is calculated as the evaluation.

4.6.1 Airframe and Actuator Design

The design of the airframe includes the determination of the actuator specifications from the wing geometry together with the required actuator torque. Figure 4.7(a) shows the designed geometry of the airframe. A tailless shape is used for the airframe due to its simpler form. On the airframe, two actuators are used as elevons. The wing geometry is obtained by scaling down the Swift II (MS Composit), a successful commercial model. During a flight, the actuator has to sustain an elevon angle with a torque against the airflow where the aerodynamic force is acting on its surface. The required torque is calculated using the flight speed (i.e., the airflow), the elevon control surface, and the elevon angle. During a flight, the mass of the MAV equals the lift force F_{lift} [246]

$$F_{\text{lift}} = \frac{1}{2} C_{\text{L}} \rho_{\text{air}} S V^2 = mg, \tag{4.23}$$

where C_{L} is the lift coefficient, ρ_{air} the air density, S the wing area, V the flight speed, m the mass, and g is gravity. C_{L} can be obtained as $C_{\text{L}} = 2\pi\alpha$, and α is the angle of attack of the wing. Equation 4.23 can be rewritten as

$$V = \sqrt{\frac{2mg}{C_{\text{L}} \rho_{\text{air}} S}}. \tag{4.24}$$

Equation 4.24 gives the flight speed V for a given S, C_{L}(i.e., α), and m. The wing area S is a function of the wingspan b for a fixed wing geometry, that is, $S = S(b)$. The MAV mass m is estimated from the wing mass m_{wing} and the total mass of the necessary components m_{comp}, including the actuators (estimated value), a motor, batteries, a receiver, etc.

$$\begin{aligned} m &= m_{\text{wing}} + m_{\text{comp}}, \\ m_{\text{wing}} &= \rho_{\text{w}} h S(b), \end{aligned} \tag{4.25}$$

where ρ_{w} and h are the density of the wing material and the thickness of the wing, respectively. A 5 mm thick styrofoam (Depron) is used as an airframe material. The second expression in Equation 4.25 is valid when the airfoil shape is a plate, as in our case. From the above, V is expressed as a function of b for a fixed value of α

$$V(b) = \sqrt{\frac{\rho_{\text{w}} h S(b) + m_{\text{comp}}}{\pi \alpha \rho_{\text{air}} S(b)} g}. \tag{4.26}$$

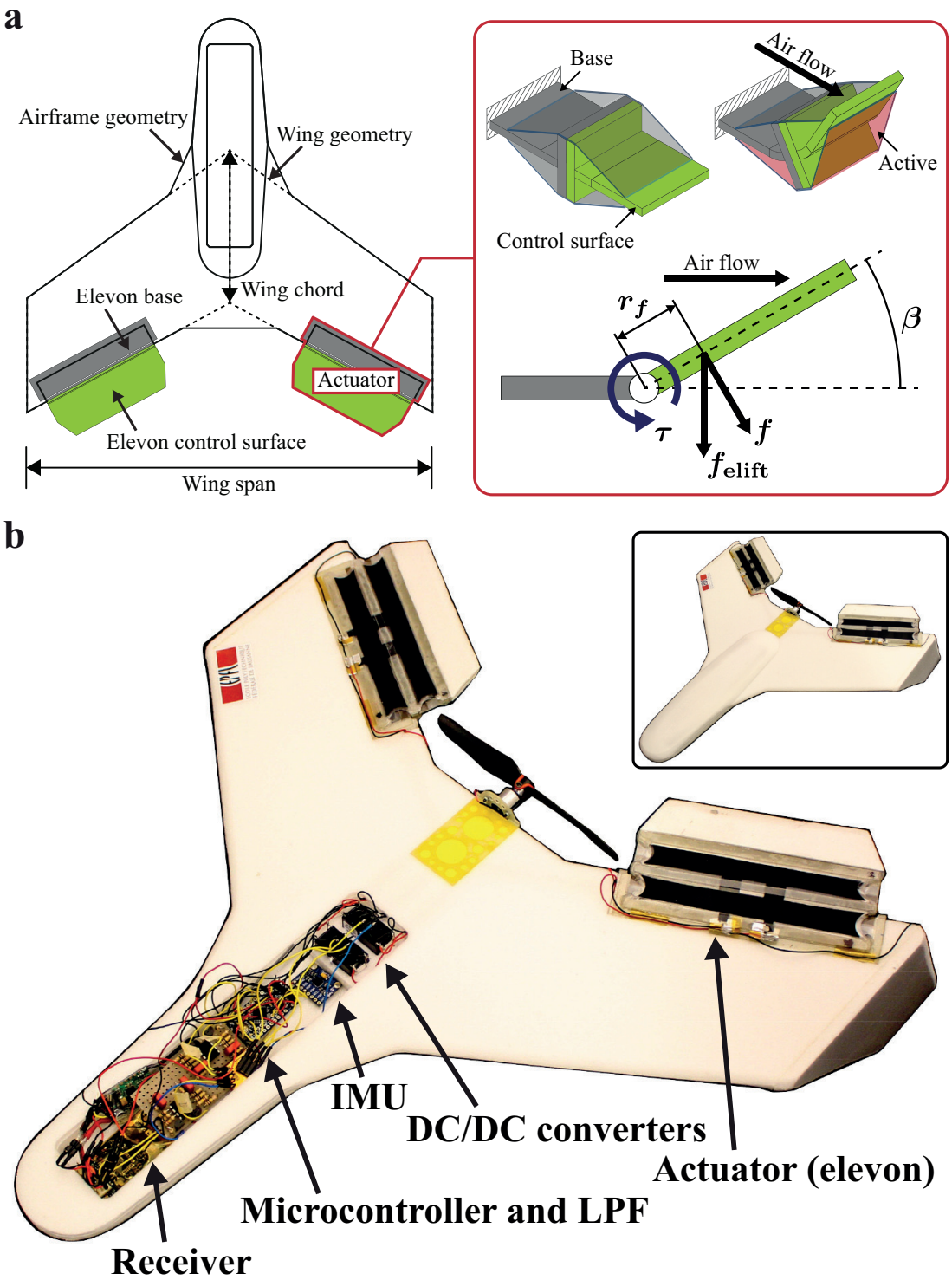

Figure 4.7 – (a) Schematic of the airframe. The elevon control surface is determined from a ratio of the wing geometry. The required torque τ is obtained as the counter torque against the aerodynamic force f acting on the control surface with an elevon angle β. (b) Fabricated MAV (without the cover). The actuators are placed with mounting angle of 10 ° to ensure the longitudinal static stability. The inset shows the MAV with the cover.

Equation 4.26 shows larger S results in lower V. b is chosen so that V is in a range of 5-10 m/s, which is moderate wind on the earth [247]. This flight speed value is expected to generate a resistance to subtle wind (1-5 m/s) in which flight of the MAV is assumed to be performed. For alpha, a value of 7.5 ° is taken. The value of the flight speed V determined is 6.14 m/s for the wingspan $b = 400$ mm.

The design process of the airframe described above is a simplified form to determine the flight speed for obtaining the actuator specification. For example, the process does not consider the balance between the motor output power and the MAV mass. For further optimized airframe design, a detailed evaluation based on more paramters is required. Example of such evaluation is mass-power balance itaration using mass and power models [248].

Next, the required torque of the actuator is determined. As shown in Figure 4.7(a) and explained in Section 4.4, in the actuator one of the arm parts is used as the control surface while the other is used as the base. The required torque τ is obtained as the counter torque against the aerodynamic force acting on the control surface with an elevon angle

$$\begin{aligned} \tau &= r_f \cdot f, \\ f &= f_{\mathrm{elift}} \cos\beta, \\ f_{\mathrm{elift}} &= \frac{1}{2} C_{\mathrm{Le}} \rho_{\mathrm{air}} S_{\mathrm{e}} V^2, \end{aligned} \tag{4.27}$$

where f, f_{elift}, and r_f are the aerodynamic force, the elevon lift force, and their position in the chord, respectively, β the maximum elevon angle, C_{Le} the lift coefficient of the elevon ($C_{\mathrm{Le}} = 2\pi\beta$), and S_{e} is the control surface area. S_{e} is obtained from a ratio of the wing geometry shown in Figure 4.7(a): 30 % of the wingspan and 25 % of the aerodynamic mean chord†. r_f can be approximated as 25 % of the elevon chord (the aerodynamic pressure [246]), and the aerodynamic force f is assumed to be perpendicular to the elevon is a vector component of the lift force f_{elift}. 15 ° is used for β because experimental results on thin wings at low-Reynolds number have shown that the lift coefficient is linear within this region [249]. The value of the required torque τ determined is 1780 mN · mm. The elevon geometry (i.e., S_{e}) is then used as the specification of the actuator.

Figure 4.7(b) shows the fabricated MAV. The nose of the airframe is extended to install the control system. The actuators are placed with a biased mounting angle of 10 ° to ensure the longitudinal static stability as explained in Subsection 4.6.3. The vertical tails are put downward to prevent damage to the actuators at landing. The measured mass of the MAV is 130.7 g, which is heavier than the estimated mass. This is due to the additional mass mostly resulted from the airframe extension, the elevon mounting parts, and underestimation of the actuator mass. The required actuator torque determined from the estimated mass is assumed to be sufficient to control the MAV, as the impact of the additional mass on the flight speed is reasonably low (7.02 m/s). The specifications and the design parameters of the MAV, and the determined values are summarized in Table 4.2.

Table 4.2 – Specifications and design parameters of the MAV, and determined values

Specification	Value
Dimensions	
Wing span b	400 mm
Wing chord (center) C_1	150 mm
Wing thickness h	5 mm
Wing area S	0.0525 m^2
Elevon control surface area S_e	0.0043 m^2
Elevon aerodynamic force position r_f	10.7 mm
Other	
Air density ρ_{air}	1.2041 kg/m^3
Wing material density ρ_w *	33 kg/m^3
Gravity g	9.8 m/s^2
Angle of attack of the wing α	7.5 °
Maximum elevon angle β	15 °
Estimated mass m	100 g
Measured mass	130.7 g
Determined flight speed V based on m	6.14 m/s
Determined required torque τ	1780 mN·mm

* According to the property of Depron presented on the manufacturer's web site: http://www.depronfoam.com/

†The aerodynamic mean chord C_{MAC} is calculated as $C_{MAC} = 2C_1(1 + t + t^2)/3(1 + t)$, where t is the ratio between the wing center chord C_1 and the wing edge chord C_2, that is, $t = C_2/C_1$ [246].

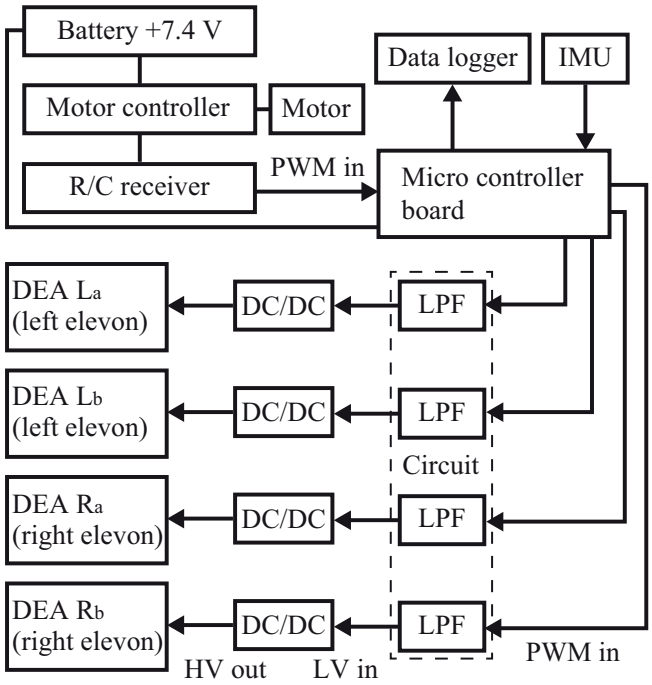

Figure 4.8 – Control system of the MAV. The control signal from the receiver is converted to a high-voltage actuation signal for the DEAs via the micro controller, the LPF circuit, and the DC/DC converters.

4.6.2 Control System

The DEAs used for the actuator require high-voltage actuation signals, therefore a dedicated control system is necessary for the MAV. Figure 4.8 shows the outline of the control system. When a control signal is sent from the transmitter, the receiver (Futaba, R617FS) outputs a PWM signal, which is then processed via the micro controller board (SparkFun, Arduino Pro Mini 328) to 4 outputs corresponding to DEAs placed in the actuators. Subsequently, the outputs are low-pass filtered to a low DC signal from PWM, and then the high-voltage signal is generated through the DC/DC converters (EMCO, Q-50, power 0.5 W). Finally, a high voltage output proportional to the low voltage input is applied to the DEAs, up to a maximum of 5 kV. An IMU board (Kootek, GY-521) consisted of accelerometer and gyroscope is used to measure the motion of the MAV. During a flight, the sensor values are recorded together with the control signal by a data logger (SparkFun, DEV-09530). Since the data is analyzed offline, the IMU in this system is not related to the control of the MAV.

From the point of view of the actuation, the resistor connected to the DEA dissipates power from the DC/DC converter when the DEA is actuated, which is dominant power consumption. As shown in Figure 4.8, there are 4 DC/DC converters in the MAV, and two of them are activated at same time for every maneuver. Thus, during a flight if the DEAs are actuated with maximum voltage all the time, the power consumption is approximated as ~1 W. This value is assumed to be acceptable for the MAV since the power consumption of the motor (HobbyKing, AP05 3000kv) is approximated as ~22 W (calculated from the maximum current 3 A with driving voltage 7.4 V), which is dominant in the entire system.

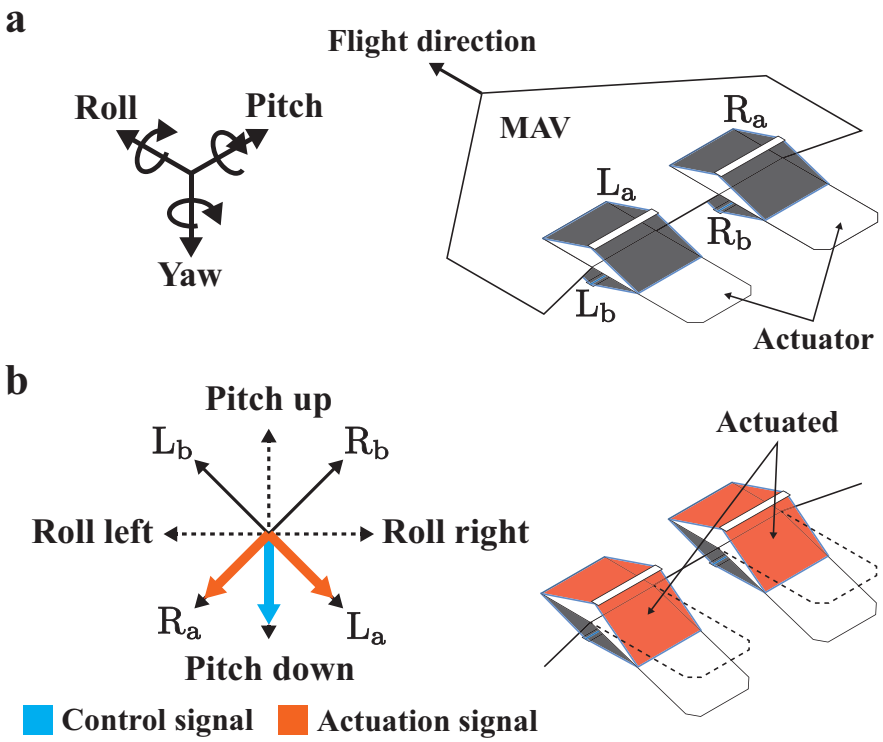

Figure 4.9 – Control and actuation signal relation. (a) There are 4 DEAs forming the elevons. L_a and L_b for the left elevon, R_a and R_b for the right elevon, respectively. (b) The control signal is split out to generate the actuation signal for those DEAs. In this case, L_a and R_a are actuated corresponding to a pitch down control signal.

Table 4.3 – MAV control signal vs. actuated DEA

Control signal	DEA L_a	DEA L_b	DEA R_a	DEA R_b
Pitch up	−	+	−	+
Pitch down	+	−	+	−
Roll left	−	+	+	−
Roll right	+	−	−	+

+:actuated -:not actuated

The control signal of the MAV consists of two channels: the pitch and the roll. As shown in Figure 4.9(a), there are 4 DEAs as L_a and L_b for the left elevon, and R_a and R_b for the right elevon, respectively. Figure 4.9(b) represents what appears when a pitch down is input. In this figure the control signal and the actuation signal are normalized with respect to their maximum values, which are represented by the arrows. The signal is split out to two actuation signals and then L_a and R_a are actuated, resulting in a down angle of both elevons which produces a nose-down pitch movement of the MAV during a flight. Table 4.3 summarizes the relation between the control signals and the corresponding actuated DEAs. For other cases, such as a combination of pitch and roll, actuation signal differences between L_a and L_b, and between R_a and R_b are applied.

4.6.3 Results

A flight of 150 seconds is performed, including an arm throw takeoff and a ground landing. During the flight, the MAV attitude control is achieved only by the elevon actuators via a remote controller with a human pilot. The data recorded during the flight has noise, which mostly comes from the motor. To suppress the noise, the data is smoothed with a Low-Pass Filter (LPF) with a cutoff frequency of 1 Hz. The filtered data range is a few seconds shorter than the flight time to avoid high-noise coming from the takeoff acceleration and the landing deceleration. The bias errors of the IMU are removed.

The filtered data is then compared with the control signal, as shown in Figure 4.10(a). The angular values refer to the coordinates shown in Figure 4.9(a). The data on the yaw axis is not considered because it is a secondary factor based on the other two axes. The control signals are normalized with respect to their maximum value. The roll angular velocity visibly follows the control signal while the pitch angular velocity shows low matching. The pitch angular velocity seems to be shifted positively. This is due to the fact that the MAV requires the pitch up angular velocity for turning, in addition to the roll and the yaw angular velocity. The correlation between the angular velocities and the control signals is 0.723 for the roll, and 0.198 for the pitch.

The actuators controlled the MAV in the desired direction. This is obvious from the fact that the angular velocities, especially in the roll, visibly follow the control signal. This results in a strong correlation and therefore high controllability on this axis. Figure 4.10(b) shows the flight trajectory of the MAV determined using the extended Kalman filter (EKF) [250, 251, 252] with the raw data of both the accelerometer and the gyroscope, while the flight speed is assumed to be constant, since the motor throttle is fixed during the flight except for the takeoff and the landing. The trajectory reflects the control signal (i.e. the will of the pilot), and forms a range where the MAV can be visually controlled.

Figure 4.11 is a turning sequence of the MAV during the flight. During the turn, the actuators well control and stabilize the MAV attitude. Note that in Figure 4.11, the time frame is different from that of Figure 4.10. A flight movie of the MAV can be seen on [253].

The poor correlation with the pitch may have resulted from a strong longitudinal static stability of the MAV. The longitudinal static stability is necessary to keep the MAV attitude stable against disturbance (e.g., wind). Figure 4.12(a)(i) represents the MAV in steady flight. The static stability is achieved by the lift force and the aerodynamic force on the elevon actuators. Their moments around the center of gravity (COG) stabilize the MAV on the pitch axis. This inherent stabilization may resist controllability on this axis. Additionally, as shown in Figure 4.12(a)(ii), due to the biased angle, the elevon surface exposed to the airflow is smaller at the pitch down, therefore low controllability in this direction is expected. The swept wing of the MAV also stabilizes the attitude along the roll axis. Nevertheless, the correlation of this axis is strong, suggesting that the elevon actuator has adequate performance for aerodynamic control.

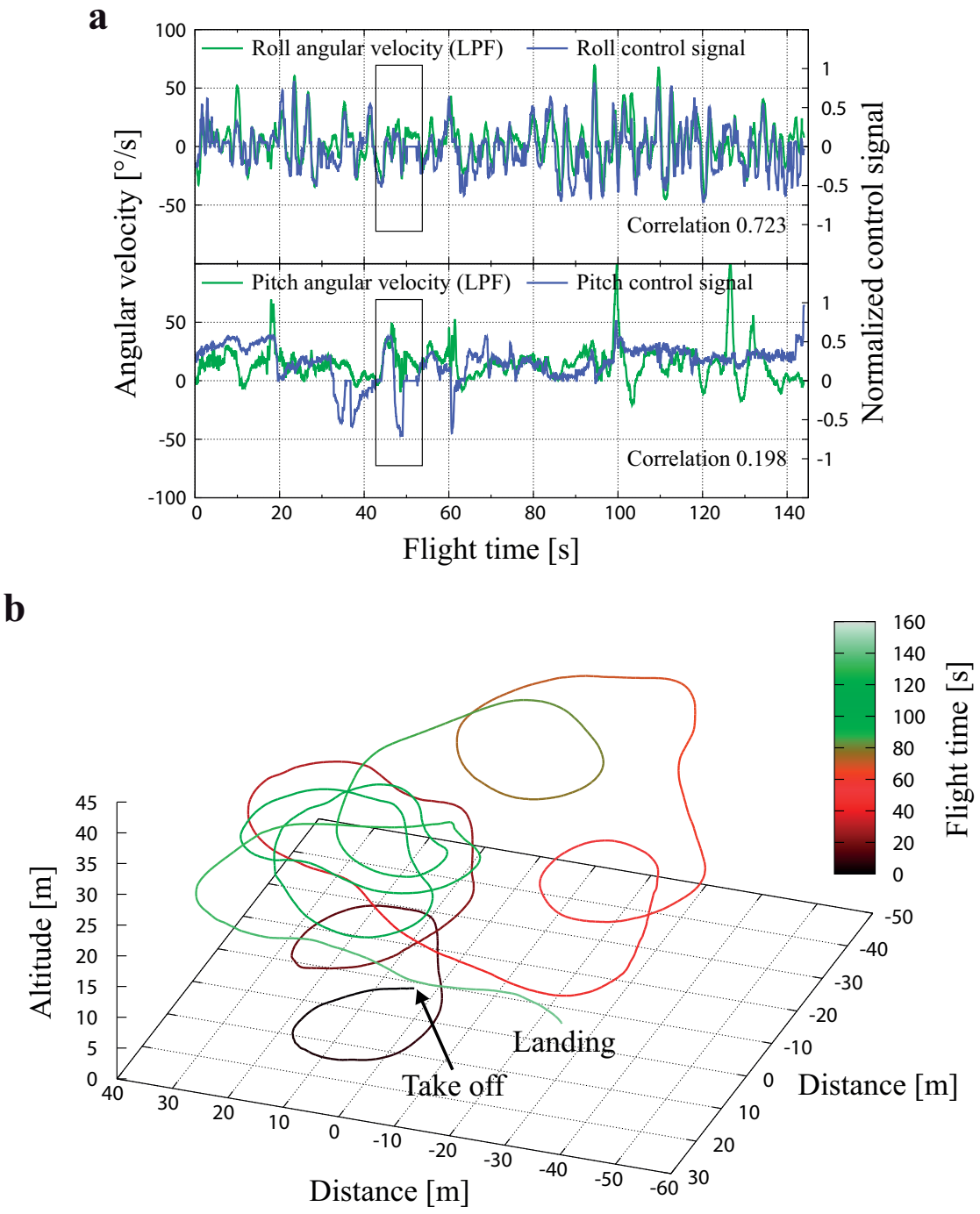

Figure 4.10 – (a) Comparison of the angular velocity and the control signal at flight time. During the flight, the attitude control is achieved only by the elevon actuators. The actuators controlled the MAV in the desired direction which is obvious from the fact that the angular velocity visibly follows the control signal. The trajectory shown in (b) is the result where the control signal therefore the will of the pilot is reflected. The trajectory is formed into a range where the MAV could be visually controlled.

Figure 4.11 – Turning sequence of the MAV during a flight. The MAV smoothly transition to a left tern, while the actuators well control the attitude. It is highlighted at the time section 2.5-3.5 s where the MAV is rapidly stabilized from a steep bank. Note that the time frame is different from that of Figure 4.10.

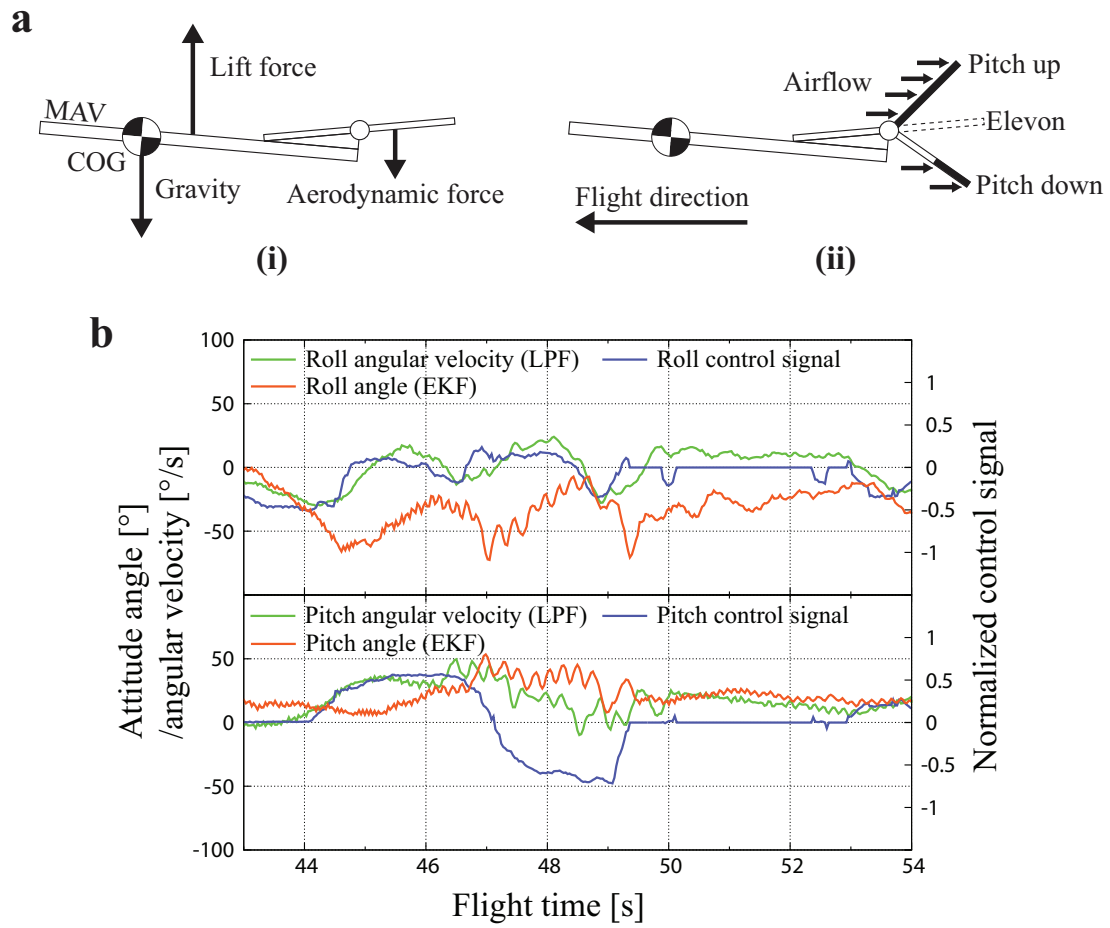

Figure 4.12 – Schematics of the longitudinal stability, and comparison of the attitude angle, the angular velocity, and the control signal at the flight time section of 43-54 s. (a)(i) The longitudinal stability is achieved by the moments around the COG caused by the lift force and the aerodynamic force on the elevon, which are stabilizing the MAV attitude on the pitch axis. (ii) Due to the biased actuator mounting angle, the surface area of the elevon exposed to the airflow is smaller at the direction of the pitch down, resulting in low controllability in this direction. (b) Comparison of the attitude angle, the angular velocity, and the control signal at the flight time section of 43-54 s.

Figure 4.12(b) shows the MAV attitude angle, the angular velocity, and the control signal at the flight time section of 43-54 s represented as a box in Figure 4.10(a). The attitude angle is determined using the extended Kalman filter. The attitude angles follow the control signal with a delay which may have resulted from the inertia of the MAV. The inherent stability is visible at 50-52 s where the attitude angles gradually decrease with no control signal towards their level flight attitude: 0 ° for the roll, and an angle of attack for the pitch, respectively. Both the roll and the pitch angular velocity show biases at 50-52 s. The bias on the roll is due to the inherent stability on this axis. The bias on the pitch angular velocity suggests that the MAV is turning while the attitude approaches to the level flight. As expected, the pitch angular velocity and hence the attitude is sensitive to the pitch up but not the pitch down.

4.7 Discussion

The flight of the MAV, which moves rapidly and requires accurate and fast control, proves that the positioning control and the response speed of the actuator perform adequately for this type of application. As the reason for this, mainly two actuator features are considered. First, the use of a silicone type elastomer as a DEA material, which has low viscoelasticity, contributes to both the positioning control and the response speed. Second, the simple actuator structure without additional mechanical parts prevents transmission loss. The simple structure also leads to ease of design.

In the model constructed in this work, the presence of many design parameters suggests the possibility of achieving a required performance with different combination of the parameters, allowing for flexibility of design. This is supported by the result shown in Figure 4.5 where the actuator performance directly changed with the number of DEA on each side. This flexibility could potentially be translated to scalability with proper dimensioning.

The symmetric configuration of the actuator in the motion plane suggests modularity. Considered from the fact that many robotic systems existing today consist of multi-degree-of-freedom-systems, it would be possible to realize those motions while holding the actuator features, that is, foldability and compliance. Also, as shown in the elevon actuator, an asymmetric planar geometry can be used for the arm part. This shows potential for the construction of complicated geometry forming systems where advanced robotic functionalities are realized, such as programmable shape change.

The compliance of the actuator gives robustness not only to the system but also to external environments. This would provide, for example, safe robot-human interactions and handling of fragile objects. As previously mentioned, the compliance can also be used as elastic strain energy storage, which enables self-deploying of robot structures without the need of actuation.

5 Variable Stiffness Dielectric Elastomer Actuator

This chapter develops an actuator with integrated variable stiffness functionality based on dielectric elastomers. The actuator, called variable stiffness dielectric elastomer actuator, consists of a uniaxially pre-stretched DEA bonded on a low-melting-point alloy (LMPA) embedded silicone substrate. In the actuator, the DEA generates a bending actuation, and the LMPA changes its phase between solid and liquid by Joule heating, providing variable stiffness of the structure between soft and rigid states. In order to prove the concept, an actuator with dimension of 40 mm length × 10 mm width × 1 mm thickness and mass of ~1 g is fabricated and characterized. The characterization results show voltage-controllable actuation stroke angle and blocked force up to 47.5 ° and 2.4 mN in the soft state, and 1.1 ° and 2.1 mN in the rigid state, respectively. The rigid state also exhibits a spring constant of 23.3 mN/mm, which is ~90× larger compared to an actuator without LMPA (0.26 mN/mm), representing the high stiffness. To demonstrate a practical use, a two-finger gripper is developed in which the actuators act as the fingers. The gripper, which has active parts mass of ~2 g, adapts the fingers to the object in the soft state, and exhibits a sufficient holding force in the rigid state, enabling picking up of an object mass of ~11 g (~108 mN), even though the actuated grasping force is only 2.4 mN.

5.1 Introduction

Soft robots are robots that consist of compliant materials. The approach to form those robots is known as soft robotics [254, 255, 256]. The passive adaptability of continuum structure of soft robots can perform terrestrial locomotion, bio-mimetic fish swimming, and gripping various objects with a simple feedforward control [326, 46, 260, 315], while conventional systems often require many actuators and sensors with sophisticated feedback control, and can be slow and costly. In addition, soft robots have shown resistance to mechanical and thermal damages [44, 257], and their inherent compliance ensures safety to interact with human [256].

Variable stiffness (controllable stiffness) can be an important function for soft robots to

This chapter is adapted from the article:
J. Shintake, B. Schubert, S. Rosset, H. Shea and D. Floreano, "Variable stiffness actuator for soft robotics using dielectric elastomer and low-melting-point alloy," in *IEEE/RSJ International Conference on Intelligent Robots and Systems*, Hamburg, Germany, October 2015.

exert intentional forces to environments, and to withstand external loads while keeping their shape. This function has enabled multi-task movement [258], adapted terrestrial locomotion [259], handling of various objects [260], and improved dexterity in manipulation [261]. Toward further development of these types of functional soft robots, one approach is to use variable stiffness actuators in which the actuation and the controllable stiffness are provided by a single device, thus drastically simplifying the robotic structure. Technologies related to this purpose in the literature are based on jamming [259, 260, 261, 262], electrorheological/magnetorheological fluids [263, 264], shape memory polymers (SMPs) [265, 266, 267], and low-melting-point alloys (LMPAs) [258, 268]. There have been variable stiffness actuators based on combinations of these technologies: jamming-pneumatic actuator [262], SMP-pneumatic actuator [267], and SMP-DEA [266].

However, these examples use external parts to provide air pressure, electromagnetic field, and temperature, respectively, which could lead to a complicated structure. Shape memory alloy could be a candidate as it is able to change its stiffness by Joule-heating directly, but it exhibits a small relative stiffness change (2-3×) and a high absolute stiffness (28-41 GPa elastic modulus in martensite phase) [6].

The aim of the work in this chapter is to develop a simple variable stiffness actuator composed of a DEA and a LMPA embedded silicone substrate [269]. The actuator does not require any external parts to control the stiffness as the LMPA substrate allows direct Joule-heating. Specifically speaking, (1) combining DEAs and LMPAs, and (2) an actuator configuration based on DEA that allows integration of LMPAs are proposed. Therefore, the actuator presented in this chapter leverages on a LMPA technology previously developed. In the following sections, first the LMPA substrate and the concept of the variable stiffness actuator is explained. To prove the concept, the actuator is fabricated and characterized. Subsequently, a two-finger gripper is developed to demonstrate a practical use of the actuator. Finally, the results obtained in this chapter are discussed.

5.2 LMPA Embedded Silicone Substrate

The LMPA embedded silicone substrate is made of a LMPA channel encapsulated in a silicone matrix where the LMPA changes its phase between solid and liquid by direct Joule-heating. Therefore, varying degrees of stiffness of the structure, between fully rigid and completely soft, are achieved efficiently as a function of the input power. The substrate shows a relative stiffness change of $> 25\times$ (elastic modulus of 40 MPa in the rigid state, and 1.5 MPa in the soft state), and a fast transition from rigid to soft states (< 1 s) at a low power (< 0.5 W) [269]. The transition speed, power consumption, and both the absolute and the relative stiffness depend on the geometry of the LMPA channel and the silicone matrix. The LMPA substrate can also act as a strain sensor by measuring its change in resistance due to changes in geometry [269]. The self-sensing capability could be used for more accurate actuator control or shape estimation, compared to the case where only the DEA is used for the sensing.

5.3 Working Mechanism

The actuator, called variable stiffness dielectric elastomer actuator (VSDEA), consists of a uniaxially pre-stretched DEA bonded on a LMPA embedded silicone substrate, as shown in Figure 5.1(a).

The working mechanism of the actuator is explained using Figure 5.1(b)(i-v). Even though the LMPA substrate can vary the stiffness as a function of the input power [269], in the rest of this chapter, only the two extreme cases are considered for the LMPA: solid and liquid, corresponding to soft and rigid state of the actuator. When the LMPA is activated, Joule-heating changes the phase of the alloy from solid to liquid, resulting in a soft state. In this state, (i) the entire structure is bent with a radius of curvature where the internal stress of the pre-stretched DEA and the bending moment of the LMPA substrate are at their equilibrium state. (ii) Applying a voltage to the DEA while keeping the LMPA soft leads to a unidirectional bending actuation towards the flat state, due to the electrostatic pressure which reduces the internal stress in the DEA and releases the bending moment in the substrate. The amount of the bending can be controlled by the voltage on the DEA. (iii) If the LMPA is deactivated but the DEA is kept active until the structure becomes solid, (iv) a rigid state for a desired bending (or flat) shape can be achieved. In this state, the device can sustain its rigid shape without any input power. From this state, other rigid shapes, e.g., (v), can be achieved by activating the LMPA through the state (i). Rigid states (iv) and (v) mean the device is able to rigidify all the shapes that are achievable in the soft state.

The DEA and the LMPA substrate can be made with silicone, and this inherent material compatibility simplifies the structure therefore eases the fabrication process and modeling of VSDEA. A closed-form analytical model of the actuator is described in Appendix A. For the same reason, the actuator has a high compliance in the soft state (elastic modulus of less than 1 MPa). In addition, the actuation of the VSDEA can be extended to bidirectional movement when another DEA is placed on the other side of the LMPA substrate, as shown in Figure 5.1(c). In this configuration, the DEAs start actuation from fully pre-stretched state, meaning that the actuation strain is beyond the pre-strain. Therefore, the performance of the actuator such as actuation stroke and output force will be different from that of the unidirectional configuration (Figure 5.1(b)).

The basis of the actuator concept, the configuration consisted of a pre-stretched DEA and a silicone substrate forming entirely soft actuator, is firstly presented by the author in [270]. Since then, there has been same configuration reported [271]. This configuration is similar to the dielectric elastomer minimum energy structures (DEMESs) that use a flexible substrate with a hole [154, 272]. DEMESs are also able to achieve bidirectional actuation [273]. However, our configuration has several features that differ from DEMESs. (1) The high compliance of the structure provides better physical adaptability to environments (e.g., conformation of gripper fingers to the object being held). (2) The absence of a hole eases the fabrication and the designing (e.g., layout of the LMPA channel), and improves the robustness as the DEA is covered by the substrate. (3) The use of silicone allows encapsulation of the LMPA into the substrate. (4) Bidirectional movement can be achieved with simpler structural configuration, just adding another DEA, contrary to DEMESs that require additional parts [273].

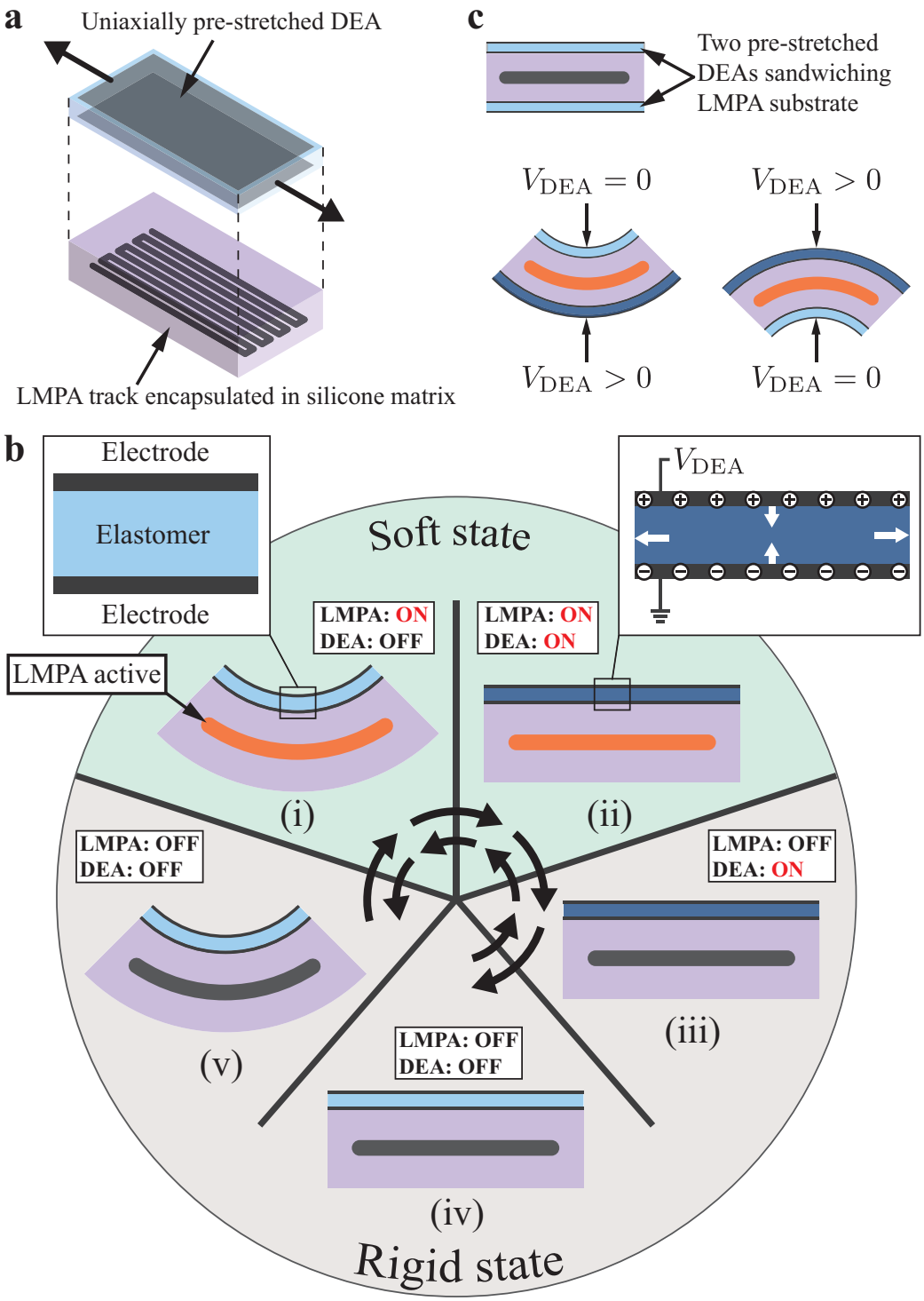

Figure 5.1 – Working mechanism of VSDEA. (a) The actuator consists of a pre-stretched DEA attached onto a LMPA substrate. (b)(i) The activation of the LMPA makes the structure soft, resulting in a bending shape. (ii) In this state, applying a voltage to the DEA leads to a bending actuation toward the flat shape. (iii)(iv) Deactivation of the LMPA keeps a desired bending shape. (v) Re-activation of the LMPA through state (i) allows changing of the rigid shape. (c) Bidirectional actuation can be obtained by putting another DEA on the other side of the LMPA substrate.

5.4 Fabrication

A proof of concept actuator is fabricated according to the fabrication process shown in Figure 5.2(a)-(j). The DEA and the LMPA substrate are made separately at first, and then they are bonded together at the end of the process. A silicone elastomer (NuSil Technology, CF19-2186) is used for the DEA. (a) The elastomer is cast on a polyimide sheet using a film coater (Zehntner, ZAA2300) and a film applicator (Zehntner, ZUA2000) forming a membrane with thickness of ~45 μm after the curing at temperature of 80 C°. (b) The membrane is then pealed-off from the sheet, stretched uniaxially, and held in an acrylic (PMMA) frame. (c) Subsequently, the compliant electrodes are applied on the both sides using the pad-printing.

The fabrication of the LMPA substrate starts from (d) printing Polylactide (PLA) with the geometry of the LMPA channel on the bottom plate of a PMMA mold using a 3D printer (MakerBot, Replicator 2). (e) The mold is then filled with a silicone (Smooth-On, Ecoflex 0030). (f) After the curing, the Ecoflex negative mold is placed on a stainless steel plate and the hot liquid LMPA is filled inside using a syringe through a punched hole. The LMPA used has a melting temperature of 47 C° (HiTech Alloys, Cerrolow 117). Once cooled, the molded LMPA is carefully separated from the Ecoflex negative mold. Then, the LMPA is annealed above the melting temperature to achieve a more favorable low-energy shape, as opposed to the forced shape of the mold. This step minimizes separation of the alloy in the final device due to poor wetting to the silicone encapsulation. During this step, the temperature of the steel plate is controlled using a hot plate. (g) To encapsulate the LMPA, a soft silicone (Bluestar, Silbione LSR 4305) in the liquid state is put in a PMMA mold. The amount of the silicone determines the position of the LMPA in the substrate in the thickness direction. (h) Before the filled silicone is cured completely, the molded LMPA is placed on the top, and the same silicone was filled again. The adhesion of the non-fully cured silicone prevents the movement of the LMPA until the entire structure is cured.

(i) After the curing of the silicone at room temperature, the LMPA substrate is carefully separated from the mold, and bonded to the DEA prepared at (c), using oxygen plasma surface activation (Diener electronic, Zepto plasma system). The DEA is equipped with the electrical connections using a conductive tape and a conductive silver epoxy. (j) The entire structure is cut from the PMMA frame and the electrical connections for the LMPA are formed using electrical wire. A silicone glue (Dow Corning, Sylgard 734) is put on the electrical connections to hold the connections and to prevent the leakage of the LMPA when it is in the liquid phase.

The fabricated VSDEA is shown in Figure 5.3(a). The actuator is flat after the fabrication, and the activation of the LMPA substrate leads to a bending shape due to the pre-stretch of the DEA. When compared to an actuator without the LMPA, the rigidity is visible where a nut of mass 2 g is supported (Figure 5.3(b)). On the other hand, the device can be compliant when the LMPA substrate is activated (Figure 5.3(c)). The heating time necessary to melt the LMPA is ~30 s at a power input of ~1 W for the fabricated actuator. The heating time can be shorten by increasing the input power. On the other hand, even the time to cool back the LMPA below melting takes ~30 s, more than ~60 s is necessary to cool the actuator back to room temperature. This is due to the fact that the cooling depends on convection between the surface of the LMPA substrate and the surrounding air [269].

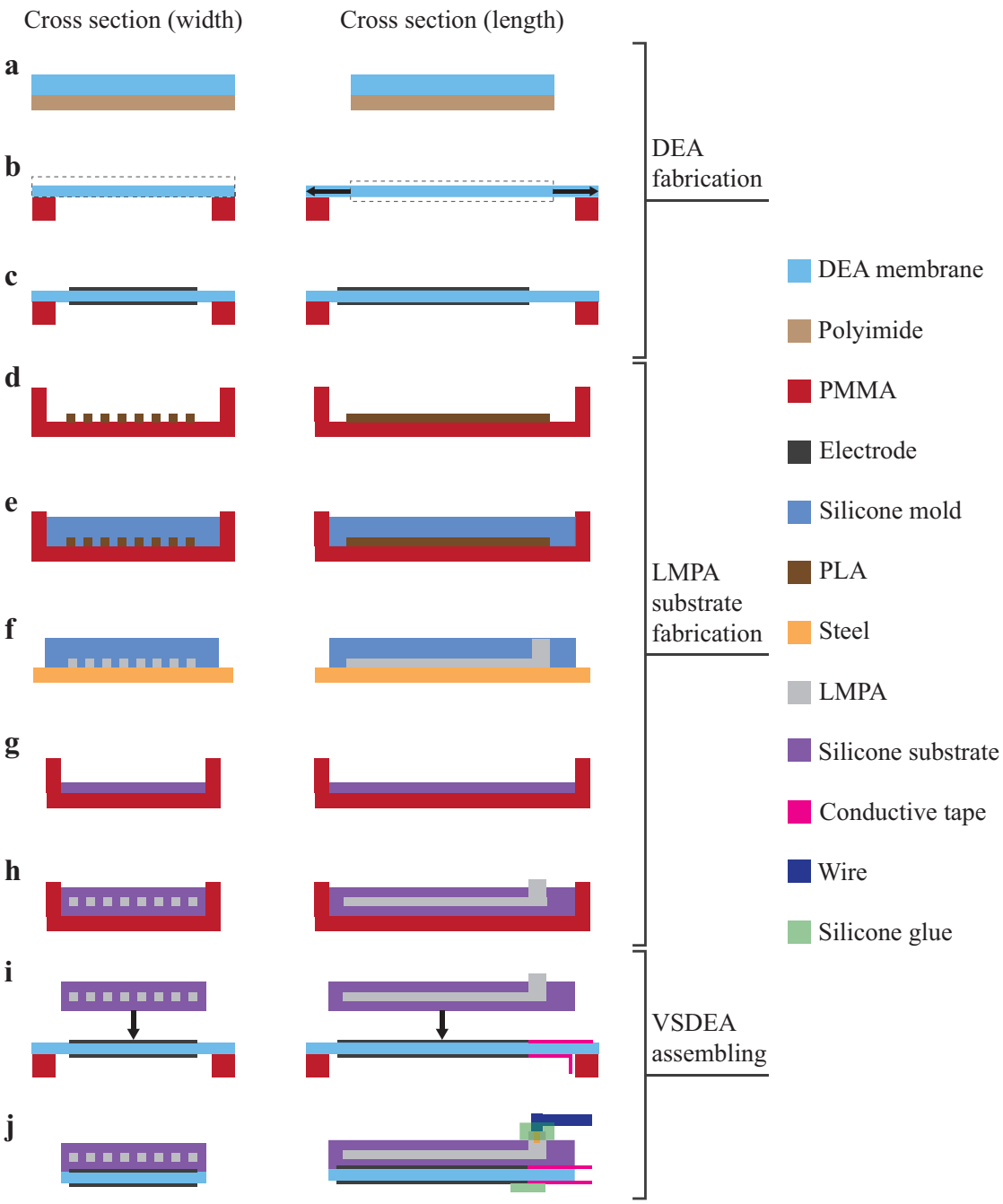

Figure 5.2 – Fabrication process of VSDEA. (a) The DEA elastomer is cast and (b) pre-stretched followed by (c) the patterning of the electrodes. (d) PLA is printed onto a PMMA mold to form the geometry of the LMPA channel. (e) Fill the mold with Ecoflex. (f) Hot liquid LMPA is filled inside the Ecoflex negative mold. (g) A soft silicone in the liquid state is put in a PMMA mold to encapsulate the LMPA. (h) Place the LMPA and fill the same silicone. (i) After the curing, bond the LMPA substrate to the DEA. (j) Place wires and then silicone glue over the connections.

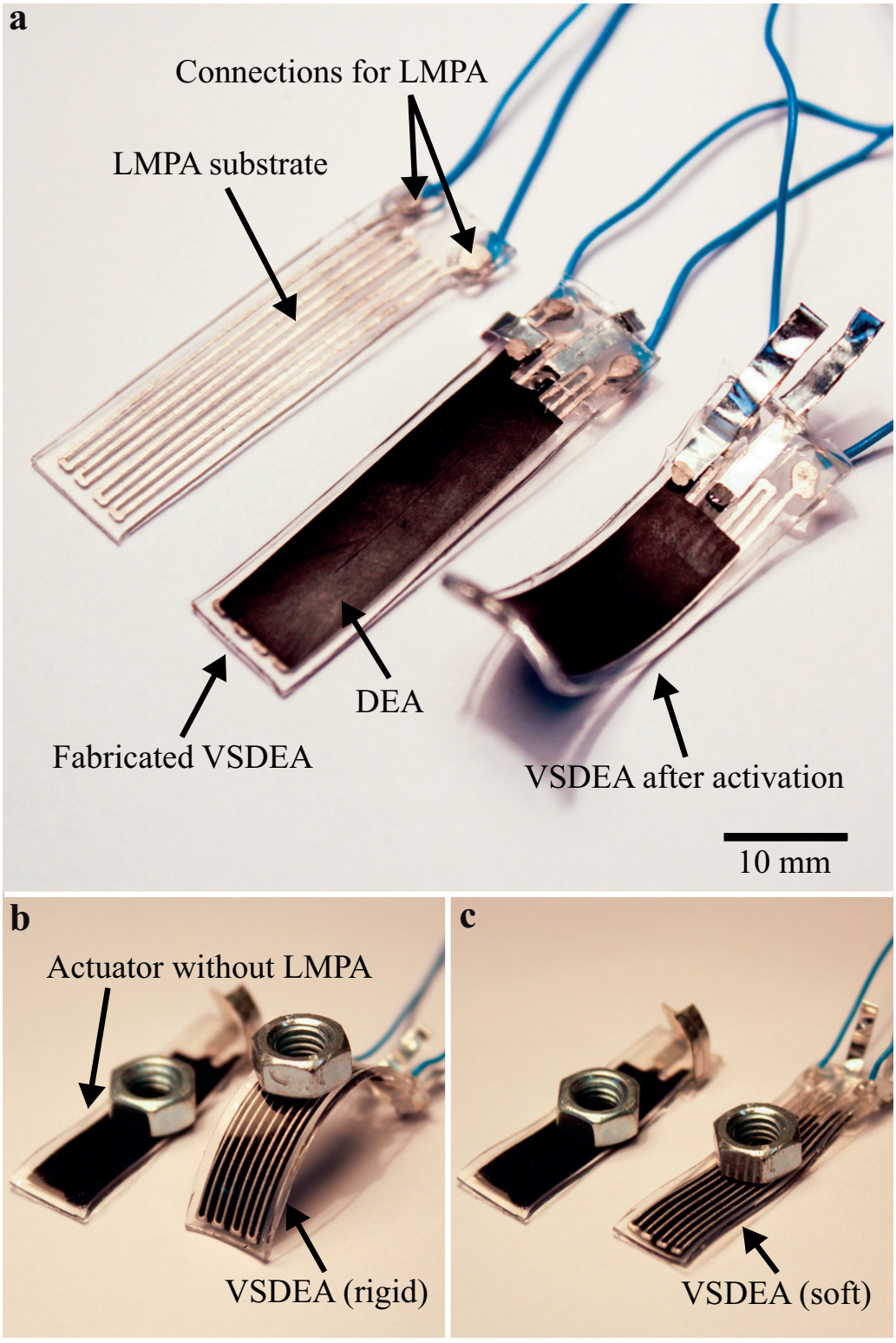

Figure 5.3 – Fabricated VSDEA. The actuation has an overall dimension of 40 mm length × 10 mm width × 1 mm thickness. (a) The activation of the LMPA substrate results in a bending shape. (b) Compared to an actuator without the LMPA, the rigidity of VSDEA is visible. (c) The compliance of the device is clear when the LMPA substrate is activated.

5.5 Actuator Design

The fabricated VSDEA shown in Figure 5.3(a) has a dimension of 40 mm length × 10 mm width × 1 mm thickness with mass of ~1 g. Table 5.1 summarizes the specifications. The DEA has an active electrode area of 29 mm length × 8 mm width. This area is determined so that it fits in the diameter of a printing pad used in the fabrication (46 mm). The DEA electrodes are surrounded with passive membrane region of 1 mm gap at their edge for insulation. The initial thickness of the DEA (~45 μm) is given so that the electric field inside the elastomer is below the breakdown field (100 V/μm for a silicone elastomer [92]) for a given maximum applied voltage (3 kV). When the actuator is flat, the DEA is thinnest therefore the electric field is strongest. In this state, the strain of the DEA equals the pre-stretch. The maximum electric field in the fabricated VSDEA is calculated as 80 V/μm (= 3000 V/(45 μm/1.2)). The pre-stretch ratio (1.2) is determined from an analytical model of an actuator with a pure silicone substrate (i.e., without LMPA). Appendix A details the model.

The cross-sectional geometry of the LMPA channel (0.45 mm width × 0.35 mm thickness) corresponds to a single line of the 3D printer used in the fabrication. The lateral dimensions of the channel (35 mm length × 8 mm width) is determined so that it covers the active electrode area of the DEA with equally-spaced lines. The LMPA channel is longer than that of the DEA to avoid overlapping of the electrical connections. The thickness of the entire substrate (1 mm) is the same as that of the preliminary experimental actuator mentioned above.

The pad diameter does not limit the electrode area because the DEA membrane can be moved laterally relative to the pad position. An example can be seen in [274], where an electrode geometry longer than the pad diameter is patterned to achieve a multi-segmented bending actuator. The LMPA channel cross-sectional dimensions and the spacing can be smaller when microfabrication process is used (42 μm width × 54 μm thickness, and 116 μm spacing are reported [269]). In this case, lateral dimension of the channel is limited to the size of a wafer. The entire thickness of the LMPA substrate (1 mm) can be changed corresponding to the amount of the liquid silicone used in the fabrication process steps (g) and (h) in Section 5.4.

As mentioned previously in Section 5.3, in terms of the configuration, VSDEA is similar to DEMESs. Therefore, the design principle to determine the behavior of VSDEA such as initial bending angle and actuation stroke and force could follow that of DEMESs. Mechanical parameters and material properties are associated to the design, and are mainly the geometry (lateral dimensions and thickness), the elastic modulus of both the DEA and the LMPA substrate, and the pre-stretch ratio. An optimal set of those parameters could be found based on analytical model [272, 89] or finite element method [157] that are available for DEMESs. In VSDEA, determination of the bending stiffness of the LMPA substrate in the soft and the rigid states is an important design aspect. The bending stiffness in the rigid state can be calculated by the integration of the second area moment of both the LMPA channel and the silicone matrix ([269], Appendix A). In the soft state, the LMPA channel is liquid. It has been proposed to approximate the liquid LMPA channel by the silicone matrix for calculating the bending stiffness [269]. However, this approximation may be not valid for VSDEA at the scale size of the fabricated actuator, as suggested in Appendix A. Therefore, it is necessary to reflect mechanical behavior of the liquid LMPA channel correctly in the design principle.

Table 5.1 – Specifications of the fabricated VSDEA

Specifications	Value
Dimensions*	
DEA	
Length	40 mm
Width	10 mm
Initial thickness	45 μm
DEA electrode	
Length	29 mm
Width	8 mm
LMPA channel	
Length	35 mm
Width (single channel)	0.45 mm
Overall width	8 mm
Thickness	0.35 mm
Number of channels	8
LMPA substrate	
Length	40 mm
Width	10 mm
Thickness	1 mm
Material property	
DEA elastomer (NuSil Technology, CF19-2186)	
Elastic modulus	0.83 MPa [126]
LMPA (HiTech Alloys, Cerrolow 117)	
Elastic modulus	3.0 GPa [269]
Substrate silicone (Bluestar, Silbione LSR 4305)	
Elastic modulus	0.2 MPa [126]
Other	
DEA pre-stretch ratio	1.2
Mass	~1 g

* Values are of the flat state.

5.6 Characterization

5.6.1 Experimental Setup

The fabricated actuator is characterized on the actuation stroke angle, the blocked force, and the reaction force against a forced displacement. Figure 5.4(a) inset shows a bending actuation of the VSDEA in the soft state. The actuation stroke angle measured is defined as the tip angle difference from the initial shape i.e., no applied voltage. The actuator is placed in the direction minimizing gravity effects. A CMOS camera and image processing with MATLAB are used to obtain the angle value. The blocked force and the reaction force are taken by putting the probe of a load cell (Applied Measurement, UF1-55) to the actuator tip perpendicularly at the initial shape (Figure 5.4(b) inset). The reaction force is measured by applying the forced displacement via the load cell probe which is moved externally using a motorized stage (Zaber T-LSR150B), as shown in Figure 5.5 inset. During the characterization, the power input for activating the LMPA substrate is kept at ~0.5 W, while the applied voltage for the DEA is varied from 0 to 3 kV. A power supply and a high voltage supply (Auckland Biomimetics Lab, EAP controller) are used for activating the LMPA and the DEA, respectively.

5.6.2 Results

The measured bending angle as a function of the DEA applied voltage for the soft and the rigid state is shown in Figure 5.4(a). 6 samples are measured and the average is taken. At the soft state, the actuator showed voltage-controllable actuation with the angle range of 47.5 ± 7.2 ° at 3 kV. On the other hand, the rigid state exhibited almost same shape over the DEA applied voltage, only 1.1 ± 0.8 ° angle difference is observed at 3 kV, representing the high bending stiffness of the structure. The deviation of the data is due to different initial angle of the samples resulting from the fabrication variation.

Figure 5.4(b) plots the measured blocked force as a function of the DEA applied voltage for the rigid and the soft state. Same as the angle, 6 samples are measured and the average is taken. Both the states showed similar force at 3 kV (2.4 ± 0.2 mN for the soft state, and 2.1 ± 0.5 mN for the rigid state). The larger deviation at the rigid state may have resulted from the alignment errors of the load cell probe and the small actuation angle of the actuator preventing accurate measurement. Figure 5.4(c,d) shows the bending angle and the blocked force as functions of the DEA applied voltage for one actuator with 5 cycle measurements. The actuator exhibited good repeatability, only a small hysteresis is observed, and this is due to low viscoelasticity of the silicones used for the actuator.

Figure 5.5 shows the measured reaction force as a function of the forced displacement. In this measurement, a VSDEA and an actuator without LMPA are used. To clarify their rigidity difference, the spring constant of the devices k is estimated using a least squares method applied to the data on the range of 1-3 mm (linear part). The spring constant k_v is defined as $k_\mathrm{v} = F_\mathrm{r}/x_\mathrm{d}$, where F_r and x_d are the reaction force and the forced displacement, respectively. The fitted lines based on the calculation are shown in Figure 5.5. The spring constant of the VSDEA is obtained as 23.3 mN/mm, and is ~90 times larger than that of the actuator without the LMPA (0.26 mN/mm).

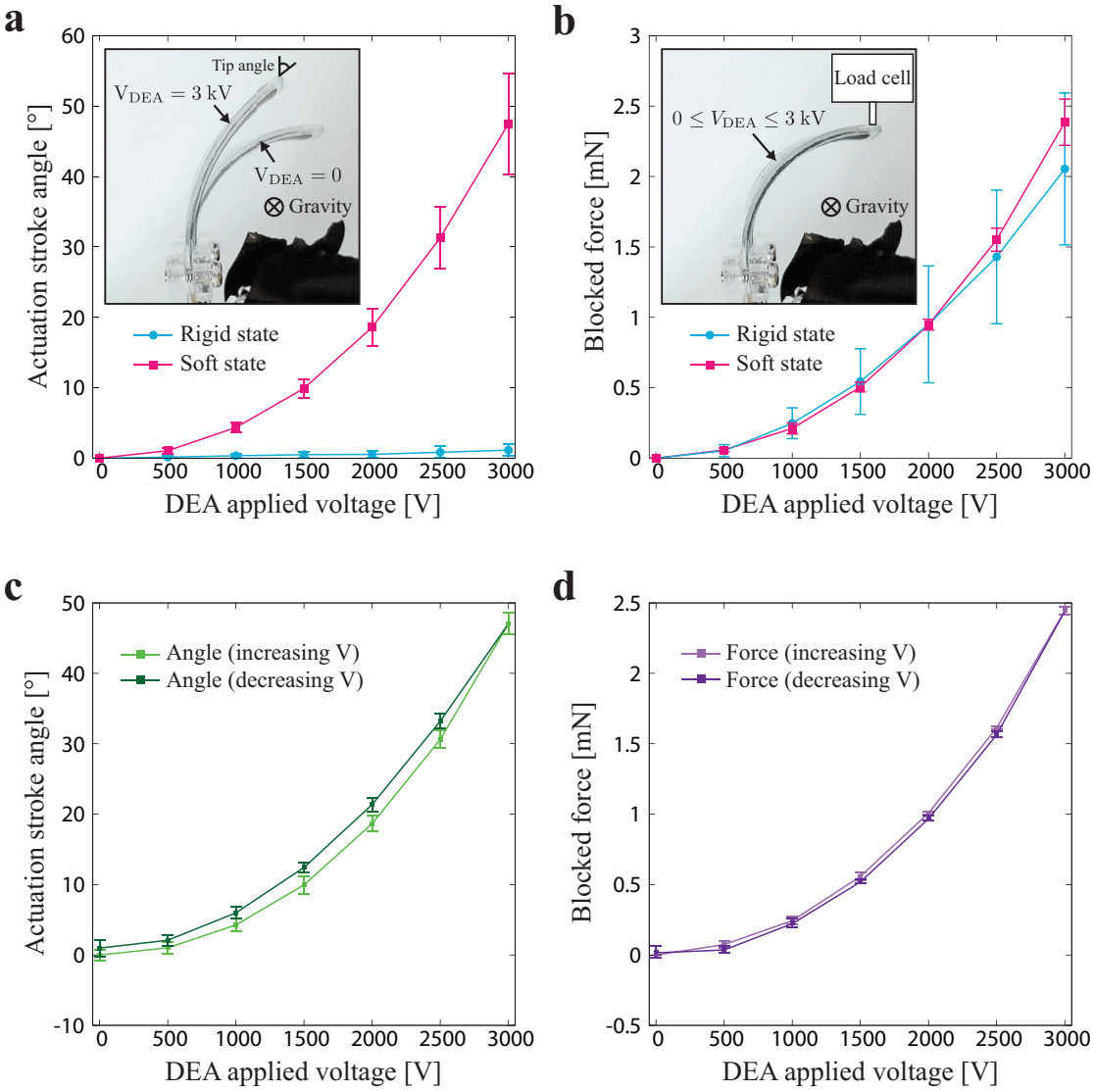

Figure 5.4 – Measured actuation stroke and blocked force as function of the DEA applied voltage, and the reaction force against a forced the forced displacement. (a) Measured actuation stroke angle as a function of the DEA applied voltage. Inset shows actuation of a VSDEA in the soft state. The actuation stroke angle is measured as the tip angle difference from the initial shape. In the soft state, the power input for the LMPA is kept ~0.5W. The actuation range is observed as 47.5 ± 7.2 ° for the soft state, and 1.1 ± 0.8 ° for the rigid state at 3 kV. (b) Measured blocked force as a function of the DEA applied voltage. The blocked force is measured by putting the load cell probe on the tip of the actuator. Similar force was observed for both states: 2.4 ± 0.2 mN for the soft state, and 2.1 ± 0.5 mN for the rigid state. 6 samples are measured in both the stroke angle and the force characterizations, and their average is reported. (c) Result of 5 cycle measurements of one sample on the actuation stroke angle and (d) the blocked force. The actuator showed good repeatability.

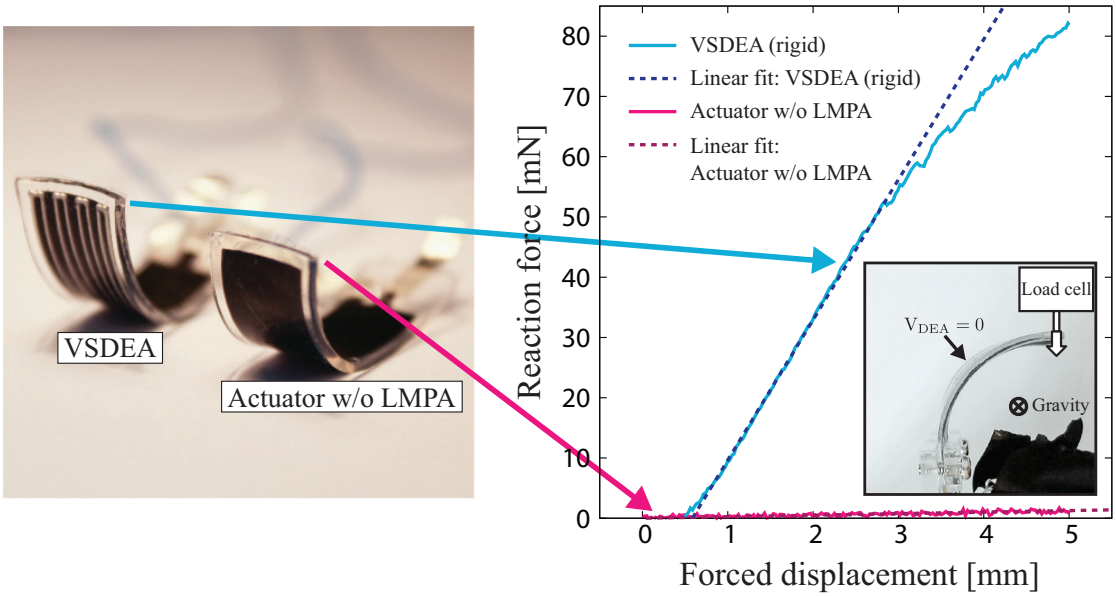

Figure 5.5 – Measured reaction force as a function of the forced displacement. The rigidity of the VSDEA led to a clear difference compared to an actuator without the LMPA. The dashed lines represent the spring constant of the devices obtained by a least squares method.

5.7 Two-finger Gripper

A two-finger gripper shown in Figure 5.6 is developed as an application to demonstrate a practical use of the actuator. The gripper consists of two VSDEAs connected via plastic parts to act as the fingers. Each finger is the same actuator characterized in the previous section, therefore, the mass of the active parts of the gripper is ~2 g. For this type of grasping devices, VSDEA is expected to provide adaptation of the fingers to the object in the soft state, and a sufficient holding force at the rigid state. An external motorized stage (Zaber, T-LSR150B) provides up-down motion of the gripper to perform picking up of the object, while a high voltage supply (Auckland Biomimetics Lab, EAP controller) activates the gripper fingers.

Figure 5.6(a)-(i) show the sequences of a gripper demonstration. To visualize the effect of the stiffness change, firstly a picking up of the object rely on only the soft state is shown in the sequences (a)-(f). (a) At the beginning, the gripper is above the object, a plastic dish filled with metal washers of mass ~11 g (~108 mN). The fingers are at close position. Soften the fingers by activating the LMPA, and (b) applying a voltage to the DEA leads to their open position. (c) The gripper is lowered by the external motorized stage. (d) Cutting of the voltage to the DEA leads to closing the soft fingers to grasp the object with passive adaptation of their compliant structure. (e) Subsequently the gripper is raised to pick up the object while keeping the LMPA active. However, (f) the device eventually loses the object due to a low holding force resulted from the high compliance of the structure. Next, instead of operating the gripper only in the soft state, after the sequences (a)-(d), (g) solidifying the fingers by deactivating the LMPA. (h-i) The rigid state provides a sufficient holding force and picking up object is successfully achieved, even though the actuated grasping force is only 2.4 mN. The full procedure of the gripper demonstration described above can be seen on [275].

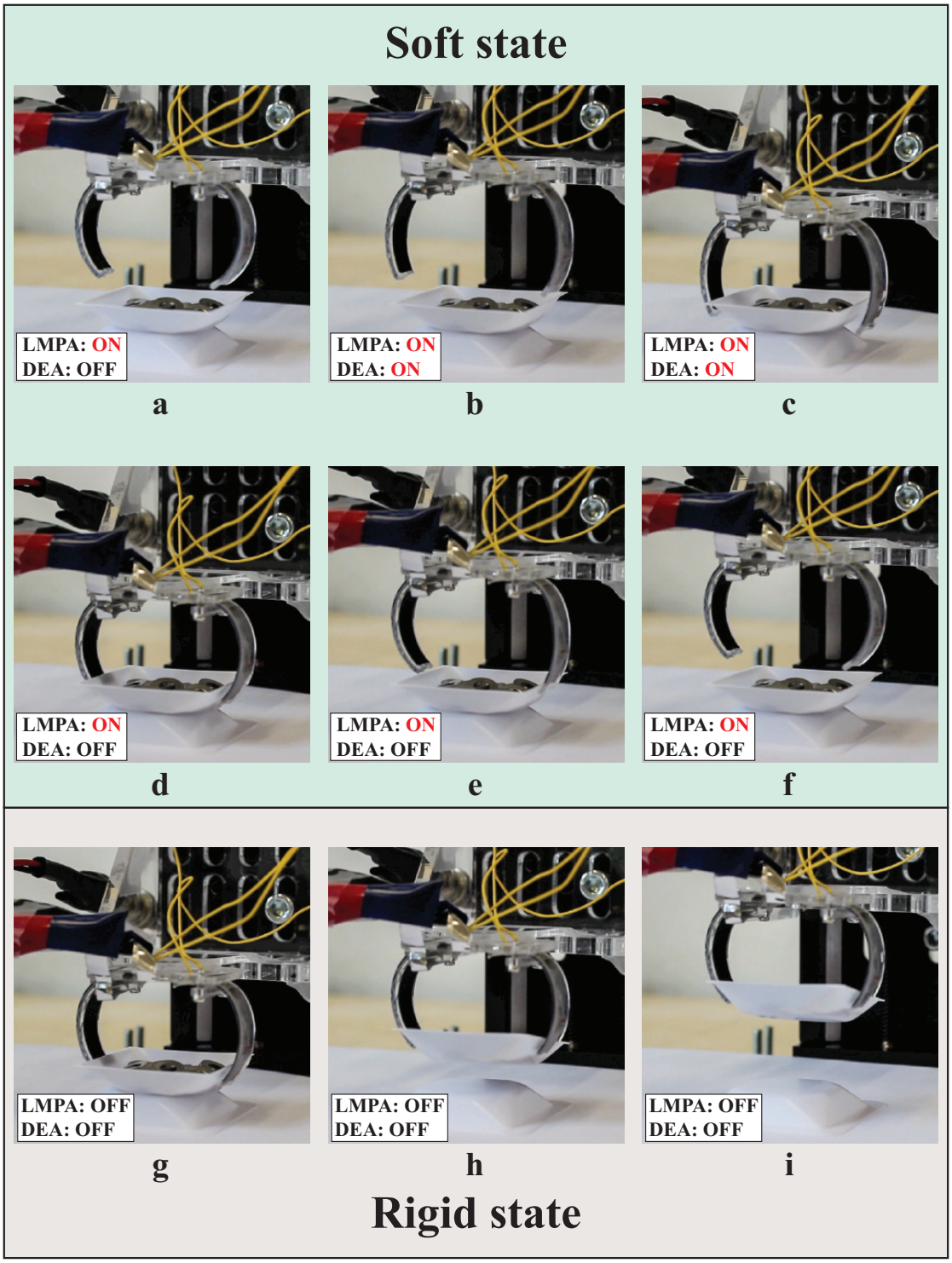

Figure 5.6 – Developed gripper consisting of two VSDEAs. An external motorized stage is used to provide up and down motion of the device to perform picking up of the object. The sequences (a)-(f) shows an attempt to pick up an object only rely on the soft state. The object, a plastic dish filled with metal washers of mass ~11 g, can not be picked up due to a low holding force resulted from the high compliance of the structure. When the rigid state is used after the sequences (a)-(d), the gripper is able to pick up the object thanks to a sufficient holding force.

5.8 Discussion

The simple actuator structure allows decoupling and designing of the actuation part and the variable stiffness part independently, leading to a high design flexibility. This may contribute production of the device at different geometry and scale. As a DEA configuration, the actuator could be combined with other variable stiffness materials or devices (e.g., SMP with a heater) by simply replacing the LMPA substrate.

The actuator finds potential applications. Since the device does not require any power input to sustain the rigid state, this feature could take a role of holding the package in small transportation drones [323] during flight, where the available power source is limited. For the same reason, perching of flying robots (e.g., [276]) could be considered. The controllable stiffness allows us to have variable mechanical impedance [238] which would enable various dynamic behaviors of the system e.g., asymmetric deformation of a periodically actuated structure could produce one way thrust like a jellyfish [277]. The current structure of VSDEA does not limit segmentation of the DEA and the LMPA. This means that even from a single device, multi-degree-of-freedom actuation could be generated. Such actuation may allow complex deformation strategies to perform programmable shape change. The segmentation of the LMPA may enable local stiffening of the robot, which could be used for dextrous manipulators (e.g., [261, 278]) and endoscopes (e.g., [279]). The self-sensing capability of both the DEA and the LMPA substrate in VSDEA would support controlling of those applications mentioned above.

6 Electroadhesion Dielectric Elastomer Actuator

This chapter develops an actuator with electroadhesion functionality based on dielectric elastomers. The actuator relies on a DEA design that simultaneously maximizes electroadhesion and electrostatic actuation, while allowing self-sensing by employing an interdigitated electrode geometry. The concept of the DEA design is validated through development of a two-finger soft gripper. The electroadhsion functionalizes the gripper to posses increased versatility. To address an optimal design for the gripper, experimental devices are characterized. The results show that the proposed DEA design generates much larger electroadhesion force (10×) homogeneously distributed on the electrode surface, compared to a conventional DEA design. The design also demonstrates high holding force of the gripper (3.5 N shear force for 1 cm^2) and low mechanical grasping force (1 mN) enabling handling of sensitive objects as well as other solid objects. The developed gripper is simple, lightweight (~1.5 g), and fast (~100 ms to close fingers). The gripper is found capable of handling a wide range of challenging objects such as a fragile, highly-deformable water-filled thin membrane balloon (35.6 g), a flat sheet of paper (0.8 g), and a raw chicken egg (60.9 g).

6.1 Introduction

The actuation of DEAs results from an electrostatic pressure (the Maxwell stress) generated by opposite charges on the electrodes. The Maxwell stress is proportional to the square of the electric field in the elastomer membrane in the direction normal to the surface [294](also shown in Section 3.1). For DEA actuation, one generally only considers this normal electric field in the elastomer. However the charges on the electrodes also create fringe electric fields at the edges of the electrodes. These fringe fields can generate electroadhesion in nearby objects, as the electric fields induce surface charges on the objects, resulting in attractive forces to the charges on the electrodes. In DEA applications, these forces are usually ignored and their use has not been reported to date.

The aim of the work in this chapter is to develop an electroadhesion enabled dielectric

This chapter is adapted from the articles:
J. Shintake, S. Rosset, B. Schubert, D. Floreano and H. Shea, "Versatile soft grippers with intrinsic electroadhesion based on multifunctional polymer actuators," *Advanced Materials*, accepted.
J. Shintake, S. Rosset, B. Schubert, D. Floreano and H. Shea, "DEA for soft robotics: 1-gram actuator picks up a 60-gram egg," in *Proc. SPIE*, San Diego, CA, USA, March 2015.

elastomer actuator. The idea is to have a DEA design that simultaneously optimizes both electroadhesion and electrostatic actuation of a bending DEA by an electrode arrangement, allowing both in-membrane and fringing electric fields to be maximized. The concept of the DEA design is validated through development of a two-finger soft gripper. In the soft gripper, the functionality of the actuator—electroadhsion—yields a high versatility on objects types that can deal with. In the following sections, first versatility in robotic grippers, and electroadhesion and other comparable adhesion technologies in terms of their usability for grasping devices are discussed. Subsequently, the DEA design is presented, and an optimal design is addressed for the gripper through characterization of experimental devices. After the characterization, the gripper is developed and evaluated through picking up demonstration for a set of varied objects. Finally, the results obtained in this chapter are discussed.

6.2 Versatility in Robotic Grippers

The human hand easily picks up objects of an enormous variety of shapes, even if they are fragile or highly deformable. In order to achieve this high versatility, fingered robotic grippers often use many actuators in combination with feedback control based on visual, tactile, force and angular position sensing, followed by trajectory planning [280, 281, 282]. If the target object is fragile, such as a chicken egg for example, the human hand adapts the grasping force, exploiting the compliance of tissue in the fingers and sensing the shear movement to safely grip the object [283]. Moreover, in the case of deformable objects such as a water balloon, human hands can sense the stiffness and follow the deformation while continuously regulating force and finger position.

Replicating these grasping properties with traditional robotic grippers typically require complex sensing, motor accuracy, modelling, and learning [284, 285, 286, 287, 288]. Endowing robotic grippers made with rigid components with the versatility to grasp objects with many different shapes and differing material properties can be computationally challenging, costly and slow, and require external sensors. For this reason, robotic grippers typically have a specialized design for a specific object type [289].

Soft grippers, grippers consist of compliant materials, suggest a path to simplifies control for handling complex objects, thanks to their inherent compliance allowing passive shape adaptation of the gripper structure to the object. Early investigation on shape-adaptable grippers exploited a variety of technologies such as air evacuation of granule-filled bag [290] (now known as granular jamming [260]), electrorheological (ER) fluids [291], ER fluid with electroadhesion [292], pneumatic actuators [293], and shape memory foams [293]. Yet even for current soft grippers [260, 315, 316, 300, 317, 318, 319], tasks that are easy for human hands, such as handling flat objects and deformable objects, remains a major challenge.

6.3 Electroadhesion and Other Adhesion Technologies

Electroadhesion has been used in wafer handling [295], wall climbing robots [296, 297], rigid and flexible grippers [298, 299]. Early development also showed an end effector composed of a rigid flat substrate and an ER fluid encapsulated membrane [292]. Electroadhesion has many advantages over comparable adhesion technologies, such as vacuum or gecko-inspired adhesion.

Vacuum handling technologies are widely used in industry, but are limited to objects with smooth, non-porous surfaces. Additionally, the need for vacuum pump and tubing adds significant bulk. Gecko-inspired adhesion uses van der Waals forces between passively deformed micro fibers and the target surface. This adhesion technology has been applied for grippers [300, 304, 305]. However, in this technology, the adhesion mechanism relies upon external mechanical preloading in the normal or shear direction [300, 301, 302, 303, 304, 305], which may cause unpredictable deformation and possible damage when the target object is sensitive like fragile or deformable. Reversibility of the gecko adhesion is also challenging to achieve with lightweight objects, and the adhesion mechanism works poorly on low surface-energy materials, such as Teflon [306].

Electroadhesion can be used with smooth and rough surfaces, with dielectric objects and with metallic objects [295, 298] and is fully electrically controlled. A potential drawback is a small residual adhesion force after removing the voltage. However, these residual forces are reported to be extremely low for dielectric objects, and last for only a few seconds [307]. For conductive objects the small residual force can be greatly reduced by operating at low frequency AC voltage rather than DC [295].

6.4 Working Mechanism

A schematic of the DEA design for the gripper is shown in Figure 6.1(a). The structure consists of an elastomer membrane with patterned compliant interdigitated electrodes laminated between two passive silicone layers. In order to maximize the electroadhesion force and the electrostatic actuation, the electrodes are wired such that adjacent electrode segments on the same planar surface are at opposite potentials, as are those electrodes which overlap each other across the membrane (Figure 6.1(b)). When a voltage bias is applied across the electrodes, fringe electric fields are generated at the segmentation boundaries providing homogeneous adhesion forces over the entire surface (Figure 6.1(b-c)), contrary to conventional DEA designs that can generate adhesion forces only at the periphery.

According to the literature, the adhesion force scales with the square of the fringe electric field intensity that induces surface charges by polarization for dielectric materials [309, 310], and by electrostatic induction for conductive materials [310]. The same applied voltage provides electrostatic actuation in the region where electrodes directly overlap. The passive silicone layers, sandwiching the DEA (Figure 6.1(a)), serve to insulate the electrodes to avoid electrical breakdown between adjacent electrodes or short-circuit via the external object. In the gripper, the bottom passive layer is in contact with the object being picked up. A stiffer elastomer, Sylgard 184 (~2.6 MPa of elastic modulus with curing temperature at 150 C° [308]) is used for the passive layers to minimize inherent tackiness, allowing smooth releasing of objects.

The actuator exhibits a bending actuation that can be used for the gripper fingers motion, by applying a voltage to a uniaxially pre-stretched DEA bonded to one or two passive layers (Figure 6.1(d)). This actuator configuration is same as the one presented in Section 5.3. The structure has a curled shape at zero applied voltage where the internal stress of the pre-stretched DEA and the bending moment of the passive layers are at their equilibrium state. When a voltage is applied, the electrostatic pressure reduces the internal stress in the DEA and releases the bending moment in the passive layers, leading to voltage-controllable bending actuation towards a flat shape. The initial bending angle, the actuation stroke, and the actuation force can be modulated by the mechanical parameters, such as, elastic modulus and thickness of both the DEA and the passive layers, and the DEA pre-stretch.

Our DEA design, having four independent electrodes, also allows different output characteristics by changing wiring of electrodes as shown in Figure 6.2: DEA actuation with reduced electroadhesion force, and only electroadhesion with no DEA actuation. Moreover, the larger percentage change in capacitance of the device as it uncurls enables self-sensing of the bending angle (Appendix B), as reported for other DEAs.

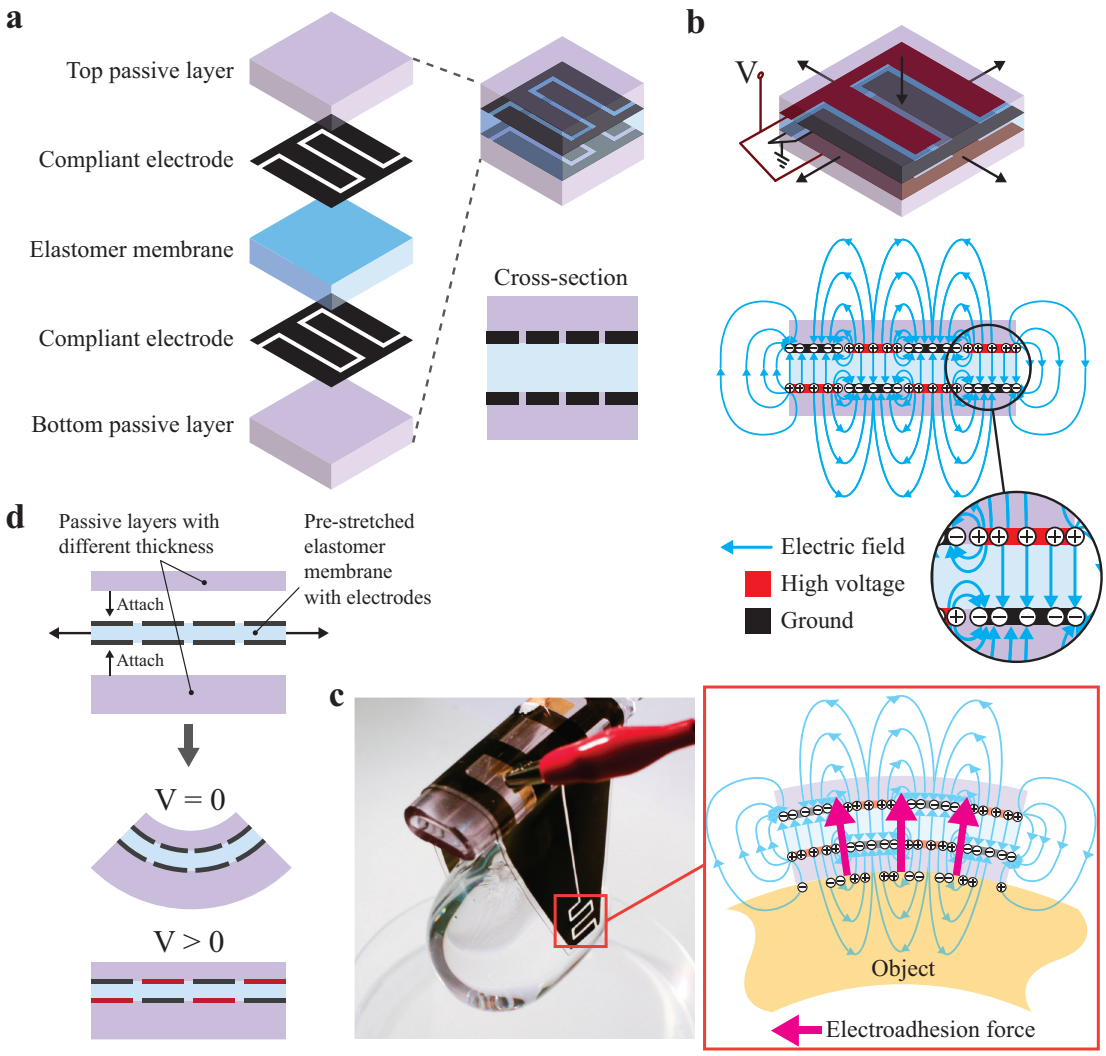

Figure 6.1 – Working mechanism of the DEA design for the gripper. (a) Each of the electrodes sandwiching the elastomer membrane consists of two interdigitated electrodes. Two passive layers made of a silicone are laminated on the top and bottom. The bottom passive layer touches the object being picked up. (b) DEA actuation (bending motion in this multilayer configuration) is proportional to the square of the electric field in the membrane in the direction normal to the surface, and the electroadhesion force is proportional to the square of the fringe electric fields. For optimum combined DEA and electroadhesion operation, one applies the same voltage difference between the neighboring interdigitated electrodes on the top and bottom layers, but laterally offset so as to obtain an alternating high electric field normal to the membrane (where top and bottom electrodes overlap), and strong fringe fields in the gaps at the segmentation boundaries. Other electrodes configurations lead to different actuation and gripping modes (Figure 6.2). (c) These fringe fields create electroadhesion forces on the object surface in contact, which are used to generate substantial holding forces in the gripper. The electroadhesion is maximum in the region where the electrodes are interdigitated, allowing tailoring which parts of the electroadhesion grip, and parts which only bend. (d) DEA gripper consists of a pre-stretched DEA bonded to passive layers. The structure is curled at zero applied voltage. Applying voltage to the DEA generates electrostatic pressure, which reduces the stress in the DEA, uncurling the structure towards a flat shape.

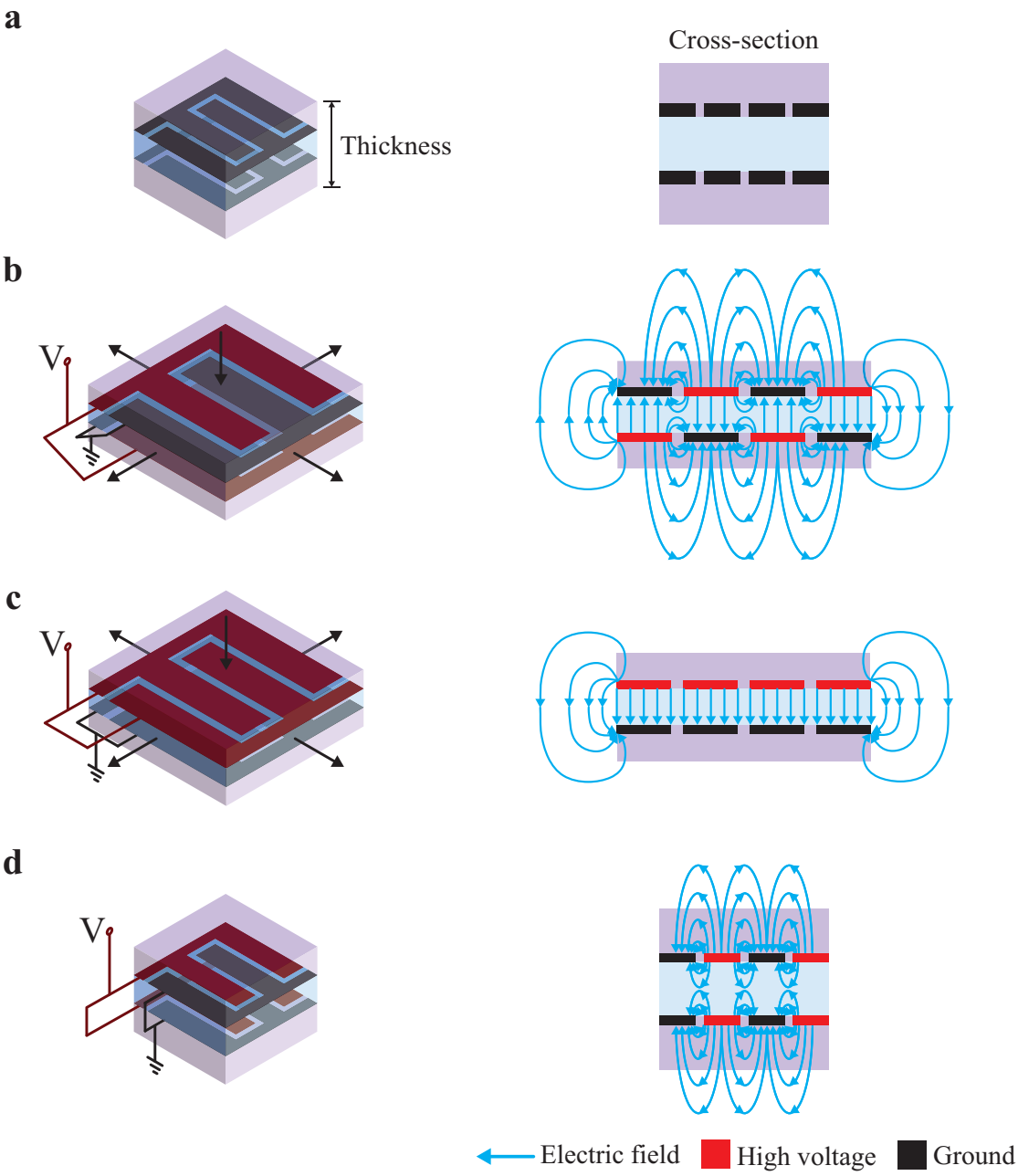

Figure 6.2 – Different output characteristics of the DEA design. (a) Initial state of the DEA (without any applied voltage). (b) Activation with the wiring used for the gripper configuration (described in the main text), which creates electrostatic actuation with higher electroadhesion force. (c) Activation with opposite potentials across the thickness direction like usual DEAs results in electrostatic actuation with fringe electric fields at the edges, generating actuation with reduced electroadhesion force. (d) Activation with opposite potentials on the same planar surface and same potentials in the thickness direction results in fringe electric fields on the surface, i.e., electroadhesion forces while no electrostatic actuation is produced.

6.5 Fabrication

In this section, the fabrication process used for the experimental devices and the gripper is explained. The devices and the gripper are later discussed in Section 6.6 and Section 6.7, respectively.

The fabrication process shown in Figure 6.3 starts from casting the DEA membrane. (a) The silicone NuSil Technology CF19-2186 consisted of two components is mixed with a solvent (iso-octane) at a 2:1 weight ratio, respectively, and the mixture is blade-casted on Polyethylene terephthalate (PET) film using a variable gap applicator (Zehntner, ZUA2000) and a film applicator coater (Zehntner, ZAA2300), then cured for 60 min at 80 °C. The thickness of the casted membrane depends on the applicator gap. DEA membranes of two thicknesses are used: 80 μm and 60 μm for the experimental devices and for the gripper, respectively. (b) The DEA membrane is peeled from the film, pre-stretched uniaxially with a ratio of 1.2, and mounted in a Polymethyl methacrylate (PMMA) holding frame using a silicone adhesive foil (Adhesives Research, ARclear 8932EE) for electrode patterning. Subsequently, the compliant electrodes are patterned using the pad-printing. The electrodes are cured for 30 min at 80 °C. (c) The passive layers are chemically bonded onto the DEA membrane, using oxygen plasma surface activation (Diener electronic, Zepto plasma system). The passive silicone layers (Dow Corning, Sylgard 184) are produced with the same blade casting process, and different curing temperatures are used: 80 °C and 150 °C for the experimental devices and the gripper, respectively. (d) Holes that penetrate the structure are made by punching for the electrical connections. (e) A PMMA plate is attached below the sample using the silicone adhesive foil. (f) The holes are filled with a silver epoxy (amepox, ELECTON 40AC), and pieces of a conductive tape are placed. (g) After the wiring, the device is separated from the holding frame. Figure 6.3(h)-(j) are the devices fabricated through the process above. They will be described in the following sections.

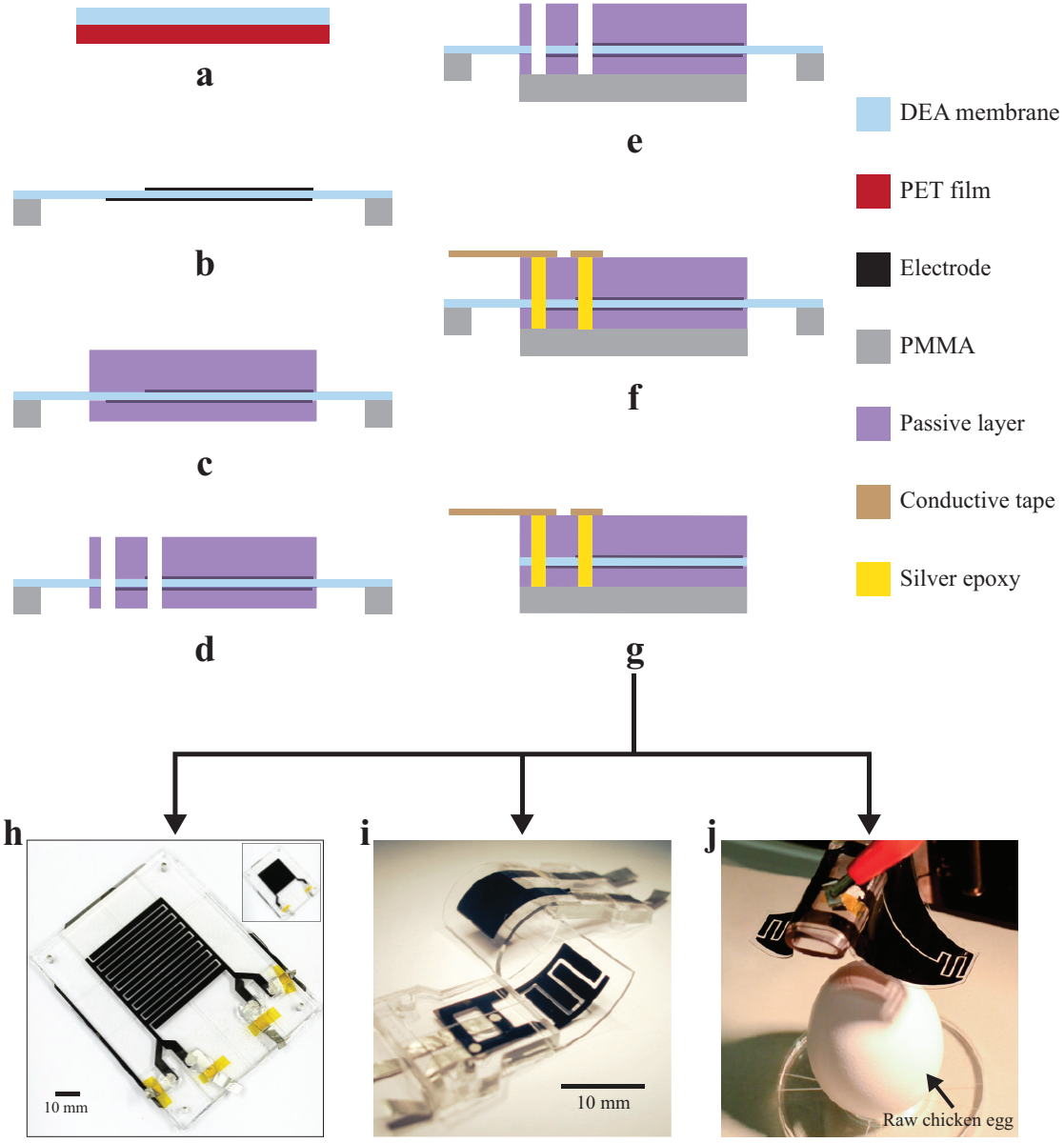

Figure 6.3 – Fabrication process of the experimental devices and the gripper. (a) The DEA membrane is blade-casted on a PET film. (b) The membrane is peeled from the film, pre-stretched uniaxially, and mounted in a PMMA holding frame. Subsequently the electrodes are patterned via a pad-printing. (c) The passive layers are chemically bonded on the DEA membrane. (d) Punched holes are made for the electrical connections. (e) A PMMA plate is attached below the sample. (f) The holes are filled with a silver epoxy, and pieces of a conductive tape are placed. (g) The device is separated from the holding frame. (h) Samples used for local adhesion force measurement. (i) Samples used for total adhesion force and actuation performance measurements. (j) Gripper used for validation of the DEA design.

6.6 Characterization

The interdigitated electrode geometry, used for the DEA design, has gaps between the segmented boundaries necessary for maximizing electroadhesion. The gaps however lead to a reduction of the electrostatic actuation due to the smaller overlapping electrode area across the DEA membrane. The gaps can be narrowed to maximize DEA actuation, but the gap size must be sufficiently large to avoid electrical breakdown in the passive layer insulating the segmented electrodes (of order 100 μm gaps are needed to withstand 5 kV potential difference, essentially resulting from the breakdown field strength of silicone elastomer, typically 50 to 100 V/μm). On the other hand, a uniform (i.e., no gaps) electrode geometry generates largest electrostatic actuation, however it creates fringe fields only at the electrode periphery, leading to lower electroadhesion force than the interdigitated case.

In this context, the impact of electrode geometry on electroadhesion and electrostatic actuation is assessed through characterization of experimental devices to address the trade-off and an optimized design for the gripper. Additionally, understanding characteristics on electroadhesion is important since our DEA design, a bilayer offset interdigitated electrodes, is essentially different from other existing electroadhesion devices which have electrodes on single surface. Two electrode geometries are used for characterization: an interdigitated shape and a square shape.

First, following experimental investigations are conducted: i) the spatial dependence of the electroadhesion force, ii) the influence of the applied voltage and of the bottom passive layer thickness on the adhesion force, and iii) the actuation (bending) performance. Finally, the performance of the complete gripper is reported.

6.6.1 Spatial Dependence of Electroadhesion Force

The electroadhesion force is proportional to the fringing fields, which are generated mostly at the electrode edge. For a given area, the total edge length for the interdigitated electrode is much longer than that of the square electrode, thanks to the gaps between the segmented boundaries. Hence, one predicts a much larger total electroadhesion force for an interdigitated geometry than for a square geometry, as well as a force nearly uniformly distributed over the area for the interdigitated shape, but only a force localized at the periphery for the square shape.

To visualize spatial distribution of the electroadhesion force, a small probe (20 times smaller area than the total electrode area) is scanned over a test sample while recording the normal component of local electroadhesion force. For this purpose, the experimental samples shown in Figure 6.4(a) that have active overall electrode area of 40 mm × 40 mm with passive outline dimension of 70 mm × 70 mm (Figure 6.4(b)) are used. The thickness of the top and the bottom passive layers are 50 μm. The normal force is measured using a probe of 10 mm diameter at 13 different locations along the lines crossing the center on the electrode (XX' and YY' axes, shown in Figure 6.4(b)). An external motorized stage (Zaber, T-LSR150B) is used to pull the probe and detach it from the device. A load cell is used to measure the force (Applied Measurements, UF1-55). There is no measurable stiction between the passive layer and the probe interface. A paper is used for the probe interface,. During the measurement, a high voltage supply (Auckland Biomimetics Lab, EAP controller) activates the devices with an applied voltage of 2.5 kV. For every measurement, 2 devices are characterized 3 times each, and the average force is reported.

Figure 6.4(c) plots the measured local normal adhesion force at applied voltage of 2.5 kV, and clearly represents the effect of the interdigitated design over the square design. The square electrode generates a local normal force of approximately 15 mN only at the periphery probe positions of 15 mm and 55 mm in XX' and YY' axes), and a force of less than 0.1 mN for all interior points. On the other hand, the interdigitated electrode, the local force is much larger and homogeneous over the electrode surface; ~120 mN on average for all the points on the electrode, more than 1000 times larger force at the interior points compared to the square design. The result proves that the scaling of the electroadhesion force is proportional to the total electrode area for the interdigitated electrode, but only proportional to the periphery length for the square electrode. Also, for the gripper, the uniform electrode configuration will not enable holding an object smaller than the overall electrode area due to the absence of electroadhesion force at the center.

The total electroadhesion force of the interdigitated design can be calculated by dividing the device electrode area (1600 mm^2) by the probe area (78.5 mm^2), and multiplying the measured local normal force (~120 mN), as this design scales the adhesion force proportional to area. Similarly, the total adhesion force of the square design can be obtained from the total periphery of the device (160 mm), the probe diameter (10 mm), and the measured maximum local normal force (~15 mN), based on the fact that this design generates the force only at the electrode periphery. The interdigitated electrode produces 10 times higher total electroadhesion force (~2400 mN) than to the square electrode (~240 mN).

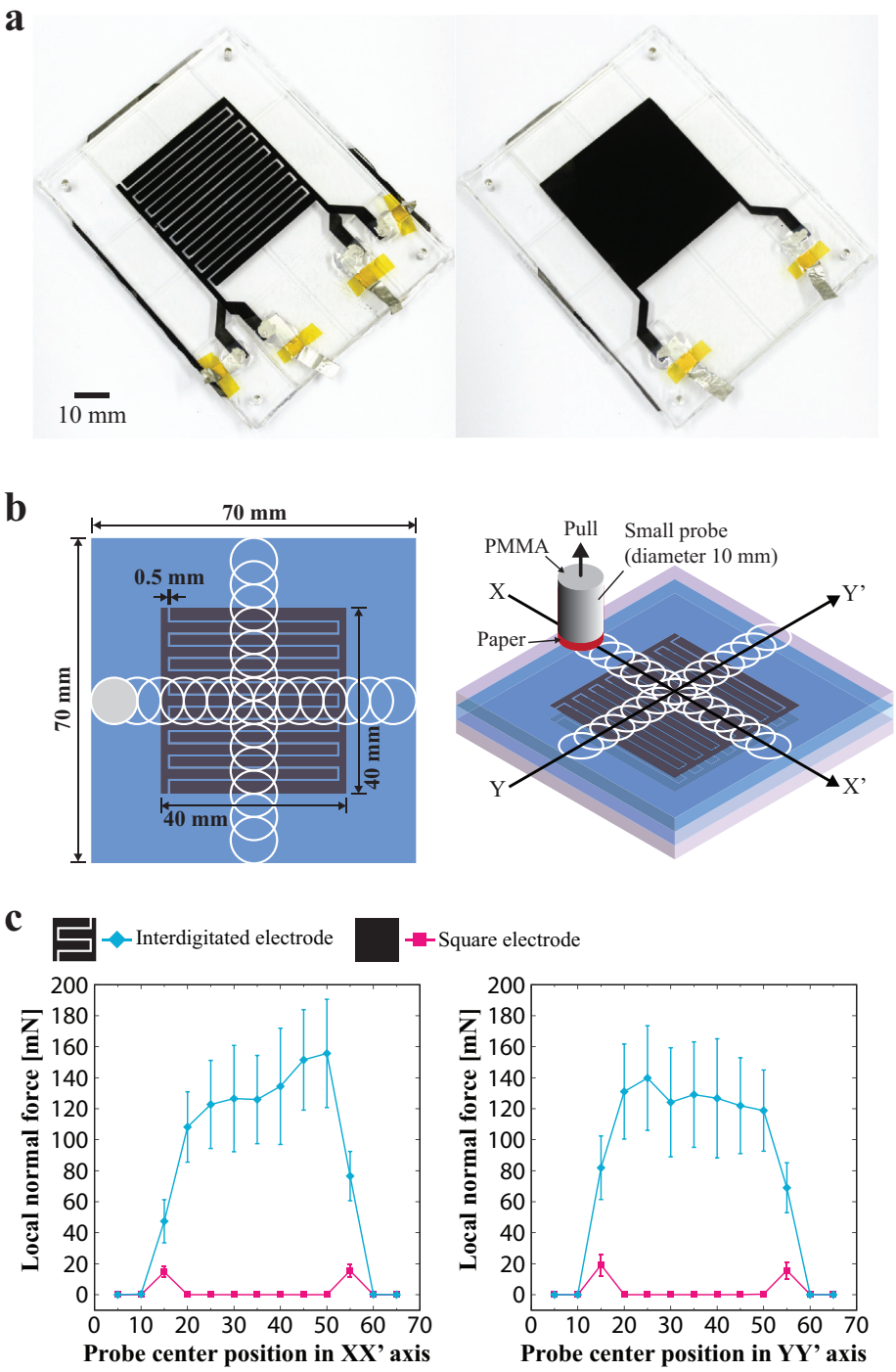

Figure 6.4 – (a) The experimental devices used for the characterization (left: interdigitated, right: square). Electrode area is 40 mm × 40 mm. (b) The local electroadhesion force is measured at 13 points along the lines crossing the center of the devices (XX' and YY' axes) using a probe of diameter 10 mm. (c) (left) The measured local normal electroadhesion force as a function of the probe position for an applied voltage of 2.5 kV in XX' axis, and (right) in YY' axis. The interdigitated electrode generates much larger and more homogeneous local forces over the electrode surface thanks to the segmented electrode boundaries, while the square electrode produces forces only at the periphery. For every measurement, 2 devices are characterized 3 times each, and the average force is reported.

6.6.2 Effect of Applied Voltage and Passive Layer Thickness on Electroadhesion Force

The influence of two important parameters – applied voltage and bottom passive layer thickness – on the magnitude of the electroadhesion force is investigated. It has been analytically and experimentally shown that the magnitude of the electric field, hence the adhesion force, increases with increasing voltage [295, 311, 312, 313] and increases with decreasing insulator thickness (the bottom layer thickness in our case) [312, 314], in electroadhesion devices with single surface electrode.

For this purpose, simplified devices shown in Figure 6.5(a) are characterized. The devices represent one finger of the gripper in a simple square shape to clearly observe the impact of the electrode geometry: active overall electrode area of 10 mm × 10 mm with passive outline dimension of 15 mm × 15 mm. These devices are smaller than those discussed in the previous subsection, but are the same size as the gripping part of the gripper, and allow using a probe covering the entire electrode area (10 mm × 10 mm) to measure the electroadhesion force in both shear force required to displace the probe, and normal force to detach it from the device. The measurement setup is shown in Figure 6.5(c,d), where the bending part of the simplified devices is flattened and fixed on to a PMMA plate to ensure homogeneous interface.

Three voltages (0 V, 2.5 kV, and 5 kV), and two thicknesses of the bottom passive layer (50 μm and 400 μm) are used to see the effect of voltage and thickness on the adhesion force. Figure 6.5(b) shows the cross-section of the device bending part. For the devices with the interdigitated electrode, the thickness of the top passive layer is kept 50 μm. For the devices with the square electrode, no top passive layer facing to the PMMA plate is used, as the electrode on this side is grounded (no need of insulation).

The probe which is connected to a load cell (ATI Industrial Automation, Nano 17), is moved by an external motorized stage (Zaber, T-LSR150B), and a paper is used as the probe interface. There is no measurable stiction between the passive layer and the probe interface. A high voltage supply (Auckland Biomimetics Lab, EAP controller) is used to activate the devices. For every measurement, 4 devices are characterized 3 times each, and their average is reported.

Figure 6.6(a,b) show the measured shear and normal electroadhesion forces as functions of the applied voltage for different bottom passive layer thicknesses. The shear force scales with the voltage and the inverse of the thickness, in the manner described above. At 5 kV, the thinnest passive layer shows the shear force a 3.5 ± 0.3 N (corresponds to 35 ± 3 kPa given the 10 mm × 10 mm overall electrode area) for the interdigitated electrode, and 1.8 ± 0.1 N (18 ± 1 kPa) for the square electrode. The shear forces at zero applied voltage are due to static friction. The normal force (Figure 6.6(b)) scales with both the voltage and the inverse of the thickness in the same way as the shear force does. Since there is no inherent stiction between the passive layer and the interface, no normal force is seen at zero voltage. The normal force at 5 kV is 1.3 ± 0.2 N (13 ± 2 kPa) for the interdigitated electrode, and 0.7 ± 0.1 N (7 ± 1 kPa) for the square electrode.

The factor of two between measured electroadhesion forces for interdigitated and square electrodes is consistent with the ratio of gap lengths producing fringing fields for the two configurations, as in the previous subsection.

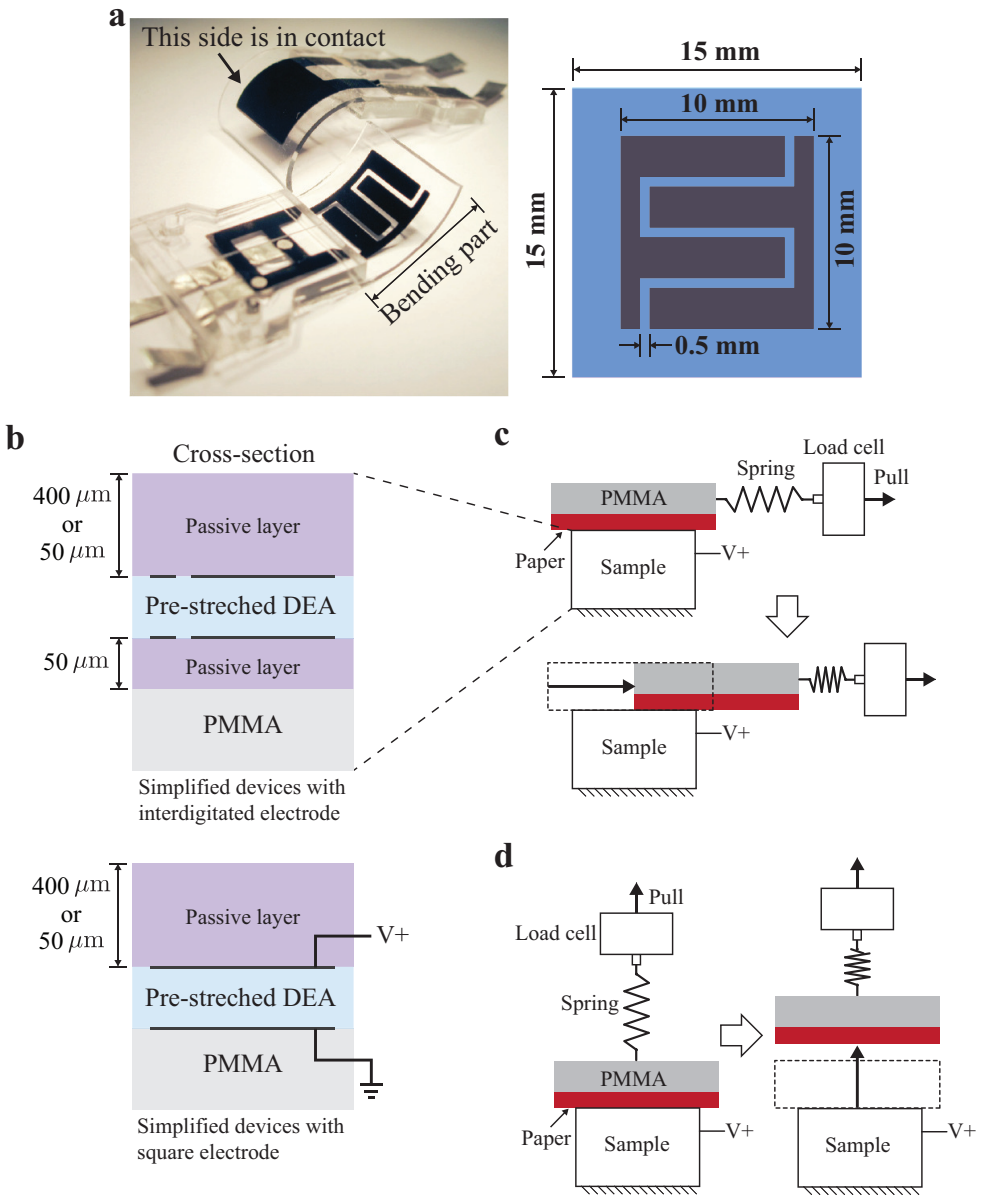

Figure 6.5 – Simplified devices and electroadhesion force measurement setup. (a) The simplified devices used for the characterization (with 400 μm-thick bottom passive layer facing to the interface), and their dimension (bending part). (b) Cross-section of the device bending part when flattened and fixed on to a PMMA plate. No top passive layer facing to the PMMA plate is used for the devices with the square electrode shape, as the electrode on this side is grounded (no need of insulation). (c) The shear force is obtained as maximum detachment force when the interface part consisted of a paper and a PMMA plate is moved by an external motorized stage which is connected to the interface via a load cell, a spring, and a string. The sample is fixed on a mount. To ensure homogeneous interface, a weight of 5 g (not illustrated) is placed on the top of the PMMA plate. (d) With the same setup, the normal force is obtained by changing the moving direction of the interface part.

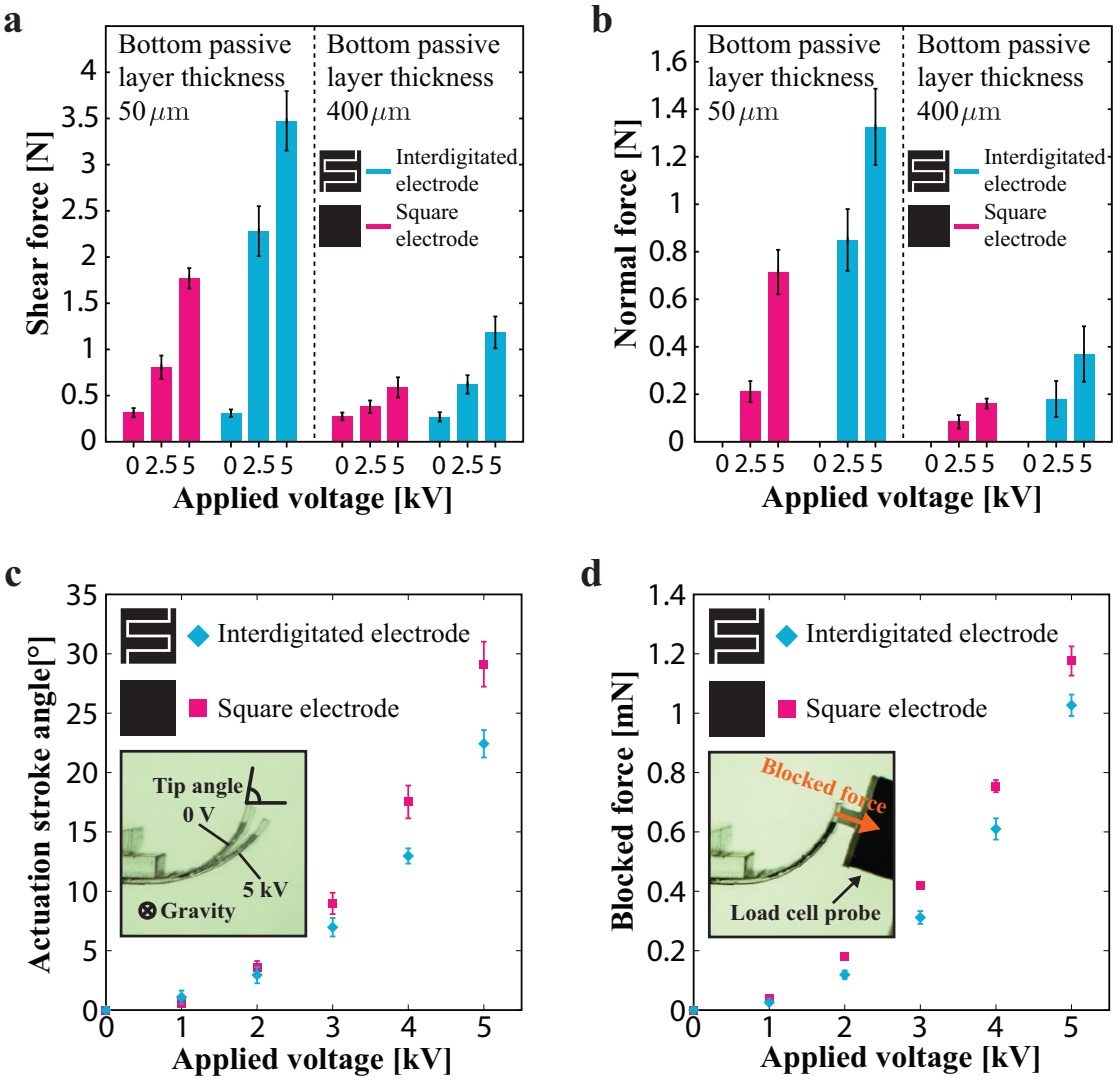

Figure 6.6 – Characterization on the total electroadhesion force and the actuation performance on the simplified devices. (a) The measured shear force as a function of applied voltage for different bottom passive layer thicknesses. The forces at 0 V are due to static friction. (b) The measured normal force as a function of the applied voltage for different passive layer thicknesses. Since there is no inherent stiction between the passive layer and the interface, no normal force is seen at 0 V. (c) The measured actuation stroke angle as a function of the applied voltage. The inset shows the bending actuation of the device with the interdigitate electrode. (d) The measured blocked force as a function of the applied voltage. The inset shows a sample being measured. For every measurement, 4 devices are characterized 3 times each, and their average is reported.

6.6.3 Actuation performance

The actuation stroke angle and the blocked force are characterized as functions of the applied voltage (0 to 5 kV). The same simplified devices discussed in the previous section are used, but only the devices with the bottom layer thickness of 400 μm (Figure 6.5(a)). Compared to full square electrodes, the gaps between the interdigitated electrode are expected to slightly lower the actuation stroke and the blocked force due to the smaller overlapping electrode area across the DEA membrane (83.75 mm^2 in the interdigitated electrode, and 100 mm^2 in the square electrode for the simplified devices).

The actuation stroke angle measured is defined as the tip angle difference from the initial shape i.e., no applied voltage (Figure 6.6(c) inset). A CMOS camera (Point Grey, FMVU-13S2C) and image processing in MATLAB are used to determine the tip angle. A load cell (Applied Measurements, UF1-55) is used to measure the blocked force (Figure 6.6(d) inset). During the measurements, a high voltage supply (Auckland Biomimetics Lab, EAP controller) activates the devices. For every measurement, 4 devices are characterized 3 times each, and their average is reported.

Figure 6.6(c,d) plot the measured actuation stroke angle and the blocked force as functions of the applied voltage. The interdigitated electrode shows the actuation stroke and the force only ~20 % lower than the square electrode, which corresponds to the 20% lower electrode overlap area. The actuation strokes for the interdigitated electrode and the square electrode at 5 kV are 22.4 ± 0.1 ° and 29.1 ± 1.9 °, and the forces at 5 kV are 1.03 ± 0.1 mN and 1.18 ± 0.1 mN, respectively. The magnitude of the blocked force is in the mN order, 3 orders of magnitude smaller than the electroadhesion force. This result expects the gripper to exhibits low mechanical grasping force allowing handling of sensitive objects such as fragile items, while the holding force is provided mostly by the shear electroadhesion force.

6.7 Two-finger Gripper

A two-finger soft gripper, shown in Figure 6.7 is fabricated as a proof of concept to demonstrate its versatility at picking up different object types. The fabrication process for this device is identical to that of the experimental samples characterized in the previous section, and is presented in Section 6.5.

The gripper consists of a 60 μm-thick pre-stretched DEA laminated between a 100 μm-thick top passive silicone layer and a 175 μm-thick bottom passive layer, as shown in Fig 6.7(a). The gripper structure is realized as a planar extension of the DEA design (Figure 6.1(a)), forming a 2-finger shape that can perform open-close motions for picking up and releasing objects. This simple device structure is lightweight (~1.5 g for a 47 mm × 114 mm device with a 10 mm × 10 mm gripping area) and allows for fast movement (it takes ~100 ms to close the fingers). The geometry of the electrodes is designed to provide stronger adhesion forces around the fingertips by the fine interdigitated segmentation, and the other sections generate larger actuation stroke. The gripper can be controlled only by a single control voltage thanks to the simple, compliant composite structure, similar in overall concept to [260, 315, 316, 300, 317, 318, 319].

The gripper is evaluated though demonstration of picking up objects of different types

in a setup shown in (Figure 6.7(b)), where the gripper is raised and lowered by an external motorized stage (Zaber, T-LSR150B) to act as an end effector. A high voltage supply (Auckland Biomimetics Lab, EAP controller) is used to activate the device at 3.5 kV. At zero applied voltage, the gripper has open fingers (curled shape). When the voltage is applied, the fingers are actuated to close around the object—a raw chicken egg in this example—while the electroadhesion force is simultaneously generated. The object is then picked up thanks to the holding force provided by the electroadhesion while the motorized stage is moved. Releasing of the object is achieved by a reverse of the operating procedure explained above. The same operating principle is used for all the objects tested during the demonstration.

The gripper is successful at handling various objects: a raw chicken egg, a fragile, highly deformable water-filled thin silicone membrane balloon, a flat paper, a Teflon tube, and a metallic oil can (Figure 6.7(b-f)). The high compliance of the gripper structure allows the fingers to adapt to the various object shapes. This is ensured by the actuation and the electroadhesion force in the normal direction. While structural compliance has been demonstrated in other soft grippers, the use of electroadhesion gives our devices added functionality and performance. The large holding force provided by the shear electroadhesion force (on the order of Newtons) and the low mechanical grasping force provided by the actuation (on the order of milli-Newtons) allow for handling of fragile objects (Figure 6.7(b)). Moreover, the normal electroadhesion force allows for picking up flat objects (Figure 6.7(d)) without grasping, which is difficult for other universal finger-based grippers given the absence of features that can be grabbed.

The functionality of the gripper is most highlighted when the object is deformable (Figure 6.7(c)). The low mechanical grasping force minimizes the object's deformation when the gripper's fingers close around it, the normal adhesion force keeps the gripper's fingers in conformal contact with the target as it deforms, and the shear adhesion force provides the holding force. The object tested here, a water-filled silicone membrane balloon (the fabrication process is described in Appendix C), is not only highly deformable but also very fragile due to the thin soft membrane (thickness of 25 μm), and it breaks easily when picked up by the human hand. These challenging features would make grasping with conventional grippers extremely difficult. The electroadhesion also enables picking up slippery objects (Teflon tube, Figure 6.7(e)), which can be difficult for other grippers and adhesion technologies especially the Gecko-inspired adhesion [306]. Handling of a metallic oil can (Figure 6.7(f)) proves that the electroadhesion is suited for conductive objects as well as dielectric objects.

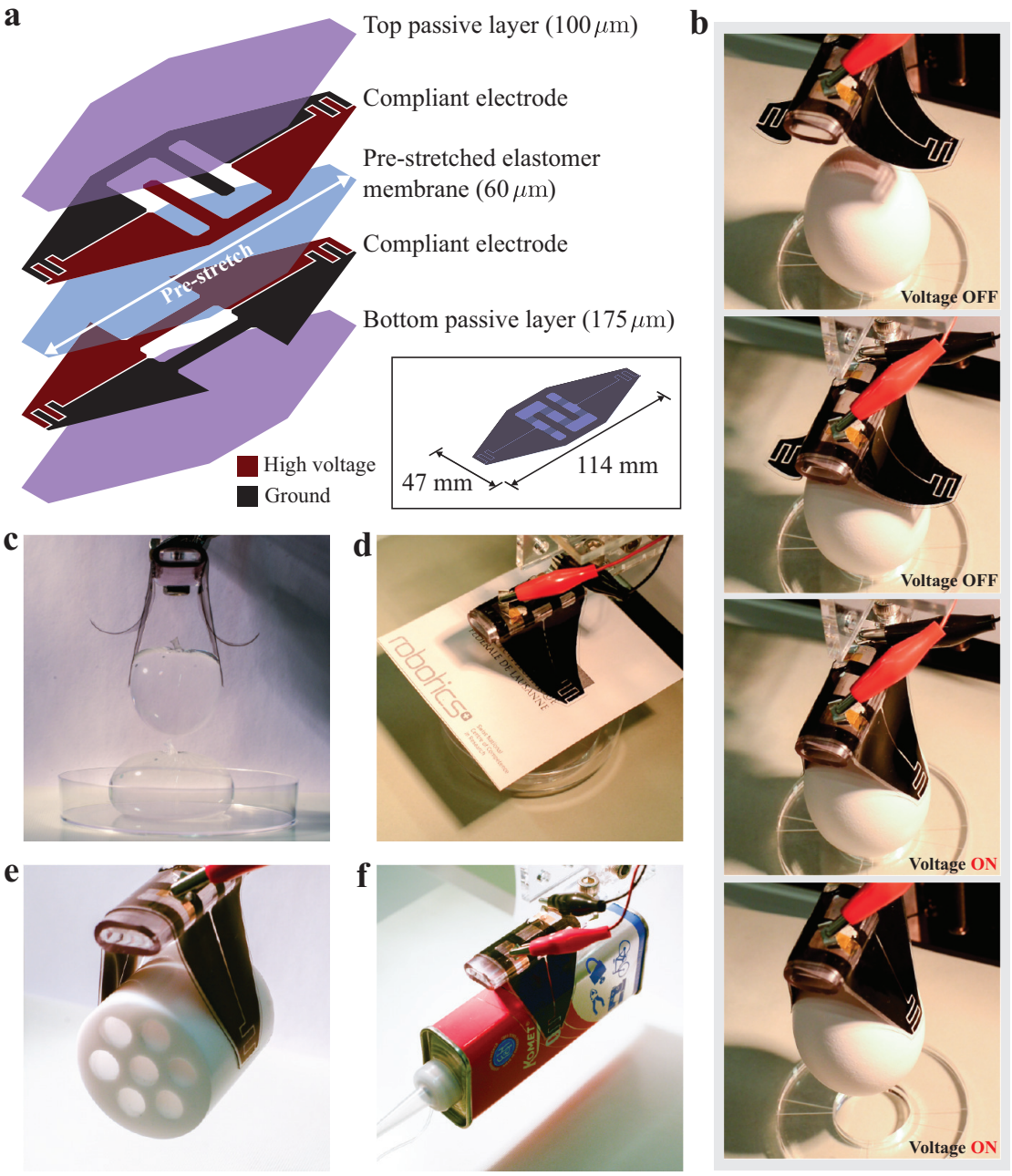

Figure 6.7 – Structure of the electroadhesion-enabled soft gripper, and demonstration of gripping different objects. (a) The gripper consists of a pre-stretched elastomer membrane with patterned compliant electrodes laminated between two passive silicone layers. Different colors of the electrodes represent their polarity (red is positive, and black is negative). (b) Lifting objects is performed using an external motorized stage to raise and lower the gripper. The gripper has open fingers at 0 V. When the voltage is applied, the actuation moves the fingers to close around the object while the electroadhesion force is generated simultaneously. The adhesion force provides sufficient holding force to pick up the target, here a raw chicken egg mass of 60.9 g. With the same operating principle, picking up demonstration is performed for (c) a fragile, highly deformable water-filled thin membrane balloon (35.6 g), (d) a flat paper (0.8 g), (e) a Teflon tube (80.8 g), and (f) a metallic oil can (82.1 g).

6.8 Discussion

The total electroadhesion force generated from the proposed DEA design, a bilayer offset interdigitated electrodes, can be much higher (order of several times) by optimizing the electrode geometry such as the gap and the segmented electrode width, and the thickness of the passive layer (Figure 6.6(a,b)), as has been suggested in electroadhesion devices with single surface electrode [312, 314, 320, 321]. Also, for a fixed electrode area, one could increase the electroadhesion force dramatically by patterning smaller gaps between the lines to enable longer total gap length. One is ultimately limited by fabrication resolution, electrical breakdown in small gaps, and the reduced penetration depth of the fringing in the object, since the fringing distance scales with electrode gap.

The DEA design allows tailoring the location of the interdigitated electrode responsible for the electroadhesion and that for the electrostatic actuation. With this feature, the adhesion force and the actuation can be locally maximized at different desired locations, providing flexibility in designing for different applications as required (e.g., our gripper shown in Figure 6.7(a)). The sensing capability of the device (Appendix B) could enable additional functionalities such as object shape recognition to help understanding the target geometry when such information is not available through other sensors, making it an active smart skin. The interdigitated electrodes can also be used to measure dielectric properties [322] of the object and thus gain insight into its composition.

The developed two-finger soft gripper validates the DEA design by exhibiting a high versatility to handle a wide range of challenging objects. As a grasping device technology, the soft gripper finds potential applications. The low weight of the device makes it easy to incorporate as an end effector in lightweight manipulators or added to small transportation drones [323]. Since silicone is a biocompatible material it can also be used in the medical and food industry (for example, tissue handling by electroadhesion has been reported [324]). Furthermore, this technology can be adopted to produce a wide range of grippers of different size and shape. The homogeneous distribution of adhesion forces on the interdigitated electrode (Figure 6.4(c)) enables scaling in size and the simplicity of the structure enables the design of different gripper shapes, for example with 3 long fingers.

The DEA design described here could also be used for other soft robots beyond grippers. For example, in bioinspired caterpillar robots [325] and gait robots [326], the novel DEA design could achieve kinematically more efficient locomotion by producing controllable high friction force (i.e., electroadhesion force) on the ground surface via actuated body or legs. In those robots, the presence of strong electroadhesion force could also enable wall-climbing functionality (an example based on rigid approach can be seen in [327]). Other example is soft modular robots [328], where the electroadhesion is used for their interconnection, while the actuation provides movements of each modular robot for their localization and of the entire connected structure. Finally, all the applications mentioned above can benefit from the simple, highly integrated system thanks to its multifunctionality—electroadhesion, actuation with different output characteristics, and sensing—as highlighted in the presented soft gripper.

7 Conclusion

In this thesis, functional soft actuators based on dielectric elastomer actuators (DEAs) were investigated. The investigation was conducted through development of novel actuators: (1) foldable antagonistic dielectric elastomer actuator, (2) variable stiffness dielectric elastomer actuator, and (3) electroadhesion dielectric elastomer actuator. The results address a method to create the functionalized robots with simplified actuator configurations, and expand the use of DEAs in robotics.

7.1 Summary

The foldable antagonistic dielectric elastomer actuator consists of 2 sets of pre-stretched DEAs forming a simple antagonistic configuration that enables bidirectional actuation and passive folding. The actuators were designed and fabricated with specification matching to a micro aerial vehicle (MAV) that had 400 mm wingspan and mass of ~130 g. In the MAV, the actuators were used as elevons (control surfaces). A closed-form analytical model of the actuator was constructed to guide the actuator design. The fabricated elevon actuator exhibited voltage-controllable angular displacement (± 26 °) and torque (2720 mN·mm) at 5 kV, while the model prediction showed good agreement to the measured data. Two elevon actuators were integrated into the MAV. The actuators were evaluated in terms of the controllability of the MAV by calculating the correlation between the control signal and the MAV motion. During a flight, the actuators well controlled the MAV attitude in the desired direction from a takeoff to a ground landing, which resulted in a strong correlation of over 0.7 between the control signal and the MAV motion in roll axis. The developed MAV demonstrated a practical use of the actuator.

The variable stiffness dielectric elastomer actuator (VSDEA) consists of a uniaxially pre-stretched DEA bonded on a low-melting-point alloy (LMPA) embedded silicone substrate. The actuator is simple (composed of only two parts), and expected to allow a high design flexibility. In the actuator, the DEA generates a bending actuation, and the LMPA changes its phase between solid and liquid by Joule heating, providing controllable stiffness of the structure between soft and rigid states. A proof of concept actuator was fabricated, which had dimension of 40 mm length × 10 mm width × 1 mm thickness and mass of ~1 g. The fabricated VSDEA showed voltage-controlled bending actuation with a large stroke angle (47.5 ± 7.2 °) at 3 kV, and good repeatability in the soft state. In the rigid state, the actuator maintained

almost same shape, only 1.1 ± 0.8 ° angle difference was observed at 3 kV. The rigid state also exhibited a spring constant of 23.3 mN/mm, which was ~90× larger compared to an actuator without LMPA (0.26 mN/mm). A two-finger gripper consisted of 2 VSDEAs was developed. The gripper successfully picked up the object mass of ~11 g (108 mN) by appropriately using the soft and rigid states, even though the actuated grasping force was only 2.4 mN. The gripper demonstrated a practical use of the actuator, and proved that variable stiffness functionality enables simplified actuator configuration therefore the robot.

The electroadhesion dielectric elastomer actuator consists of a DEA sandwiched between two passive silicone layers. The structural simplicity of the actuator is expected to allow a high design flexibility. In the actuator, the DEA has a design employing an interdigitated electrode geometry that simultaneously maximizes electroadhesion and electrostatic actuation. The actuator also allows self-sensing the bending angle by measuring the capacitance change between the electrodes. The concept of the actuator was validated through development of a two-finger soft gripper. To address an optimal design, experimental devices were characterized. The characterization results showed that the proposed DEA design has advantage for grasping application over traditional DEAs, as it can produce up to 10 times higher electroadhesion forces at the cost of only ~20 % reduction in actuation performance. The results also represented high holding force of the gripper (3.5 N shear force for 1 cm^2) and low mechanical grasping force (1 mN). The two-finger soft gripper is lightweight (~1.5 g for a 47 mm × 114 mm device with a 10 mm × 10 mm gripping area), fast (it takes ~100 ms to close the fingers), all-silicone, composed of single structure, and can be controlled with simple control input (switch on and off of the voltage). The gripper showed a high versatility to pick up objects of different types, such as a fragile, highly-deformable water-filled thin membrane balloon (35.6 g), a flat sheet of paper (0.8 g), a raw chicken egg (60.9 g), a Teflon tube (80.8 g), and a metallic oil can (82.1 g). The fact that handling of such a wide range of challenging objects is achieved by a single device with simple control input, is a main advantage of our gripper over other existing grippers. The gripper demonstrated a practical use of our DEA design, and proved that adhesion functionality enables simplified actuator configuration therefore the robot.

7.2 Future Work

Future work for the foldable antagonistic dielectric elastomer actuator could address development of fully foldable robotic systems. It would be interesting to create a completely foldable version of the current MAV because it would show how the foldability of the entire airframe affects the robot's performance. A concept of the foldable MAV is presented in Appendix D. A redesign of the actuator structure should be tried to reduce the number of parts, which may simplify the fabrication and improve the actuator performance in terms of the specific power.

Future work for the variable stiffness dielectric elastomer actuator could address further characterization and optimization including the bidirectional configuration such as the detailed stiffness change and heating/cooling time. Cooling time reduction should be tried. For this purpose, increasing the surface area of the actuator with a heatsink like geometry, or the use of cooling water injected in additional channel could be a solution. The LMPA substrate loses conductivity when the alloy track is physically broken due to large external loads [269]. Self-healing capability that covers the failure mode of the LMPA substrate should be addressed. Solution for self-healing the broken track could be the use of carbon black-filled elastomers implemented as the wall of the LMPA channels to keep conductivity.

Future work for the electroadhesion dielectric elastomer actuator could address characterization on the different output characteristics (Figure 6.2 in Section 6.4), which may contribute to define suitable operating principle for given application types. In parallel, further characteristics on electroadhsion such as more detailed investigation of the electric field distribution should be studied. When the electrode gap is significantly larger than the thickness of the DEA, the form of the fringing fields on the surface could be different from what is shown in Figure 6.1(b) in Section 6.4; strong fringing fields generating adhesion may be created more in the direction across the thickness. For this purpose, analytical and computational models should be associated to help the characterization. It would be interesting to implement other electrode geometries such as spiral, concentric circle, and Hilbert curve [321], because it could increase the adhesion force, or change the actuation and the sensing behaviors.

Regarding all the actuators, obtaining more detailed actuation characteristics such as dynamic behaviors (e.g., response speed to determine operating frequency), repeatability, and their behavior in different device size scale are remaining. These works and optimization of actuation performance (stroke, force, etc.) in terms of mechanical parameters (e.g., prestretch ratios) could enable development of varied robotic applications. Further investigation of self-sensing capability could address additional functionalities such as shape recognition and composition acquisition of external objects, as mentioned in Section 6.8. Further consideration on the material selection could contribute to improve the actuator performance. For example, a lighter material with the same elastic modulus increases the specific power. For those works, construction of more accurate analytical and computational models including dynamic behavior should be followed. Extension of such models for robotic applications would greatly help their designing, but challenging. Apart from the work on each actuator, combining two or all of the three functionalities would address advanced actuator configurations and robotic applications. Similarly, integration of other DEA capabilities such as self-sensing, self-healing, switching, energy harvesting, and color change would greatly expand the potential

applications, and bring unprecedented types of robots.

The electrode directly effects to the actuation performance of DEAs. Therefore, realization of electrodes with higher compliance, better conductivity and repeatability, longer lifetime, and thinner matrix is a challenge. Additionally, investigation of elastomer that has better properties such as higher breakdown strength may be a way to improve the performance. Voltage reduction is another challenge and has a great potential. Removing the need of high-voltage supply makes robots simple and compact, and would expand potential applications. For this purpose, stacking ultra thin DEAs could be a solution, however, extensive developments of fast, accurate, and low cost fabrication process may be inevitable.

Robotics grows. Our society and daily life will see robots that are very common. After the selection, soft actuator technologies existing today would be developed to form active intelligent material rather than actuation component. There sensors, haptics, harvesters, batteries, healers, and computations are integrated. At this time, the existence of robots changes from something that has to be designed beforehand to something that obtains the design oneself in response to given conditions and environments. Robots are no longer assembled components but the material itself. Such intelligent material is scalable and extremely low cost, spreading into the world. For instance, when placed on a human body, it understands optimal shapes and physical assistive outputs through communication with the person based on haptics and visuals. Eventually, self-propagation and self-modification are integrated. At some point in infinite attempts of responses to stimulus, the material would cause intelligence. The scenery from there will surely be beautiful. The functional soft robotic actuators developed in this thesis and the initial results provide an excellent starting point.

A Model of Variable Stiffness Actuator

In this chapter, we explain a closed-form analytical model to predict the actuation stroke angle of variable stiffness dielectric elastomer actuator (VSDEA) discussed in Chapter 5, based on the total potential energy in the system similar to the one explained in Section 4.3. The model outputs the bending angle at an equilibrium state for a constant applied voltage.

The bending angle θ is determined by calculating the local minimum of the potential energy U_{tot}.

$$\frac{\partial U_{\text{tot}}}{\partial \theta} = 0, \text{and } \frac{\partial^2 U_{\text{tot}}}{\partial \theta^2} > 0, \tag{A.1}$$

U_{tot} consists of the potential energy of the DEA U_{DEA} and the bending energy of the LMPA substrate U_{hinge}. Two energies are involved in U_{DEA}: the strain energy of the DEA U_{strain}, and the electrostatic energy U_{electric}.

$$U_{\text{tot}} = U_{\text{strain}} + U_{\text{electric}} + U_{\text{bending}}. \tag{A.2}$$

In the model, the rigidity of the substrate is represented by the torsional spring stiffness k [241, 242] to calculate U_{bending}.

$$U_{\text{bending}} = \frac{1}{2} k\theta^2 = \frac{1}{2} \frac{EI_s}{l_s} \theta^2, \tag{A.3}$$

where EI_s and l_s are the bending stiffness (flexural rigidity) and the length of the substrate, respectively. EI_s is product of elastic modulus E and second moment of area I. Equation A.3 means the substrate is expressed as a uniform plate. Therefore, the model allows to incorporate not only the LMPA substrate but also other materials such as a pure silicone.

Figure A.1(a) shows the cross-section of VSDEA in the flat state (i.e., just after attaching the DEA). To calculate the bending stiffness EI_s, the structure of the actuator is considered as a composite consisted of layers representing the DEA, the silicone matrix, and the LMPA channel. This allows to calculate the second moment of area of each layer, and their integration gives EI_s. Since the structure is symmetric in the x direction, the centroid of the cross-section y_n is

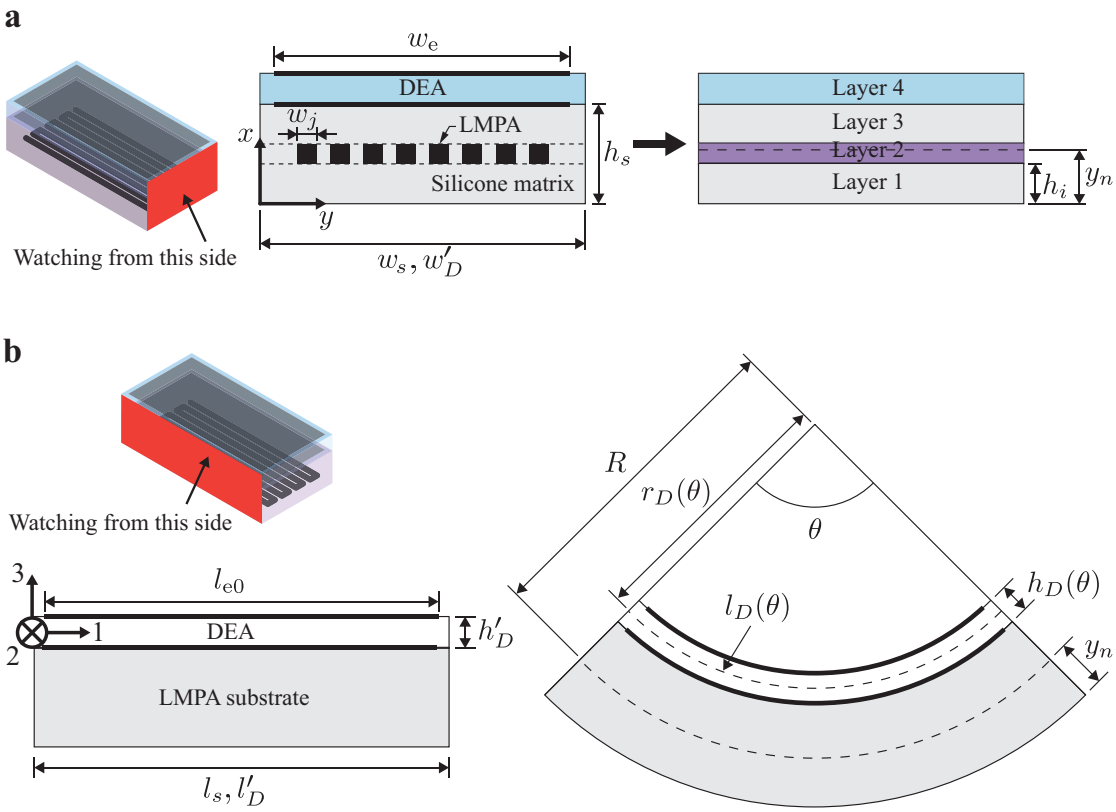

Figure A.1 – VSDEA model schematics. (a) The cross-section of VSDEA in the flat state. The structure is considered as a composite consisted of layers. (b) Schematics of VSDEA model watching from the lateral side.

given as

$$y_n = \frac{\sum_i E_i y_i A_i}{\sum_i E_i A_i}, \tag{A.4}$$

where, E_i and A_i are the elastic modulus and the cross-sectional area of the i^{th} layer ($A_i = w_s \cdot h_i$), respectively, and y_i is the distance to the center of the layer from the bottom of the substrate. The elastic modulus of the LMPA layer (layer 2 in Figure A.1(a)), E_2 is approximated as

$$E_2 = \frac{E_{\text{LMPA}} \sum_j^N w_j + E_{\text{silicone}}(w_s - \sum_j^N w_j)}{w_s}, \tag{A.5}$$

where E_{LMPA} is the elastic modulus of the LMPA, E_{silicone} the elastic modulus of the silicone, w_j the width of the j^{th} channel, N the number of channels, and w_s is the width of the substrate. As mentioned in Section 5.3, we consider two extreme cases for the LMPA: solid and liquid. Equation A.5 allows to include the solid and liquid phases, when their elastic modulus is given. In the liquid phase, we assume the modulus of the LMPA is same as that of the silicone matrix

($E_{\mathrm{LMPA}} = E_{\mathrm{silicone}}$). EI_s is then calculated by integration of the second moment of area on the layers except for the DEA, based on the parallel axis theorem [329].

$$\begin{aligned} EI_s &= \sum_i E_i \left\{ I_i + (y_i - y_n)^2 A_i \right\}, \\ I_i &= \frac{w_s h_i^3}{12}. \end{aligned} \tag{A.6}$$

During the actuation, we assume the thickness of the substrate and y_n are constant, while the strain of the DEA changes therefore the strain energy U_{strain}. Figure A.1(b) is a schematics of the actuator watching from the lateral side. The radius of curvature of the actuator R is defined as

$$R = \frac{l_s}{\theta} = h_s - y_n + r_D(\theta) + \frac{h_D(\theta)}{2}, \tag{A.7}$$

where h_s is the thickness of the substrate, and $h_D(\theta)$ is the thickness of the DEA. $r_D(\theta)$ is the radius of curvature of the DEA given as

$$r_D(\theta) = \frac{l_D(\theta)}{\theta}, \tag{A.8}$$

where $l_D(\theta)$ is the length of the DEA. Due to the incompressibility of the elastomer (Section 3.1), the volume of the DEA is constant, thus:

$$\begin{aligned} & l'_D \cdot w'_D \cdot h'_D = l_D(\theta) \cdot w'_D \cdot h_D(\theta), \\ & \therefore h_D(\theta) = \frac{l'_D \cdot h'_D}{l_D(\theta)}, \end{aligned} \tag{A.9}$$

where l'_D, w'_D, and h'_D are the length, the width, and the thickness of the DEA in the flat state (i.e., the pre-stretched state shown in Figure 5.1(a)). w'_D is assumed to be constant during the actuation. Substituting Equations A.8 and A.9 into Equation A.7, and using the fact $l'_D = l_s$

$$\{l_D(\theta)\}^2 + \left\{(h_s - y_n)\theta - l_s\right\} l_D(\theta) + \frac{l_s h'_D}{2}\theta = 0. \tag{A.10}$$

Solving Equation A.10 gives the length of the DEA as a function of the bending angle.

$$l_D(\theta) = \frac{1}{2}\left[l_s - (h_s - y_n)\theta + \sqrt{\left\{(h_s - y_n)\theta - l_s\right\}^2 - 2 l_s h'_D \theta} \right]. \tag{A.11}$$

The stretch ratios of the DEA are then given as

$$\lambda_1(\theta) = \frac{l_D(\theta)}{l_s}\lambda_{1\mathrm{p}}, \quad \lambda_2 = \frac{1}{\sqrt{\lambda_{1\mathrm{p}}}} = \text{constant}, \quad \lambda_3(\theta) = \frac{\sqrt{\lambda_{1\mathrm{p}}}}{\lambda_1(\theta)}, \tag{A.12}$$

where λ_1, λ_2, and λ_3 are the stretch ratio in the direction 1, 2, and 3, respectively, as indicated in

Figure A.1(b). Direction 1 and direction 2 refer to the length direction and the width direction of the actuator, respectively, and direction 3 is along the thickness direction. Equation A.12 takes account of the incompressibility of the elastomer, and incorporates the pre-stretch uniaxially applied along the direction 1, $\lambda_{1\mathrm{p}}$. λ_2 is constant as the width of the actuator is fixed.

We use the Neo-hookean hyperelastic model [330] as a strain energy density function W to express U_{strain} by the stretch ratios.

$$W = \frac{\mu}{2}(I_1 - 3), \tag{A.13}$$

where μ is the shear modulus of the DEA elastomer, and $I_1 = \lambda_1^2 + \lambda_2^3 + \lambda_3^2$. By substituting Equation A.12 into Equation A.13, U_{strain} is obtained as

$$\begin{aligned} U_{\mathrm{strain}} &= Vol \cdot W(\theta) = Vol \cdot \frac{\mu}{2}(I_1(\theta) - 3), \\ I_1(\theta) &= \{\lambda_1(\theta)\}^2 + \frac{1}{\lambda_{1\mathrm{p}}} + \frac{\lambda_{1\mathrm{p}}}{\{\lambda_1(\theta)\}^2}, \\ Vol &= l'_D w'_D h'_D, \end{aligned} \tag{A.14}$$

where Vol is the volume of the DEA.

The electrostatic energy of the DEA U_{electric} is then expressed as

$$\begin{aligned} U_{\mathrm{electric}}(\theta) &= -\frac{1}{2}C(\theta)V^2 = -\frac{1}{2}\varepsilon_0\varepsilon_{\mathrm{r}}\frac{A_{\mathrm{e}}(\theta)}{h_D(\theta)}V^2, \\ A_{\mathrm{e}}(\theta) &= l_{\mathrm{e}}(\theta)\, w_{\mathrm{e}} = l_{e0}\frac{\lambda_1(\theta)\, w_{\mathrm{e}}}{\lambda_{1\mathrm{p}}}, \\ h_D(\theta) &= h'_D\lambda_3(\theta) = \frac{h'_D\sqrt{\lambda_{1\mathrm{p}}}}{\lambda_1(\theta)}, \end{aligned} \tag{A.15}$$

where C is the capacitance of the DEA, ε_0 the permittivity of free space, ε_{r} the relative permittivity of the elastomer, V the DEA applied voltage, and A_{e}, l_{e}, and w_{e} are the area, the length and the width of the electrode, respectively. l_{e0} is the initial length of the electrode, which corresponds to the dimension when the actuator is flat. U_{electric} is negative as the voltage-controlled case is considered [272].

As all the energies U_{bending}, U_{strain}, and U_{electric} are functions of θ, Equation A.1 becomes a differentiation of U_{tot} with respect to θ, that is:

$$\frac{dU_{\mathrm{strain}}}{d\theta} + \frac{dU_{\mathrm{electric}}}{d\theta} + \frac{dU_{\mathrm{bending}}}{d\theta} = 0. \tag{A.16}$$

Differentiation of Equations A.3, A.14, and A.15 with respect to θ gives each term in Equation A.16. Solving Equation A.16 finds θ as a function of the applied voltage V.

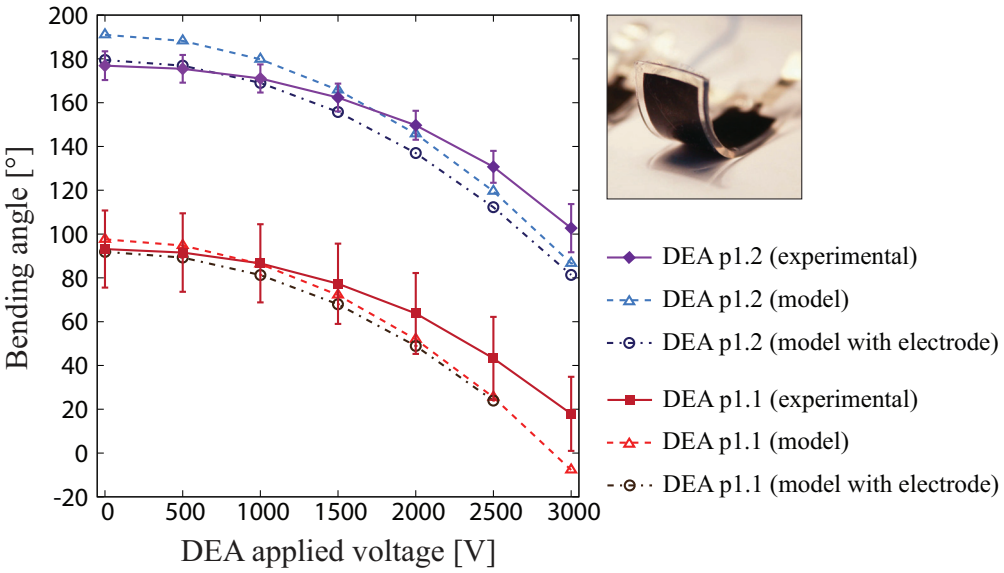

Figure A.2 – Bending angle of actuators without LMPA as a function of the DEA applied voltage for different DEA pre-stretch. Two types of experimental samples are measured: one has pre-stretch of 1.1 (p1.1), and the other has 1.2 (p1.2). The inset shows the actuator with pre-stretch of 1,1. The model shows good agreement, especially the presence of the electrodes is considered. 6 samples are measured for each type, and their average is reported.

Figure A.2 plots a comparison between the model and a set of experimental data of actuators without LMPA (i.e., with a pure silicone substrate), on the bending angle as a function of the DEA applied voltage. In the experimental data, two types of actuator samples are measured: one has pre-stretch of 1.1, and the other has pre-stretch of 1.2. The inset in this figure shows the actuator with pre-stretch of 1.1. The model shows good agreement to the measured data. We next implement the presence of the electrodes in the model. In this case, Equation A.2 becomes

$$U_{\text{tot}} = U_{\text{strain}} + U_{\text{electric}} + U_{\text{bending}} + U_{\text{strain\_electrode}}, \tag{A.17}$$

where the electrodes are modeled as passive layers creating another strain energy $U_{\text{strain\_electrode}}$, and assumed that their deformation during the actuation follows the length of the DEA $l_D(\theta)$.

$$\begin{aligned}
&U_{\text{strain_electrode}} = 2Vol_{\text{e}} \cdot W_{\text{e}}(\theta) = Vol_{\text{e}} \cdot \mu_{\text{e}}(I_{\text{e1}}(\theta) - 3),\\
&I_{\text{e1}}(\theta) = \{\lambda_{\text{e1}}(\theta)\}^2 + {\lambda_{\text{e2}}}^2 + \{\lambda_{\text{e3}}(\theta)\}^2,\\
&\lambda_{\text{e1}}(\theta) = \frac{\lambda_1(\theta)}{\lambda_{\text{p1}}},\ \lambda_{\text{e2}} = 1,\ \lambda_{\text{e3}}(\theta) = \frac{1}{\lambda_{\text{e1}}(\theta)},\\
&Vol_{\text{e}} = l_{\text{e0}}\lambda_{\text{e1}}(\theta)\, w_{\text{e}} h_{\text{e0}} \lambda_{\text{e3}}(\theta),
\end{aligned} \tag{A.18}$$

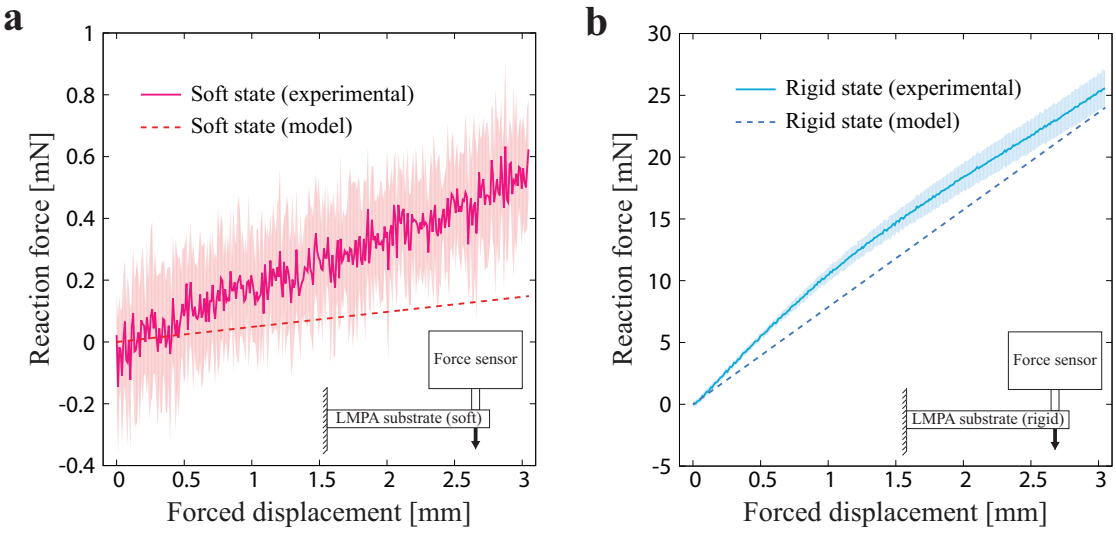

Figure A.3 – Reaction force of an LMPA substrate as a function of the forced displacement for (a) the soft and (b) rigid states. For the experimental data in the soft state, the LMPA substrate shows a small reaction force due to a high compliance of the structure. There is significant difference between the measured data and the model prediction. For the experimental data in the rigid state, the LMPA substrate shows a large reaction force thanks to a high structural rigidity. The model shows good agreement to the data. For every characterization result, one LMPA substrate is measured 3 times and the average is taken.

where $\lambda_{e1}(\theta)$, λ_{e2}, and $\lambda_{e3}(\theta)$ are the stretch ratios of the electrodes, Vol_e the volume of the electrodes, and h_{e0} is the initial thickness.

The model prediction with electrodes is shown in Figure A.2. The prediction is more close to the measured data compared to the model without electrodes, in terms of the initial angle (i.e., no applied voltage) and the actuation stroke angle. Table A.1 summarizes the parameters used for the models.

We have observed that when the substrate has the LMPA channels (VSDEA), the model prediction for the soft state shows a large difference on the initial angle and the actuation stroke angle, compared to that of the real actuators. This may be resulted from the fact that the LMPA channels in the liquid phase resist to the bending of the entire substrate. Figure A.3 shows the reaction force of a flat LMPA substrate as a function of the forced displacement for the soft and rigid states. The reaction force F_R is calculated as a point force acting on a cantilever, based on the Euler beam bending equations [329], that is:

$$F_R = \frac{3EI_s}{l_s'^3}x, \tag{A.19}$$

where l_s' is the effective length of the LMPA (distance between the fixed boundary and the point force), and x is the forced displacement.

In the soft state (Figure A.3(a)), the LMPA substrate exhibits significantly larger reaction force compared to the calculation result, while the rigid state (Figure A.3(b)) shows good agree-

Table A.1 – Model parameters of the actuators without LMPA

Parameter	Value
Dimensions	
DEA	
Length after pre-stretch l'_D	27 mm[*1]
Width after pre-stretch w'_D	10 mm
Thickness after pre-stretch h'_D	42.5 μm
DEA electrode	
Initial length l_{e0}	26 mm[*1]
Width w_e	8 mm
Initial thickness h_{e0}	2 μm[*2]
Substrate	
Length l_s	27 mm[*1]
Width w_s	10 mm
Thickness h_s	1 mm
Material property	
DEA elastomer (NuSil Technology, CF19-2186)	
Relative permittivity ε_r	2.8 [233, 243]
Shear modulus μ	0.28 MPa [126]
DEA electrode	
Shear modulus μ_e	0.64 MPa [126]
Substrate (Bluestar, Silbione LSR 4305)	
Elastic modulus $E_{silicone}$	0.2 MPa [126]
Other parameter	
Pre-stretch ratio λ_{1p}	1.1, 1.2
Permittivity of free space ε_0	8.85×10^{-12} F/m

[*1] Values are effective length from fixing part.
[*2] Medium value of reported thickness 1-4 μm [125, 126].

ment. This means that, in the soft state, the liquid phase LMPA adds a rigidity (mechanical resistance to the bending of the substrate), and can not be considered as the silicone matrix (as assumed in Equation A.5). The bending of the substrate may be happening in the way changing the volume of the LMPA filled channels. The volume change of the channels (i.e., the bending) is prevented by the liquid phase LMPA which is incompressible. Therefore, for accurate prediction of the actuation behavior of VSDEA in the soft state, the actuator model requires further consideration of the LMPA in the liquid phase, and is omitted from discussion in Chapter 5. Table A.2 summarizes the parameters used for the reaction force calculation.

Table A.2 – Parameters used for the reaction force calculation

Parameter	Value
Dimensions	
LMPA Substrate	
Length l_s'	25 mm*
Width w_s	10 mm
LMPA channel width w_j	0.45 mm
Number of channels N	8
Thickness of layer 1 (silicone) h_1	0.4 mm
Thickness of layer 2 (LMPA) h_2	0.35 mm
Thickness of layer 3 (silicone) h_3	0.4 mm
Material property	
Substrate (Bluestar, Silbione LSR 4305)	
Elastic modulus E_{silicone}	0.2 MPa [126]
LMPA (HiTech Alloys, Cerrolow 117)	
Elastic modulus E_{LMPA}	3.0 GPa [269]

* Value is effective length (distance between the fixed boundary and the point force).

B Self-Sensing Characteristics of The DEA design

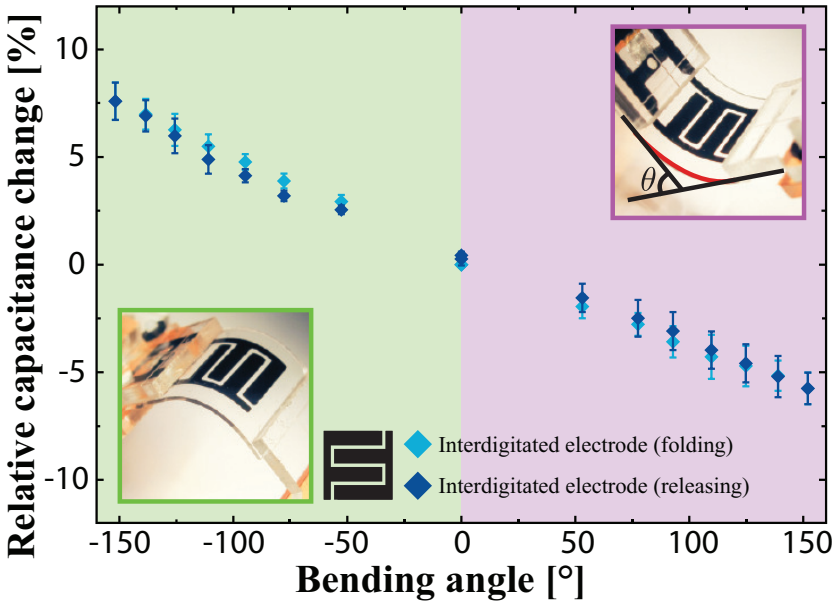

Figure B.1 – Measured capacitance as a function of the bending angle.

In the DEA design for the two-finger soft gripper presented in Section 6.4, the larger percentage change in capacitance of the device enables self-sensing of the bending angle. We measure the capacitance of the simplified devices used in the characterization described in Section 6.6.3. The samples are wired in the same way as the gripper configuration (Figure 6.1(b)), where a LCR meter (Agilent E4980A) is used to measure capacitive changes. The structure is passively bent in two directions using a manual linear stage while the bending angle θ is measured with a CMOS camera (Point Grey, FMVU-13S2C). Figure B.1 plots the measured capacitance as a function of the bending angle. The outline colors of the insets correspond to the positive or the negative bending angle which are shown in the corresponding color domains. Due to different thicknesses in the passive layers (50 μm and 400 μm), the devices show capacitance change in two bending directions up to $\pm$ 150 °. In this measurement, 4 samples are measured 3 times each and their average is taken. The average capacitance at 0 ° is 39.9 pF.

C Fabrication of Water-Filled Thin Membrane Balloon

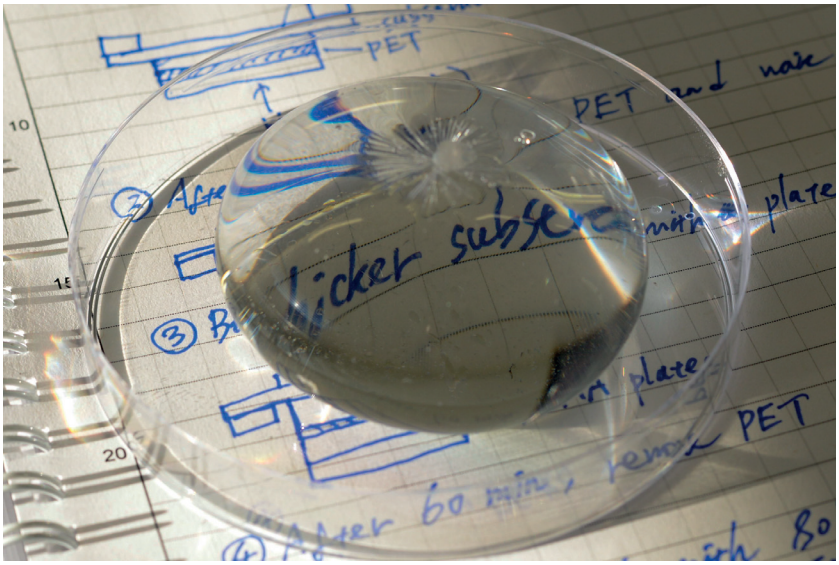

Figure C.1 – Fabricated water-filled thin membrane balloon. The twisted part can be seen on the top.

A soft silicone membrane (Bluestar, Silbione LSR 4305, 0.2 MPa elastic modulus [126]) of thickness 25 μm is produced using the same fabrication process as for the DEA membranes, and mounted in a Polymethyl methacrylate (PMMA) circular holding frame using a silicone adhesive foil (Adhesives Research, ARclear 8932EE) without any pre-stretch. Water was poured on the membrane, resulting in a bowl shape due to weight of the water. The membrane is carefully twisted to close the opening, forming a balloon which is sealed using a silicone glue (Dow Corning, 734 flowable sealant). Figure C.1 shows a fabricated water-filled thin membrane balloon.

D Concept of Foldable Micro Air Vehicle

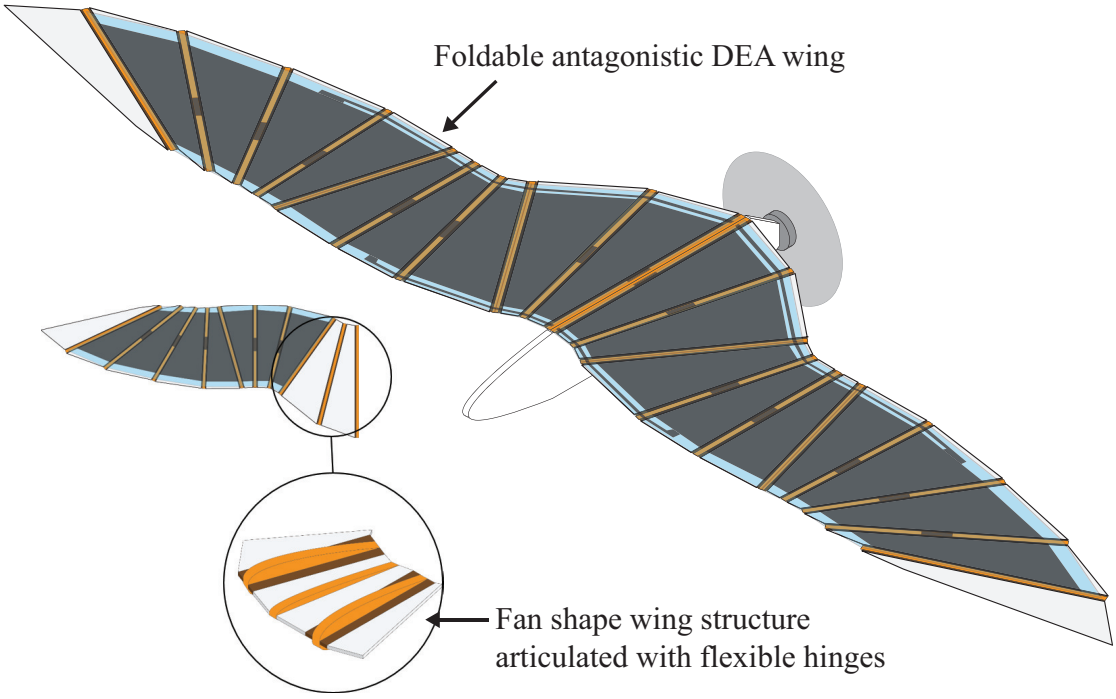

Figure D.1 – Schematic of the foldable MAV. The articulated wing consists of the foldable antagonistic dielectric elastomer actuators, allowing passive folding.

This chapter presents a concept of foldable micro air vehicle (MAV). Figure D.1 shows a schematic of the foldable MAV that has articulated wing composed of the foldable antagonistic dielectric elastomer actuators presented in Chapter 4. The articulated wing structure allows passive folding along the spanwise direction.

The articulated pattern is designed to mimic the folding mechanism of bird wing, as shown in Figure D.2. This bio-mimetic wing folding is similar to DALER, which uses the folding for multi-modal locomotion [229]. What differs from the study is that the wing presented here is active. As shown in Figure D.3, partial activation of the distributed DEAs on the articulated pattern enables bending and twisting of the wing, allowing control of the MAV in roll and pitch axes.

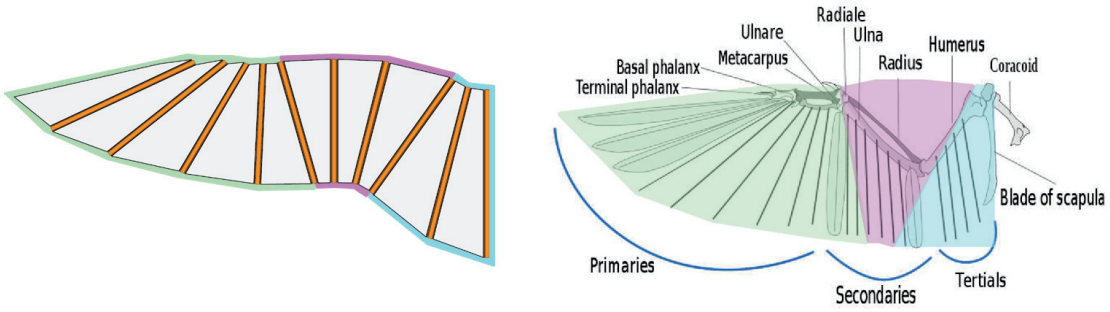

Figure D.2 – Folding mechanism of the wing.* The articulated pattern mimics the folding mechanism of bird wing.

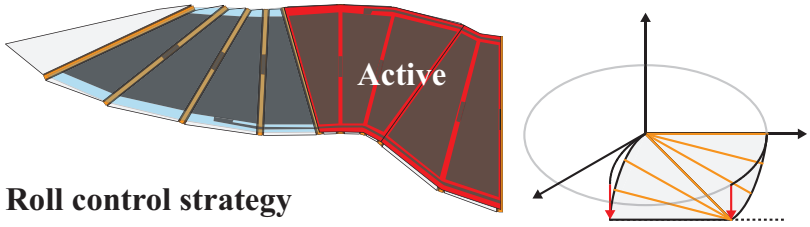

Roll control strategy

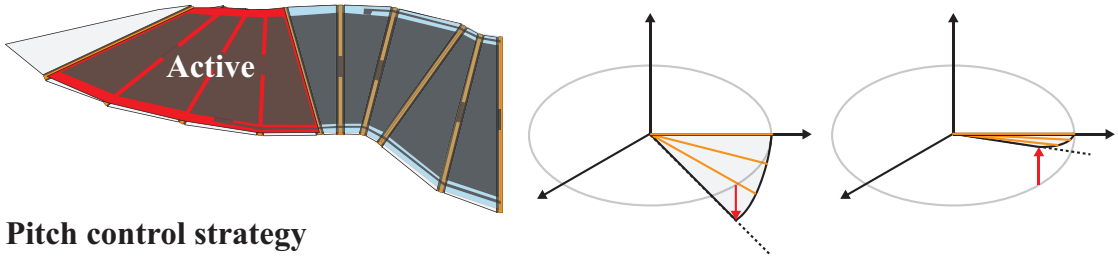

Pitch control strategy

Figure D.3 – Control strategy of the foldable MAV. The wing has the active regions to generate roll and pitch motions separately. Roll motion is achieved by pure bending actuation of the wing. Pitch motion is achieved by twist actuation.

Main concern on the foldable MAV is the flexibility of the wing, which will result in different wing deflection with the flight speed. Large wing deflections may lead to insufficient lift force. A calculation represented in Figure D.4 suggests that a desired deflection of the wing to produce the lift force (e.g., flat shape) can be achieved by biasing pre-stretch and applied voltage of the DEAs on upper and bottom sides. Figure D.5 shows a proposed control system for the MAV, and Figure D.6 is a set of other conceptual schematics.

*The schematic on the right side is adopted from: https://commons.wikimedia.org/wiki/File:Birdwing.svg.

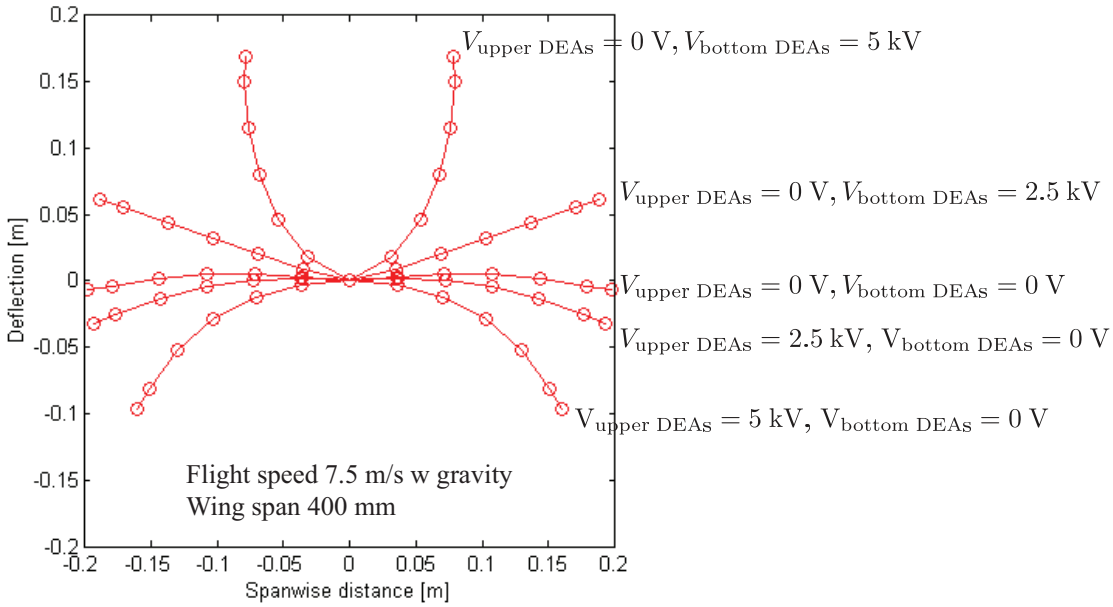

Figure D.4 – Wing shape control with biased DEA applied voltage. The DEAs on upper and bottom sides have different pre-stretch so that the wing can sustain a flat shape at no applied voltage, against a fixed flight speed.

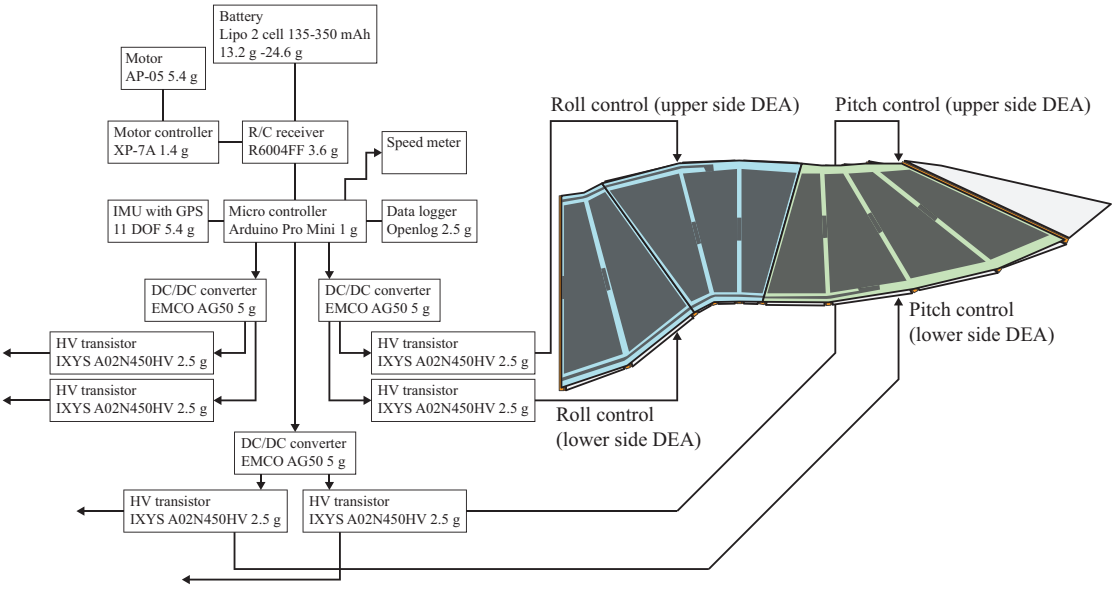

Figure D.5 – Control system of the MAV. A set of DC/DC converters and high-voltage transistors activate the active wing regions separately.

Figure D.6 – Other conceptual schematics of foldable MAV. The body has a role to protect the motor and hold the wing in the folded state.

Bibliography

[1] G. Tonietti, R. Schiavi and A. Bicchi, "Design and control of a variable stiffness actuator for safe and fast physical human/robot interaction," in *International Conference on Robotics and Automation*, Barcelona, Spain, April 2005.

[2] J. M. Jani, M. Leary, A. Subic and M. A. Gibson, "A review of shape memory alloy research, applications and opportunities," *Materials and Design*, vol. 56, pp. 1078–1113, 2014.

[3] B. E. Schubert, "Design, fabrication and testing of angled fiber suspension for electrostatic actuators," Ph.D. Thesis, University of California, Berkeley, 2011.

[4] I. Hunter, S. Lafontaine, J. Hollerbach and P. Hunter, "Fast reversible NiTi fibers for use in microrobotics," in *IEEE Micro Electro Mechanical Systems*, Nara, Japan, February 1991.

[5] C. C. Lan and C. H. Fan, "An accurate self-sensing method for the control of shape memory alloy actuated flexures," *Sens. Actuators A: Phys.*, vol. 163, no. 1, pp. 323-332, 2010.

[6] D. E. Hodgson, M. H. Wu, R. J. Biermann, "Shape memory alloys," *ASM Handbook, Volume 2: Properties and Selection: Nonferrous Alloys and Special-Purpose Materials*, pp. 897-902, 1990.

[7] S. Kim, E. Hawkes, K. Choy, M. Joldaz, J. Foleyz and R. Wood, "Micro artificial muscle fiber using NiTi spring for soft robotics," in *IEEE/RSJ International Conference on Intelligent Robots and Systems*, St. Louis, MO, USA, October 2009.

[8] J. Ayers and J. Witting, "Biomimetic approaches to the control of underwater walking machines," *Philosophical Transactions of the Royal Society of London. Series A*, vol. 365, no. 1850, pp. 273–295, 2007.

[9] M. Kovač, A. Guignard, J.-D. Nicoud, J.-C. Zufferey and D. Floreano, "A 1.5g sma-actuated microglider looking for the light," in *IEEE International Conference on Robotics and Automation*, Rome, Italy, April 2007.

[10] H.-T. Lin, G. G. Leisk and B. Trimmer, "GoQBot: a caterpillar-inspired soft-bodied rolling robot," *Bioinspiration & Biomimetics*, vol. 6, no. 2, pp. 026007-1-026007-14, 2011.

[11] S. Seok, C. D. Onal, K.-J. Cho, R. J. Wood, D. Rus and S. Kim, "Meshworm: a peristaltic soft robot with antagonistic nickel titanium coil actuators," *IEEE/ASME Transactions on Mechatronics*, vol. 18, no. 5, pp. 1485-1497, 2013.

[12] K.-J. Cho, E. Hawkes, C. Quinn and R. J. Wood, "Design, fabrication and analysis of a body-caudal fin propulsion system for a microrobotic fish," in *IEEE International Conference on Robotics and Automation*, Pasadena, CA, USA, May 2008.

[13] C. Laschi, M. Cianchetti, B. Mazzolai, L. Margheri, M. Follador and P. Dario, "Soft robot arm inspired by the octopus," *Advanced Robotics*, vol. 26, no. 7, pp. 709-727, 2012.

[14] A. Villanueva, C. Smith and S. Priya, "A biomimetic robotic jellyfish (Robojelly) actuated by shape memory alloy composite actuators," *Bioinspiration & Biomimetics*, vol. 6, no. 3, pp. 036004-1-036004-16, 2011.

[15] Z. Wang, Y. Wang, J. Li and G. Hang, "A micro biomimetic manta ray robot fish actuated by SMA," in *IEEE International Conference on Robotics and Biomimetics*, Guilin, China, December 2009.

[16] H.-J. Kim, S.-H. Song and S.-H. Ahn, "A turtle-like swimming robot using a smart soft composite (SSC) structure," *Smart Materials and Structures*, vol. 22, no. 1, pp. 014007-1-014007-11, 2013.

[17] J. Colorado, A. Barrientos, C. Rossi, J. W. Bahlman and K. S. Breuer, "Biomechanics of smart wings in a bat robot: morphing wings using SMA actuators," *Bioinspiration & Biomimetics*, vol. 7, no. 3, pp. 036006-1-036006-16, 2012.

[18] Y. Matsuyama and S. Hirai, "Analysis of circular robot jumping by body deformation," in *IEEE International Conference on Robotics and Automation*, Rome, Italy, April 2007.

[19] J.-S. Koh, E. Yang, G.-P. Jung, S.-P. Jung, J. H. Son, S.-I. Lee, P. G. Jablonski, R. J. Wood, H.-Y. Kim and K.-J. Cho, "Jumping on water: surface tension–dominated jumping of water striders and robotic insects," *Science*, vol. 349, no. 6247, pp. 517-521, 2015.

[20] K. Ikuta, M. Tsukumoto and S. Hirose, "Shape memory alloy servo actuator system with electric resistance feedback and application for active endoscope," in *IEEE International Conference on Robotics and Automation*, Philadelphia, PA, USA, April 1988.

[21] A. D. Price, A. Jnifene and H. E. Naguib, "Design and control of a shape memory alloy based dexterous robot hand," *Smart Materials and Structures*, vol. 16, no. 4, pp. 1401–1414, 2007.

[22] C. Jo, D. Pugal, I.-K. Oh, K. J. Kim and K. Asaka, "Recent advances in ionic polymer–metal composite actuators and their modeling and applications," *Progress in Polymer Science*, vol. 38, no. 7, pp. 1037–1066, 2013.

[23] J. Barramba, J. Silva and P. J. Costa Branco, "Evaluation of dielectric gel coating for encapsulation of ionic polymer–metal composite (IPMC) actuators," *Sensors and Actuators A: Physical*, vol. 140, no. 2, pp. 232–238, 2007.

[24] A. Punning, M. Kruusmaa and A. Aabloo, "A self-sensing ion conducting polymer metal composite (IPMC) actuator," *Sensors and Actuators A: Physical*, vol. 136, no. 2, pp. 656–664, 2006.

[25] M. Aureli, C. Prince, M. Porfiri and S. D. Peterson, "Energy harvesting from base excitation of ionic polymer metal composites in fluid environments," *Smart Materials and Structures*, vol. 19, no. 1, pp. 015003-1-015003-15, 2010.

[26] S. Nemat-Nasser and Y. Wu, "Comparative experimental study of ionic polymer-metal composites with different backbone ionomers and in various cation forms," *Journal of Applied Physics*, vol. 93, no. 9, pp. 5255-5267, 2003.

[27] N. Kamamichi, M. Yamakita, K. Asaka and Z.-W. Luo, "A snake-like swimming robot using IPMC actuator/sensor," in *IEEE International Conference on Robotics and Automation*, Orlando, FL, USA, May 2006.

[28] Z. Chen, S. Shatara and X. Tan, "Modeling of biomimetic robotic fish propelled by an ionic polymer–metal composite caudal fin," *IEEE/ASME Transactions on Mechatronics*, vol. 15, no. 3, pp. 448-459, 2010.

[29] J. J. Hubbard, M. Fleming, V. Palmre, D. Pugal, K. J. Kim and K. K. Leang, "Monolithic ipmc fins for propulsion and maneuvering in bioinspired underwater robotics," *IEEE Journal of Oceanic Engineering*, vol. 39, no. 3, pp. 540-551, 2014.

[30] Z. Chen, T. I. Um and H. Bart-Smith, "A novel fabrication of ionic polymer–metal composite membrane actuator capable of 3-dimensional kinematic motions," *Sensors and Actuators A: Physical*, vol. 168, no. 1, pp. 131–139, 2011.

[31] L. Shi, S. Guo, S. Mao, C. Yue, M. Li and K. Asaka, "Development of an amphibious turtle-inspired spherical mother robot," *Journal of Bionic Engineering*, vol. 10, no. 4, pp. 446–455, 2013.

[32] S.-W. Yeom and I.-K. Oh, "A biomimetic jellyfish robot based on ionic polymer metal composite actuators," *Smart Materials and Structures*, vol. 18, no. 8, pp. 085002-1-085002-10, 2009.

[33] J. Najem, S. A. Sarles, B. Akle and D. J. Leo, "Biomimetic jellyfish-inspired underwater vehicle actuated by ionic polymer metal composite actuators," *Smart Materials and Structures*, vol. 21, no. 9, pp. 094026-1-094026-11, 2012.

[34] P. Arena, C. Bonomo, L. Fortuna, M. Frasca, and S. Graziani, "Design and control of an IPMC wormlike robot," *IEEE Transactions on Systems, Man, and Cybernetics, Part B: Cybernetics*, vol. 36, no. 5, pp. 1044-1052, 2006.

[35] A. Firouzeh, M. Ozmaeian, A. Alasty and A. Iraji zad, "An IPMC-made deformable-ring-like robot," vol. 21, no. 6, pp. 065011-1-065011-11, 2012.

[36] R. K. Jain, S. Majumder and A. Dutta, "SCARA based peg-in-hole assembly using compliant IPMC micro gripper ," *Robotics and Autonomous Systems*, vol. 61, no. 3, pp. 297–311, 2013.

[37] I. A. Khan, R. K. Jain and M. Naushad, "Development of sulfonated poly(vinyl alcohol)/polpyrrole based ionic polymer metal composite (IPMC) actuator and its characterization," *Smart Materials and Structures*, vol. 24, no. 9, 095003-1-095003-14, 2015.

[38] F. Daerden and D. Lefeber, "Pneumatic artificial muscles: actuators for robotics and automation," *European Journal of Mechanical Engineering*, vol. 47, no. 1, pp. 11-21, 2002.

[39] K. C. Galloway, P. Polygerinos, C. J. Walsh and R. J. Wood, "Mechanically programmable bend radius for fiber-reinforced soft actuators," in *International Conference on Advanced Robotics*, Montevideo, Uruguay, November 2013.

[40] B. Mosadegh, P. Polygerinos, C. Keplinger, S. Wennstedt, R. F. Shepherd, U. Gupta, J. Shim, K. Bertoldi, C. J. Walsh and G. M. Whitesides, "Pneumatic networks for soft robotics that actuate rapidly," *Advanced Functional Materials*, vol. 24, no. 15 pp. 2163–2170, 2014.

[41] S. A. Morin, R. F. Shepherd, S. W. Kwok, A. A. Stokes, A. Nemiroski and G. M. Whitesides, "Camouflage and display for soft machines," *Science*, vol. 337, no. 6096, pp. 828-832, 2012.

[42] R. F. Shepherd, A. A. Stokes, R. M. D. Nunes and G. M. Whitesides, "Soft machines that are resistant to puncture and that self seal," *Advanced Materials*, vol. 25, no. 46, pp. 6709–6713, 2013.

[43] F. Daerden and D. Lefeber, "Pneumatic artificial muscles: actuators for robotics and automation," *European Journal of Mechanical Engineering*, vol. 47, no. 1, pp. 11-21, 2002.

[44] M. T. Tolley, R. F. Shepherd, B. Mosadegh, K. C. Galloway, M. Wehner, M. Karpelson, R. J. Wood and G. M. Whitesides, "A resilient, untethered soft robot," *Soft Robotics*, vol. 1, no. 3, pp. 213-223, 2014.

[45] C. D. Onal, X. Chen, G. M. Whitesides and D. Rus, "Soft mobile robots with on-board chemical pressure generation," in *International Symposium on Robotics Research*, Flagstaff, AZ, USA, September 2011.

[46] A. D. Marchese, C. D. Onal and D. Rus, "Autonomous soft robotic fish capable of escape maneuvers using fluidic elastomer actuators," *Soft Robotics*, vol. 1, no. 1, pp. 75-87, 2014.

[47] A. D. Marchese, K. Komorowski, C. D. Onal and D. Rus, "Design and control of a soft and continuously deformable 2D robotic manipulation system," in *IEEE International Conference on Robotics and Automation*, Hong Kong, China, June 2014.

[48] R. V. Martinez, J. L. Branch, C. R. Fish, L. Jin, R. F. Shepherd, R. M. D. Nunes, Z. Suo and G. M. Whitesides, "Robotic tentacles with three-dimensional mobility based on flexible elastomers," *Advanced Materials*, vol. 25, no. 2, pp. 205–212, 2013.

[49] P. Polygerinos, Z. Wang, K. C. Galloway, R. J. Wood, C. J. Walsh, "Soft robotic glove for combined assistance and at-home rehabilitation," *Robotics and Autonomous Systems*, vol. 73, pp. 135–143, 2015.

[50] T. A. Gisby, E. P. Calius, S. Xie and I. A. Anderson, "An adaptive control method for dielectric elastomer devices," in *Proc. SPIE*, San Diego, USA, March 2008.

[51] B. M. O'Brien, E. P. Calius, T. Inamura, S. Q. Xie and I. A. Anderson, "Dielectric elastomer switches for smart artificial muscles," *Applied Physics A*, vol. 100, no. 2, pp. 385-389, 2010.

[52] S. J. A. Koh, C. Keplinger, T. Li, S. Bauer and Z. Suo, "Dielectric elastomer generators: how much energy can be converted?," *IEEE/ASME Transactions on Mechatronics*, vol. 16, no. 1, pp. 33-41, 2011.

[53] S. Hunt, T. G. McKay and I. A. Anderson, "A self-healing dielectric elastomer actuator," *Applied Physics Letters*, vol. 104, no. 11, pp. 113701-1-113701-3, 2014.

[54] SEPIA Displays, "Full-color single pixel, real time operation, front lit, 12 mm wide," Available: https://www.youtube.com/watch?v=9dZpNEBqf7g [Accessed September 2015].

[55] EMCO High Voltage Corp., "EMCO proportional voltage products," Available: http://www.emcohighvoltage.com/proportional-power-supply.php [Accessed September 2015].

[56] F. Carpi, S. Bauer and D. D. Rossi, "Stretching dielectric elastomer performance," *Science*, vol. 330, no. 6012, pp. 1759-1761, 2010.

[57] R. Hentschke, *Thermodynamics: For Physicists, Chemists and Materials Scientists*, Berlin, Heidelberg: Springer-Verlag, 2014.

[58] B. Kussmaul, S. Risse, G. Kofod, R. Waché, M. Wegener, D. N. McCarthy, H. Krüger and R. Gerhard, "Enhancement of dielectric permittivity and electromechanical response in silicone elastomers: molecular grafting of organic dipoles to the macromolecular network," *Advanced Functional Materials*, vol. 21, no. 23, pp. 4589–4594, 2011.

[59] F. B. Madsen, A. E. Daugaard, S. Hvilsted, M. Y. Benslimane and A. L. Skov, "Dipolar cross-linkers for PDMS networks with enhanced dielectric permittivity and low dielectric loss," *Smart Materials and Structures*, vol. 22, no. 10, pp. 104002-1-104002-11, 2013.

[60] F. B. Madsen, L. Yu, A. E. Daugaard, S. Hvilsted and A. L. Skov, "Silicone elastomers with high dielectric permittivity and high dielectric breakdown strength based on dipolar copolymers," *Polymer*, vol. 55, no. 24, pp. 6212–6219, 2014.

[61] M. Molberg, D. Crespy, P. Rupper, F. Nüesch, J.-A. E. Månson, C. Löwe and D. M. Opris, "High breakdown field dielectric elastomer actuators using encapsulated polyaniline as high dielectric constant filler," *Advanced Functional Materials*, vol. 20, no. 19, pp. 3280–3291, 2010.

[62] L. Yu, F. B. Madsen, S. Hvilsted and A. L. Skov, "Dielectric elastomers, with very high dielectric permittivity, based on silicone and ionic interpenetrating networks," *RSC Advances*, vol. 5, no. 61, pp. 49739-49747, 2015.

[63] Y. Liu, L. Liu, Z. Zhang and J. Leng, "Dielectric elastomer film actuators: characterization, experiment and analysis*," *Smart Materials and Structures*, vol. 18, no. 9, pp. 095024-1-095024-10, 2009.

[64] G. Gallone, F. Galantini and F. Carpi, "Perspectives for new dielectric elastomers with improved electromechanical actuation performance: composites versus blends," *Polymer Science & Technology General*, vol. 59, no. 3, pp. 400–406, 2010.

[65] G. Ouyang, K. Wang and X. Y. Chen, "TiO_2 nanoparticles modified polydimethylsiloxane with fast response time and increased dielectric constant," *Journal of Micromechanics and Microengineering*, vol. 22, no. 7, pp. 074002-1-074002-9, 2012.

[66] H. Stoyanov, P. Brochu, X. Niu, E. D. Gaspera and Q. Pei, "Dielectric elastomer transducers with enhanced force output and work density," *Applied Physics Letters*, vol. 100, no. 26, pp. 262902-1-262902-3, 2012.

[67] H. Liu, L. Zhang, D. Yang, Y. Yu, L. Yao and M. Tian, "Mechanical, dielectric, and actuated strain of silicone elastomer filled with various types of TiO_2," *Soft Materials*, vol. 11, no.3, pp. 363-370, 2013.

[68] S. Vudayagiri, S. Zakaria, L. Yu, S. S. Hassouneh, M. Benslimane and A. L. Skov, "High breakdown-strength composites from liquid silicone rubbers," *Smart Materials and Structures*, vol. 23, no. 10, pp. 105017-1-105017-15, 2014.

[69] S. Rosset, "Metal ion implated electrodes for dielectric elastomer actuators," Ph.D. Thesis, École Polytechnique Fédérale de Lausanne, 2009.

[70] J.-S. Plante and S. Dubowsky, "Large-scale failure modes of dielectric elastomer actuators," *International Journal of Solids and Structures*, vol. 43, no. 25-26, pp. 7727–7751, 2006.

[71] X. Zhao, W. Hong and Z. Suo, "Electromechanical hysteresis and coexistent states in dielectric elastomers," *Physical Review B*, vol. 76, no. 13, pp. 134113-1-134113-9, 2007.

[72] R. W. Ogden, "Large deformation isotropic elasticity – on the correlation of theory and experiment for incompressible rubberlike solids," *Proceedings of the Royal Society of London. Series A*, vol. 326, no. 1567, pp. 565–584, 1972.

[73] M. Mooney, "A theory of large elastic deformation," *Journal of Applied Physics*, vol. 11, no. 9, pp. 582-592, 1940.

[74] R. S. Rivlin, "Large elastic deformations of isotropic materials. IV. Further developments of the general theory," *Philosophical Transactions of the Royal Society of London. Series A*, vol. 241, no. 835, pp. 379-397, 1948.

[75] E. M. Arruda and M. C. Boyce, "A three-dimensional model for the large stretch behavior of rubber elastic materials," *Journal of the Mechanics and Physics of Solids*, vol. 41, no. 2, pp. 389–412, 1993.

[76] A. N. Gent, "A new constitutive relation for rubber," *Rubber Chemistry and Technology*, vol. 69, no. 1, pp. 59-61, 1996.

[77] G. Marckmann and E. Verron, "Comparison of hyperelastic models for rubber-like materials," *Rubber Chemistry and Technology*, vol. 79, no. 5, pp. 835-858, 2006.

[78] B. Kim, S. B. Lee, J. Lee, S. Cho, H. Park, S. Yeom and S. Han. Park, "A comparison among Neo-Hookean model, Mooney-Rivlin model, and Ogden model for chloroprene rubber," *International Journal of Precision Engineering and Manufacturing*, vol. 13, no. 5, pp. 759-764, 2012.

[79] J. Leng, L. Liu, Y. Liu, K. Yu and S. Sun, "Electromechanical stability of dielectric elastomer," *Applied Physics Letters*, vol. 94, no. 21, pp. 211901-1-211901-3, 2009.

[80] J. Zhu, H. Stoyanov, G. Kofod and Z. Suo, "Large deformation and electromechanical instability of a dielectric elastomer tube actuator," *Journal of Applied Physics*, vol. 108, no. 7, pp. 074113-1-074113-6, 2010.

[81] R. Pelrine, R. Kornbluh, J. Joseph, R. Heydt, Q. Pei and S. Chiba, "High-field deformation of elastomeric dielectrics for actuators," *Materials Science and Engineering: C*, vol. 11, no. 2, pp. 89–100, 2000.

[82] G. Kofod, "Dielectric elastomer actuators," Ph.D. Thesis, The Technical University of Denmark, 2001.

[83] M. Wissler and E. Mazza, "Modeling of a pre-strained circular actuator made of dielectric elastomers," *Sensors and Actuators A: Physical*, vol. 120, no. 1, pp. 184–192, 2005.

[84] G. Kofod, "The static actuation of dielectric elastomer actuators: how does pre-stretch improve actuation?," *Journal of Physics D: Applied Physics*, vol. 41, no. 21, pp. 215405-1-215405-11, 2008.

[85] M. Wissler and E. Mazza, "Modeling and simulation of dielectric elastomer actuators," *Smart Materials and Structures*, vol. 14, no. 6, pp. 1396-1402, 2005.

[86] M. Wissler and E. Mazza, "Electromechanical coupling in dielectric elastomer actuators," *Sensors and Actuators A: Physical*, vol. 138, no. 2, pp. 384–393, 2007.

[87] S. J. A. Koh, T. Li, J. Zhou, X. Zhao, W. Hong, J. Zhu and Z. Suo, "Mechanisms of large actuation strain in dielectric elastomers," *Journal of Polymer Science Part B: Polymer Physics*, vol. 49, no. 7, pp. 504–515, 2011.

[88] T. Lu, J. Huang, C. Jordi, G. Kovacs, R. Huang, D. R. Clarke and Z. Suo, "Dielectric elastomer actuators under equal-biaxial forces, uniaxial forces, and uniaxial constraint of stiff fibers," *Soft Matter*, vol. 8, no. 22, pp. 6167–6173, 2012.

[89] S. Rosset, O. A. Araromi, J. Shintake and H. Shea, "Model and design of dielectric elastomer minimum energy structures," *Smart Materials and Structures*, vol. 23, no. 8, pp. 085021-1-085021-12, 2014.

[90] G. Kofod, P. Sommer-larsen, R. Kornbluh and R. Pelrine, "Actuation response of polyacrylate dielectric elastomers,", *Journal of Intelligent Material Systems and Structures*, vol. 14, no. 12, pp. 787-793, 2003.

[91] X. Zhao and Z. Suo, "Theory of dielectric elastomers capable of giant deformation of actuation," *Physical Review Letters*, vol. 104, no. 17, pp. 178302-1-178302-4, 2010.

[92] S. Akbari, S. Rosset and H. Shea, "Improved electromechanical behavior in castable dielectric elastomer actuators ," *Applied Physics Letters*, vol. 102, no. 7, pp. 071906-1-071906-5, 2013.

[93] R. Palakodeti and M. R. Kessler, "Influence of frequency and prestrain on the mechanical efficiency of dielectric electroactive polymer actuators," *Materials Letters*, vol. 60, no. 29-30, pp. 3437–3440, 2006.

[94] H. R. Choi, K. Jung, N. H. Chuc, M. Jung, I. Koo, J. Koo, J. Lee, J. Lee, J. Nam, M. Cho and Y. Lee, "Effects of prestrain on behavior of dielectric elastomer actuator," in *Proc. SPIE*, San Diego, CA, USA, March 2005.

[95] S. Rosset, O. A. Araromi and H. Shea, "Maximizing the displacement of compact planar dielectric elastomer actuators," *Extreme Mechanics Letters*, vol. 3, pp. 72–81, 2015.

[96] S. Akbari, H. Shea, "Arrays of 100 μm × 100 μm dielectric elastomer actuators to strain the single cells," *Procedia Engineering*, vol. 25, pp. 693–696, 2011.

[97] Z. Suo and J. Zhu, "Dielectric elastomers of interpenetrating networks," *Applied Physics Letters*, vol. 95, no. 23, pp. 232909-1-232909-3, 2009.

[98] X. Zhao, W. Hong and Z. Suo, "Electromechanical hysteresis and coexistent states in dielectric elastomers," *Physical Review B*, vol. 76, no. 13, pp. 074113-1-074113-9 2007.

[99] J. D. W. Madden, N. A. Vandesteeg, P. A. Anquetil, P. G. A. Madden and A. Takshi, "Artificial muscle technology: physical principles and naval prospects," *IEEE Journal of Oceanic Engineering*, vol. 29, no. 3, pp. 706-728, 2004.

[100] S. Michel, X. Q. Zhang, M. Wissler, C. Löwe and G. Kovacs, "A comparison between silicone and acrylic elastomers as dielectric materials in electroactive polymer actuators," *Polymer International*, vol. 59, no. 3, pp. 391–399, 2010.

[101] L. Maffli, S. Rosset, M. Ghilardi, F. Carpi and H. Shea, "Ultrafast all-polymer electrically tunable silicone lenses," *Advanced Functional Materials*, vol. 25, no. 11, pp. 1656–1665, 2015.

[102] F. Carpi, D. D. Rossi, R. Kornbluh, R. Pelrine and P. Sommer-Larsen, *Dielectric Elastomers as Electromechanical Transducers: Fundamentals, Materials, Devices, Models and Applications of an Emerging Electroactive Polymer Technology*, Amsterdam: Elsevier, 2008.

[103] S. Rosset, M. Niklaus, P. Dubois, M. Dadras and H. Shea, "Mechanical properties of electroactive polymer microactuators with ion-implanted electrodes," in *Proc. SPIE*, San Diego, CA, USA, March 2007.

[104] Z. Wang, A. A. Volinsky and N. D. Gallant, "Crosslinking effect on polydimethylsiloxane elastic modulus measured by custom-built compression instrument," *Journal of Applied Polymer Science*, vol. 131, no. 22, pp. 41050-1-41050-4, 2014.

[105] C. Keplinger, M. Kaltenbrunner, N. Arnold and S. Bauer, "Röntgen's electrode-free elastomer actuators without electromechanical pull-in instability," *Proceedings of the National Academy of Sciences of the United States of America*, vol. 107, no. 10, pp. 4505–4510, 2010.

[106] S. Rosset and H. Shea, "Flexible and stretchable electrodes for dielectric elastomer actuators," *Applied Physics A*, vol. 110, no. 2, pp. 281-307, 2013.

[107] S. Rosset, M. Niklaus, P. Dubois and H. Shea, "Metal ion implantation for the fabrication of stretchable electrodes on elastomers," *Advanced Functional Materials*, vol. 19, no. 3, pp. 470–478, 2009.

[108] S. P. Lacour, J. Jones, Z. Suo and S. Wagner, "Design and performance of thin metal film interconnects for skin-like electronic circuit," *IEEE Electron Device Letters*, vol. 25, no. 4, pp. 179-181, 2004.

[109] M. Benslimane, P. Gravesen and P. Sommer-Larsen, "Mechanical properties of dielectric elastomer actuators with smart metallic compliant electrodes," in *Proc. SPIE*, San Diego, CA, USA, March 2002.

[110] H.-E. Kiil and M. Benslimane, "Scalable industrial manufacturing of DEAP," in *Proc. SPIE*, San Diego, CA, USA, March 2009.

[111] M. Y. Benslimane, H.-E. Kiil and M. J. Tryson, "Dielectric electro-active polymer push actuators: performance and challenges," *Polymer International*, vol. 59, no. 3, pp. 415-421, 2010.

[112] K. Wegner, P. Piseri, H. Vahedi Tafreshi and P. Milani, "Cluster beam deposition: a tool for nanoscale science and technology," *Journal of Physics D: Applied Physics*, vol. 39, no. 22, pp. R439–R459, 2006.

[113] N. Pekas, Q. Zhang and D. Juncker, "Electrostatic actuator with liquid metal–elastomer compliant electrodes used for on-chip microvalving," *Journal of Micromechanics and Microengineering*, vol. 22, no. 9, pp. 097001-1-097001-6, 2012.

[114] L. R. Finkenauer and C. Majidi, "Complaint liquid metal electrodes for dielectric elastomer actuators," in *Proc. SPIE*, San Diego, CA, USA, March 2014.

[115] W. Yuan, L. Hu, Z. Yu, T. Lam, J. Biggs, S. M. Ha, D. Xi, B. Chen, M. K. Senesky, G. Grüner and Qibing Pei, "Fault-tolerant dielectric elastomer actuators using single-walled carbon nanotube electrodes," *Advanced Materials*, vol. 20, no. 3, pp. 621–625, 2008.

[116] E. Cakmak, X. Fang, O. Yildiz, P. D. Bradford and T. K. Ghosh, "Carbon nanotube sheet electrodes for anisotropic actuation of dielectric elastomers," *Carbon*, vol. 89, pp. 113–120, 2015.

[117] J. Zang, S. Ryu, N. Pugno, Q. Wang, Q. Tu, M. J. Buehler and X. Zhao, "Multifunctionality and control of the crumpling and unfolding of large-area graphene," *Nature Materials*, vol. 12, no. 4, pp. 321–325, 2013.

[118] B. O'Brien, J. Thod, I. Anderson,E. Calius, E. Haemmerle and S. Xie, "Integrated extension sensor based on resistance and voltage measurement for a dielectric elastomer," in *Proc. SPIE*, San Diego, CA, USA, March 2007.

[119] B. O'Brien, E. Calius, T. Inamura, S. Xie and I. Anderson, "Dielectric elastomer switches for smart artificial muscles," *Applied Physics A*, vol. 100, no. 2, pp. 385-389, 2010.

[120] J. Huang, T. Li, C. C. Foo, J. Zhu, D. R. Clarke and Z. Suo, "Giant, voltage-actuated deformation of a dielectric elastomer under dead load," *Applied Physics Letters*, vol. 100, no. 4, pp. 041911-1-041911-4, 2012.

[121] R. C. Bansal, M.-J. Wang and J.-B. Donnet, *Carbon Black: Science and Technology*, 2nd ed. Boca Raton, FL: CRC Press, 1993.

[122] K. Yurekli, R. Krishnamoorti, M. F. Tse, K. O. McElrath, A. H. Tsou and H.-C. Wang, "Structure and dynamics of carbon black-filled elastomers," *Journal of Polymer Science Part B: Polymer Physics*, vol. 39, no. 2, pp. 256–275, 2001.

[123] M. Bozlar, C. Punckt, S. Korkut, J. Zhu, C. C. Foo, Z. Suo and I. A. Aksay, "Dielectric elastomer actuators with elastomeric electrodes," *Applied Physics Letters*, vol. 101, no. 9, pp. 091907-1-091907-5, 2012.

[124] S. Araby, Q. Meng, L. Zhang, I. Zaman, P. Majewski and J. Ma, "Elastomeric composites based on carbon nanomaterials," *Nanotechnology*, vol. 26, no. 11, pp. 112001-1-112001-23, 2015.

[125] S. Rosset, S. Araromi, S. Schlatter and H. Shea, "Fabrication process of silicone-based dielectric elastomer actuators," *Journal of Visualized Experiments*, DOI:10.3791/53423.

[126] L. Maffli, "Fluidically-coupled dielectric elastomer actuator structures for tunable optics and microfluidics," Ph.D. Thesis, École Polytechnique Fédérale de Lausanne, 2014.

[127] F. Carpi, G. Frediani, C. Gerboni, J. Gemignani and D. D. Rossi, "Enabling variable-stiffness hand rehabilitation orthoses with dielectric elastomer transducers," *Medical Engineering & Physics*, vol. 36, no. 2, pp. 205–211, 2014.

[128] R. Kornbluh, R. Pelrine, Q. Pei, R. Heydt, S. Stanford, S. Oh and J. Eckerle, "Electroelastomers: applications of dielectric elastomer transducers for actuation, generation and smart structures," in *Proc. SPIE*, San Diego, CA, USA, March 2002.

[129] A. Rajamani, M. D. Grissom, C. D. Rahn and Q. Zhang, "Wound roll dielectric elastomer actuators: fabrication, analysis, and experiments," *IEEE/ASME Transactions on Mechatronics*, vol. 13, no. 1, pp. 117-124, 2008.

[130] M. Y. Benslimane, H.-E. Kiil and M. J. Tryson, "Dielectric electro-active polymer push actuators: performance and challenges," *Polymer International*, vol. 59, no. 3, pp. 415–421, 2010.

[131] Q. Pei, R. Pelrine, S. Stanford, R. Kornbluh, M. Rosenthal, K. Meijer and R. Full, "Multifunctional electroelastomer rolls and their application for biomimetic walking robots," in *Proc. SPIE*, San Diego, CA, USA, March 2002.

[132] S. Arora, T. Ghosh and J. Muth, "Dielectric elastomer based prototype fiber actuators," *Sensors and Actuators A: Physical*, vol. 136, no. 1, pp. 321-328, 2007.

[133] C. G. Cameron, J. P.Szabo, S. Johnstone, J. Massey and J. Leidner, "Linear actuation in coextruded dielectric elastomer tubes," *Sensors and Actuators A: Physical*, vol. 147, no. 1, pp. 286–291, 2008.

[134] G. Kofod, H. Stoyanov and R. Gerhard, "Multilayer coaxial fiber dielectric elastomers for actuation and sensing," *Applied Physics A*, vol. 102, no. 3, pp. 577-581, 2011.

[135] J.-S. Plante and S. Dubowsky, "Compliant bistable dielectric elastomer actuators for binary mechatronic systems," in *ASME Mechanism and Robotics Conference*, Long Beach, CA, USA, September 2005.

[136] A. Wingert, M. D. Lichter and S. Dubowsky, "On the design of large degree-of-freedom digital mechatronic devices based on bistable dielectric elastomer actuators," *IEEE/ASME Transactions on Mechatronics*, vol. 11, no. 4, pp. 448-456, 2006.

[137] J.-S. Plante and S. Dubowsky, "On the performance mechanisms of dielectric elastomer actuators," *Sensors and Actuators A: Physical*, vol. 137, no. 1, pp. 96–109, 2007.

[138] H. Choi, K. M. Jung, J. W. Kwak, S. W.Lee, H. Kim, J. W. Jeon and J. D. Nam, "Multiple degree-of-freedom digital soft actuator for robotic applications," in *Proc. SPIE*, San Diego, CA, USA, March 2003.

[139] A. T. Conn and J. Rossiter, "Towards holonomic electro-elastomer actuators with six degrees of freedom," *Smart Materials and Structures*, vol. 21, no.3, pp. 035012-1-035012-9, 2012.

[140] I. A. Anderson, T. C. H. Tse, T. Inamura, B. M. O'Brien, T. McKay and T. Gisby, "A soft and dexterous motor," *Applied Physics Letters*, vol. 98, no. 12, pp. 123704-1-123704-3, 2011.

[141] R. Waché, D. N. McCarthy, S. Risse and G. Kofod, "Rotary motion achieved by new torsional dielectric elastomer actuators design," *IEEE/ASME Transactions on Mechatronics*, vol. 20, no. 2, pp. 975-977, 2015.

[142] Z. Zou, T. Li, S. Qu and H. Yu, "Active shape control and phase coexistence of dielectric elastomer membrane with patterned electrodes," *Journal of Applied Mechanics*, vol. 81, no. 3, pp. 031016-1-031016-4, 2014.

[143] L. An, F. Wang, S. Cheng, T. Lu and T. J. Wang, "Experimental investigation of the electromechanical phase transition in a dielectric elastomer tube," *Smart Materials and Structures*, vol. 24, no. 3, pp. 035006-1- 035006-9, 2015.

[144] C. Zhang, H. Chen, L. Liu and D. Li, "Modelling and characterization of inflated dielectric elastomer actuators with tubular configuration," *Journal of Physics D: Applied Physics*, vol. 48, no. 24, pp. 245502-1-245502-10, 2015.

[145] Z. Yu, W. Yuan, P. Brochu, B. Chen, Z. Liu and Q. Pei, "Large-strain, rigid-to-rigid deformation of bistable electroactive polymers," *Applied Physics Letters*, vol. 95, no. 19, pp. 192904-1-192904-3, 2009.

[146] C. Keplinger, T. Li, R. Baumgartner, Z. Suo and S. Bauer, "Harnessing snap-through instability in soft dielectrics to achieve giant voltage-triggered deformation," *Soft Matter*, vol. 8, no. 2, pp. 285-288, 2012.

[147] S. Ahmadi, M. Gooyers, M. Soleimani and C. Menon, "Fabrication and electromechanical examination of a spherical dielectric elastomer actuator," *Smart Materials and Structures*, vol. 22, no. 11, pp. 115004-1-115004-13, 2013.

[148] Y. Liu, L. Shi, L. Liu, Z. Zhang and J. Leng, "Inflated dielectric elastomer actuator for eyeball's movements: fabrication, analysis and experiments," in *Proc. SPIE*, San Diego, CA, USA, March 2008.

[149] M. Potz, M. Artusi, M. Soleimani, C. Menon, S. Cocuzza and S. Debei, "Rolling dielectric elastomer actuator with bulged cylindrical shape," *Smart Materials and Structures*, vol. 19, no. 12, pp. 127001-1-127001-5, 2010.

[150] F. Carpi, G. Frediani and D. D. Rossi, "Hydrostatically coupled dielectric elastomer actuators," *IEEE/ASME Transactions on Mechatronics*, vol. 15, no. 2, pp. 308-315, 2010.

[151] G.-K. Lau, D. D.-T. Tan and T.-G. La, "Large axial actuation of pre-stretched tubular dielectric elastomer and use of oil encapsulation to enhance dielectric breakdown strength," *Smart Materials and Structures*, vol. 24, no. 4, pp. 045025-1-045025-14, 2015.

[152] T. Li, C. Keplinger, R. Baumgartner, S. Bauer, W. Yang and Z. Suo, "Giant voltage-induced deformation in dielectric elastomers near the verge of snap-through instability," *Journal of the Mechanics and Physics of Solids*, vol. 61, no. 2, pp. 611–628, 2013.

[153] H. Godaba, C. C. Foo, Z. Q. Zhang, B. C. Khoo and J. Zhu, "Giant voltage-induced deformation of a dielectric elastomer under a constant pressure," *Applied Physics Letters*, vol. 105, no. 11, pp. 112901-1-112901-4, 2014.

[154] G. Kofod, M. Paajanen and S. Bauer, "Self-organized minimum-energy structures for dielectric elastomer actuators," *Applied Physics A*, vol. 85, no. 2, pp. 141-143, 2006.

[155] J. Zhao, J. Niu, D. McCoul, Y. Ge, Q. Pei, L. Liu and J. Leng, "Improvement on output torque of dielectric elastomer minimum energy structures," *Applied Physics Letters*, vol. 107, no. 6, pp. 063505-1-063505-5, 2015.

[156] C. H. Nguyen, G. Alici and R. Mutlu, "A compliant translational mechanism based on dielectric elastomer actuators," *Journal of Mechanical Design*, vol. 136, no. 6, pp. 061009-1-061009-9, 2014.

[157] B. O'Brien, T. McKay, E. Calius, S. Xie and I. Anderson, "Finite element modelling of dielectric elastomer minimum energy structures," *Applied Physics A*, vol. 94, no. 3, pp. 507-514, 2009.

[158] P. Lochmatter, G. Kovacs and P. Ermanni, "Design and characterization of shell-like actuators based on soft dielectric electroactive polymers," *Smart Materials and Structures*, vol. 16, no. 4, pp. 1415–1422, 2007.

[159] S.-C. Lin, W.-P. Shih and P.-Z. Chang, "Microstructural dielectric elastomer actuator with uniaxial in-plane contraction," *Journal of Intelligent Material Systems and Structures*, vol. 24, no. 3, pp. 347-356, 2013.

[160] P. Lochmatter, "Development of a shell-like electroactive polymer (EAP) actuator," Ph.D. Thesis, Swiss Federal Institute of Technology in Zurich, 2007.

[161] M. Hodgins, A. York and S. Seelecke, "Modeling and experimental validation of a bistable out-of-plane DEAP actuator system," *Smart Materials and Structures*, vol. 20, no. 9, pp. 094012-1-094012-11, 2011.

[162] T. Li, Z. Zou, G. Mao and S. Qu, "Electromechanical bistable behavior of a novel dielectric elastomer actuator," *Journal of Applied Mechanics*, vol. 81, no. 4, pp. 041019-1-041019-5, 2014.

[163] F. Carpi, A. Migliore, G. Serra and D. D. Rossi, "Helical dielectric elastomer actuators," *Smart Materials and Structures*, vol. 14, no. 6, pp. 1210–1216, 2005.

[164] F. Carpi, C. Salaris and D. D. Rossi, "Folded dielectric elastomer actuators," *Smart Materials and Structures*, vol. 16, no. 2, pp. S300–S305, 2007.

[165] G. Kovacs, L. Düring, S. Michel and G. Terrasi, "Stacked dielectric elastomer actuator for tensile force transmission," *Sensors and Actuators A: Physical*, vol. 155, no. 2, pp. 299–307, 2009.

[166] P. Lotz, M. Matysek and H. F. Schlaak, "Fabrication and application of miniaturized dielectric elastomer stack actuators," *IEEE/ASME Transactions on Mechatronics*, vol. 16, no. 1, pp. 58-66, 2011.

[167] N. H. Chuc, N. H. L. Vuong, D. S. Kim, H. P. Moon, J. C. Koo, Y. K. Lee, J.-D. Nam and H. R. Choi, "Fabrication and control of rectilinear artificial muscle actuator," *IEEE/ASME Transactions on Mechatronics*, vol. 16, no. 1, pp. 167-176, 2011.

[168] G. K. Lau, J. F. L. Goosen, F. van Keulen, P. J. French and P. M. Sarro, "Actuated elastomers with rigid vertical electrodes," *Journal of Micromechanics and Microengineering*, vol. 16, no. 6, pp. S35–S44, 2006.

[169] Q. Wang and X. Zhao, "Creasing-wrinkling transition in elastomer films under electric fields," *Physical Review Letters*, vol. 88, no. 4, pp. 042403-1-042403-6 , 2013.

[170] Q. Wang, G. R. Gossweiler, S. L. Craig and X. Zhao, "Cephalopod-inspired design of electro-mechano-chemically responsive elastomers for on-demand fluorescent patterning," *Nature Communications*, vol. 5, pp. 4899-1-4899-9, 2014.

[171] R. Pelrine, R. D. Kornbluh, Q. Pei, S. Stanford, S. Oh, J. Eckerle, R. J. Full, M. A. Rosenthal and K. Meijer, "Dielectric elastomer artificial muscle actuators: toward biomimetic motion," in *Proc. SPIE*, San Diego, CA, USA, March 2002.

[172] Q. Pei, M. Rosentha, S. Stanford, H. Prahlad and R. Pelrine, "Multiple-degrees-of-freedom electroelastomer roll actuators," *Smart Materials and Structures*, vol. 13, no. 5, pp. N86–N92, 2004.

[173] C. T. Nguyen, H. Phung, H. Jung, U. Kim, T. D. Nguyen, J. Park, H. Moon, J. C. Koo and H. R. Choi, "Printable monolithic hexapod robot driven by soft actuator," in *IEEE International Conference on Robotics and Automation*, Seattle, WA, USA, May 2015.

[174] Q. Pei, R. Pelrine, M. Rosenthal, S. Stanford, H. Prahlad and R. Kornbluh, "Recent progress on electroelastomer artificial muscles and their application for biomimetic robots," in *Proc. SPIE*, San Diego, CA, USA, March 2004.

[175] S. Dubowsky, S. Kesner, J.-S. Plante and P. Boston, "Hopping mobility concept for search and rescue robots," *Industrial Robot: An International Journal*, vol. 35, no. 3, pp. 238 - 245, 2008.

[176] K. Jung, J. C. Koo, J.-do Nam, Y. K. Lee and H. R. Choi, "Artificial annelid robot driven by soft actuators," *Bioinspiration & Biomimetics*, vol. 2, no. 2, pp. S42–S49, 2007.

[177] A. T. Conn, A. D. Hinitt and P. Wang, "Soft segmented inchworm robot with dielectric elastomer muscles," in *Proc. SPIE*, San Diego, CA, USA, March 2014.

[178] S. Shian, K. Bertoldi and D. R. Clarke, "Use of aligned fibers to enhance the performance of dielectric elastomer inchworm robots," in *Proc. SPIE*, San Diego, CA, USA, March 2015.

[179] M. T. Petralia and R. J. Wood, "Fabrication and analysis of dielectric-elastomer minimum-energy structures for highly-deformable soft robotic systems," in *IEEE/RSJ International Conference on Intelligent Robots and Systems*, Taipei, Taiwan, October 2010.

[180] M. Potz, M. Artusi, M. Soleimani, C. Menon, S. Cocuzza and S. Debei, "Rolling dielectric elastomer actuator with bulged cylindrical shape," *Smart Materials and Structures*, vol. 19, no. 12, pp. 127001-1-127001-5, 2010.

[181] M. Artusi, M. Potz, J. Aristizabal, C. Menon, S. Cocuzza and S. Debei, "Electroactive elastomeric actuators for the implementation of a deformable spherical rover," *IEEE/ASME Transactions on Mechatronics*, vol. 16, no. 1, pp. 50-57, 2011.

[182] S. Rosset and H. Shea, "Towards fast, reliable, and manufacturable DEAs: miniaturized motor and Rupert the rolling robot," in *Proc. SPIE*, San Diego, CA, USA, March 2015.

[183] S. Michel, A. Bormann, C. Jordi and E. Fink, "Feasibility studies for a bionic propulsion system of a blimp based on dielectric elastomers," in *Proc. SPIE*, San Diego, CA, USA, March 2008.

[184] C. Jordi, S. Michel and E. Fink, "Fish-like propulsion of an airship with planar membrane dielectric elastomer actuators," *Bioinspiration & Biomimetics*, vol. 5, no. 2, pp. 026007-1-026007-9, 2010.

[185] G.-K. Lau, H.-T. Lim, J.-Y. Teo and Y.-W. Chin, "Lightweight mechanical amplifiers for rolled dielectric elastomer actuators and their integration with bio-inspired wing flappers," *Smart Materials and Structures*, vol. 23, no. 2, pp. 025021-1-025021-13, 2014.

[186] J. Zhao, J. Niu, D. McCoul, Z. Ren and Q. Pei, "Phenomena of nonlinear oscillation and special resonance of a dielectric elastomer minimum energy structure rotary joint," *Applied Physics Letters*, vol. 106, no. 13, pp. 133504-1-133504-4, 2015.

[187] M. R. Hays, J. Morton, B. Dickinson, U. K. Chakravarty and W. S. Oates, "Aerodynamic control of micro air vehicle wings using electroactive membranes", *Journal of Intelligent Material Systems and Structures*, vol. 24, no. 7, pp. 862-878, 2013.

[188] G. Molinari, A. F. Arrieta and P. Ermanni, "Aero-structural optimization of three-dimensional adaptive wings with embedded smart actuators," *AIAA Journal*, vol. 52, no. 9, pp. 1940-1951, 2014.

[189] H. Godaba, W. Ng and J. Zhu, "Development of a soft jellyfish robot based on dielectric elastomer actuators," in *IEEE International Conference on Robotics and Automation, Workshop on Soft Robots*, Hong Kong, China, June 2014.

[190] E. Biddiss and T. Chau, "Dielectric elastomers as actuators for upper limb prosthetics: challenges and opportunities," *Medical Engineering & Physics*, vol. 30, no. 4, pp. 403–418, 2008.

[191] F. Carpi, A. Mannini and D. D. Rossi, "Elastomeric contractile actuators for hand rehabilitation splints," in *Proc. SPIE*, San Diego, CA, USA, March 2008.

[192] S. Pourazadi, S. Ahmadi and C. Menon, "Towards the development of active compression bandages using dielectric elastomer actuators," *Smart Materials and Structures*, vol. 23, no. 6, pp. 065007-1-065007-11, 2014.

[193] F. Carpi and D. D. Rossi, "Bioinspired actuation of the eyeballs of an android robotic face: concept and preliminary investigations," *Bioinspiration & Biomimetics*, vol. 2, no. 2, pp. S50–S63, 2007.

[194] G. Kovacs, P. Lochmatter and M. Wissler, "An arm wrestling robot driven by dielectric elastomer actuators," *Smart Materials and Structures*, vol. 16, no. 2, pp. S306–S317, 2007.

[195] P. Brochu and Q. Pei, "Advances in dielectric elastomers for actuators and artificial muscles," *Macromolecular Rapid Communications*, vol. 31, no. 1, pp. 10–36, 2010.

[196] I. A. Anderson, T. A. Gisby, T. G. McKay, B. M. O'Brien and E. P. Calius, "Multi-functional dielectric elastomer artificial muscles for soft and smart machines," *Journal of Applied Physics*, vol. 112, no. 4, pp. 041101-1-041101-21, 2012.

[197] E. Hawkes, B. An, N. M. Benbernou, H. Tanakaa, S. Kim, E. D. Demaine, D. Rus and R. J. Wood, "Programmable matter by folding," *Proceedings of the National Academy of Sciences of the United States of America*, vol. 107, no. 28, pp. 12441-12445, 2010.

[198] B. An and D. Rus, "Designing and programming self-folding sheets," *Robotics and Autonomous Systems*, vol. 62, no. 7, pp. 976–1001, 2014.

[199] H. Okuzaki, T. Saido, H. Suzuki, Y. Hara and H. Yan, "A biomorphic origami actuator fabricated by folding a conducting paper," *Journal of Physics: Conference Series"*, vol. 127, no. 1, p. 012001-1-012001-7, 2008.

[200] J. K. Paik, E. Hawkes and R. J. Wood, "A novel low-profile shape memory alloy torsional actuator," *Smart Materials and Structures*, vol. 19. no. 12, pp. 125014-1-125014-9, 2010.

[201] R. V. Martinez, C. R. Fish, X. Chen and G. M. Whitesides, "Elastomeric origami: programmable paper-elastomer composites as pneumatic actuators," *Advanced Functional Materials*, vol. 22, no. 7, pp. 1376-1384, 2012.

[202] S. Sareh and J. Rossiter, "Kirigami artificial muscles with complex biologically inspired morphologies," *Smart Materials and Structures*, vol. 22, no. 1, pp. 014004-1-014004-13, 2014.

[203] C. Lekakou, Y. Elsayed, T. Geng and C. M. Saaj, "Skins and sleeves for soft robotics: inspiration from nature and architecture," *Advanced Engineering Materials*, vol. 17, no. 8, pp. 1180–1188, 2015.

[204] R. Niiyama, X. Sun, C. Sung, B. An, D. Rus and S. Kim, "Pouch motors: printable soft actuators integrated with computational design," *Soft Robotics*, vol. 2, no. 2, pp. 59-70, 2015.

[205] S. Ahmed, Z. Ounaies and M. Frecker, "Investigating the performance and properties of dielectric elastomer actuators as a potential means to actuate origami structures," *Smart Materials and Structures*, vol. 23, no. 9, pp. 094003-1-094003-14, 2014.

[206] K. McGough, S. Ahmed, M. Frecker and Z. Ounaies, "Finite element analysis and validation of dielectric elastomer actuators used for active origami," *Smart Materials and Structures*, vol. 23, no. 9, pp. 094002-1-094002-10, 2014.

[207] F. Carpi, C. Salaris and D. D. Rossi, "Folded dielectric elastomer actuators," *Smart Materials and Structures*, vol. 16, no. 2, pp. S300–S305, 2007.

[208] C. T. Nguyen, H. Phung, T. D. Nguyen, C. Lee, U. Kim, D. Lee, H. Moon, J. Koo, J.-D. Nam and H. R. Choi, "A small biomimetic quadruped robot driven by multistacked dielectric elastomer actuators," *Smart Materials and Structures*, vol. 23, no. 6, pp. 065005-1-065005-12, 2014.

[209] S. M. Felton, M. T. Tolley, C. D. Onal, D. Rus and R. J. Wood, "Robot self-assembly by folding: a printed inchworm robot," in *IEEE International Conference on Robotics and Automation*, Karlsruhe, Germany, May 2013.

[210] S. M. Felton, M. T. Tolley, B. Shin, C. D. Onal, E. D. Demaine, D. Rus and R. J. Wood, "Self-folding with shape memory composites," *Soft Matter*, vol. 9, no. 32, pp. 7659-7878, 2013.

[211] S. Fusco, M. S. Sakar, S. Kennedy, C. Peters, S. Pane, D. Mooney and B. J. Nelson, "Self-folding mobile microrobots for biomedical applications," in *IEEE International Conference on Robotics and Automation*, Hong Kong, China, June 2014.

[212] S. Felton, M. T. Tolley, E. Demaine, D. Rus and R. J. Wood, "A method for building self-folding machines," *Science*, Vol. 345, no. 6197, pp. 644-646, 2014.

[213] S. Miyashita, L. Meeker, M. T. Tolley, R. J. Wood and D. Rus, "Self-folding miniature elastic electric devices," *Smart Materials and Structures*, vol. 23, no. 9, pp. 094005-1-094005-9, 2014.

[214] S. Miyashita, S. Guitron, M. Ludersdorfer, C. R. Sung and D. Rus, "An untethered miniature origami robot that self-folds, walks, swims, and degrades," in *IEEE International Conference on Robotics and Automation*, Seattle, WA, USA, May 2015.

[215] J. C. Breger, C. Yoon, R. Xiao, H. R. Kwag, M. O. Wang, J. P. Fisher, T. D. Nguyen and D. H. Gracias, "Self-folding thermo-magnetically responsive soft microgrippers," *Applied Materials & Interfaces*, vol. 7, no. 5, pp. 3398–3405, 2015.

[216] S. Miyashita, I. DiDio, I. Ananthabhotla, B. An, C. R. Sung, S. Arabagi and D. Rus, "Folding angle regulation by curved crease design for self-assembling origami propellers," *Journal of Mechanisms and Robotics*, vol. 7, no. 2, pp. 021013-1-021013-8, 2015.

[217] A. M. Hoover and R. S. Fearing, "Fast scale prototyping for folded millirobots," in *IEEE International Conference on Robotics and Automation*, Pasadena, CA, USA, May 2008.

[218] P. S. Sreetharan, J. P. Whitney, M. D. Strauss and R. J. Wood, "Monolithic fabrication of millimeter-scale machines," *Journal of Micromechanics and Microengineering*, vol. 22, no. 5, pp. 055027-1-055027-6, 2012.

[219] C. D. Onal, R. J. Wood and D. Rus, "An origami-inspired approach to worm robots," *IEEE/ASME Transactions on Mechatronics*, vol. 18, no. 2, pp. 430-438, 2013.

[220] A. Firouzeh and J. Paik, "Robogami: a fully integrated low-profile robotic origami," *Journal of Mechanisms and Robotics*, vol. 7, no. 2, pp. 021009-1-021009-8, 2015.

[221] D. W. Haldane, C. S. Casarez, J. T. Karras, J. Lee, C. Li, A. O. Pullin, E. W. Schaler, D. Yun, H. Ota, A. Javey and R. S. Fearing, "Integrated manufacture of exoskeletons and sensing structures for folded millirobots," *Journal of Mechanisms and Robotics*, vol. 7, no. 2, pp. 021011-1-021011-19, 2015.

[222] C. Sung and D. Rus, "Foldable joints for foldable robots," *Journal of Mechanisms and Robotics* vol. 7, no. 2, pp. 021012-1-021012-13, 2015.

[223] K. Zhang, C. Qiu and J. S. Dai, "Helical kirigami-enabled centimeter-scale worm robot with shape-memory-alloy linear actuators", *Journal of Mechanisms and Robotics*, vol. 7, no. 2, pp. 021014-1-021014-10, 2015.

[224] S. Yim and S. Kim, "Origami-inspired printable tele-micromanipulation system," in *IEEE International Conference on Robotics and Automation*, Seattle, WA, USA, May 2015.

[225] C. D. Onal, M. T. Tolley, R. J. Wood and D. Rus, "Origami-inspired printed robots," *IEEE/ASME Transactions on Mechatronics*, DOI:10.1109/TMECH.2014.2369854.

[226] J. Kim, D.-Y. Lee, S.-R. Kim and K.-J. Cho, "A self-deployable origami structure with locking mechanism induced by buckling effect," in *IEEE International Conference on Robotics and Automation*, Seattle, WA, USA, May 2015.

[227] D.-Y. Lee, J.-S. Kim, J.-J. Park, S.-R. Kim and K.-J. Cho, "Fabrication of origami wheel using pattern embedded fabric and its application to a deformable mobile robot," in *IEEE International Conference on Robotics and Automation*, Hong Kong, China, June 2014.

[228] S. M. Felton, D.-Y. Lee, K.-J. Cho and R. J. Wood, "A passive, origami-inspired, continuously variable transmission," in *IEEE International Conference on Robotics and Automation*, Hong Kong, China, June 2014.

[229] L. Daler, S. Mintchev, C. Stefanini and D. Floreano, "A bioinspired multi-modal flying and walking robot," *Bioinspiration & Biomimetics*, vol. 10, no. 1, pp. 016005-1-016005-14, 2015.

[230] M. Kovač, W. Hraiz, O. Fauria, J.-C. Zufferey and D. Floreano, "The EPFL jumpglider: a hybrid jumping and gliding robot with rigid or folding wings," in *IEEE International Conference on Robotics and Biomimetics*, Phuket, Thailand, December 2011.

[231] S. Mintchev, L. Daler, G. L'Eplattenier, L. Saint-Raymond and D. Floreano, "Foldable and self-deployable pocket sized quadrotor," in *IEEE International Conference on Robotics and Automation*, Seattle, WA, USA, May 2015.

[232] A. K. Stowers and D. Lentink, "Folding in and out: passive morphing in flapping wings," *Bioinspiration & Biomimetics*, vol. 10, no. 2, pp. 025001-1-025001-16, 2015.

[233] R. Pelrine, R. Kornbluh, Q. Pei and J. Joseph, "High-speed electrically actuated elastomers with strain greater than 100%," *Science*, vol. 287, no. 5454, pp. 836-839, 2000.

[234] M. Kollosche, J. Zhu, Z. Suo and G. Kofod, "Complex interplay of nonlinear processes in dielectric elastomers," *Physical Review E*, vol. 85, no. 5, pp. 051801-1-051801-4, 2012.

[235] J. Huang, T. Lu, J. Zhu, D. R. Clarke and Z. Suo, "Large, uni-directional actuation in dielectric elastomers achieved by fiber stiffening," *Applied Physics Letters*, vol. 100, no. 21, pp. 211901-1-211901-4, 2012.

[236] P. Lochmatter and G. Kovacs, "Design and characterization of an active hinge segment based on soft dielectric EAPs," *Sensors and Actuators A: Physical*, vol. 141, no. 2, pp. 577-587, 2008.

[237] P. Chouinard and J. Plante, "Bistable antagonistic dielectric elastomer actuators for binary robotics and mechatronics," *IEEE/ASME Transactions on Mechatronics*, vol. 17, no. 5, pp. 857-865, 2012.

[238] B. Vanderborght, A. Albu-Schaeffer, A. Bicchi, E. Burdet, D. G. Caldwell, R. Carloni, M. Catalano, O. Eiberger, W. Friedl, G. Ganesh, M. Garabini, M. Grebenstein, G. Grioli, S. Haddadin, H. Hoppner, A. Jafari, M. Laffranchi, D. Lefeber, F. Petit, S. Stramigioli, N. Tsagarakis, M. Van Damme, R. Van Ham, L. C. Visser and S. Wolf, "Variable impedance actuators: a review," *Robotics and Autonomous Systems*, vol. 61, no. 12, pp. 1601–1614, 2013.

[239] Z. Suo, "Theory of dielectric elastomers," *Acta Mechanica Solida Sinica*, vol. 23, no. 6, pp. 549-578, 2010.

[240] O. H. Yeoh, "Some forms of the strain energy function for rubber," *Rubber Chemistry and Technology*, vol. 66, no. 5, pp. 754-771, 1993.

[241] J. E. Shigley and C. R. Mischke,*Mechanical Engineering Design, 5th edition*, New York: McGraw-Hill, 1989.

[242] L. L. Howell and A. Midha, "A method for the design of compliant mechanisms with small-length flexural pivots," *Journal of Mechanical Design*, vol. 116, no.1, pp. 280-290, 1994.

[243] R. Kornbluh, R. Peirine, Q. Pei, S. Oh and J. Joseph, "Ultrahigh strain response of field-actuated elastomeric polymers," in *Proc. SPIE*, San Diego, CA, USA, March 2000.

[244] L. Mullins, "Softening of rubber by deformation," *Rubber Chemistry and Technology*, vol. 42, no. 1, pp. 339-362, 1969.

[245] S. Rosset, L. Maffli, S. Houis and H. R. Shea, "An instrument to obtain the correct biaxial hyperelastic parameters of silicones for accurate DEA modelling," in *Proc. SPIE*, San Diego, CA, USA, March 2014.

[246] J. D. Anderson, *Fundamentals of Aerodynamics*, 5th ed., Singapore: McGraw-Hill, 2011.

[247] H. Tennekes, *The Simple Science of Flight: From Insects to Jumbo Jets*, Cambridge, MA: MIT Press, 2009.

[248] S. Leven, "Enabling large-Scale collective systems in outdoor aerial robotics," Ph.D. Thesis, École Polytechnique Fédérale de Lausanne, 2011.

[249] A. Pelletier and T. J. Mueller, "Low Reynolds number aerodynamics of low-aspect-ratio, thin/flat/cambered-plate wings," *Journal of Aircraft*, vol. 37, no. 5, pp. 825-832, 2000.

[250] G. Welch and G. Bishop, "An introduction to the Kalman filter," University of North Carolina at Chapel Hill, Chapel Hill, North Carolina, 1995.

[251] A. Kim and M. Golnaraghit, "A quaternion-based orientation estimation algorithm using an inertial measurement unit," in *Position Location and Navigation Symposium*, Monterey, CA, USA, April 2004.

[252] A. M. Sabatini, "Quaternion-based extended Kalman filter for determining orientation by inertial and magnetic sensing," *IEEE Transactions on Biomedical Engineering*, vol. 53, no. 7, pp. 1346-1356, 2006.

[253] J. Shintake, S. Rosset, B. Schubert, D. Floreano and H. Shea, "A flying robot controlled by artificial muscle," Available: https://www.youtube.com/watch?v=sBo3jb3YPQo [Accessed September 2015].

[254] D. Trivedi, C. D. Rahn, W. M. Kier and I. D. Walker, "Soft robotics: biological inspiration, state of the art, and future research," *Applied Bionics and Biomechanics*, vol. 5, no. 3, pp. 99–117, 2008.

[255] S. Kim, C. Laschi and B. Trimmer, "Soft robotics: a bioinspired evolution in robotics," *Trends in Biotechnology*, vol. 31, no. 5, pp. 287–294, 2013.

[256] D. Rus and M. T. Tolley, "Design, fabrication and control of soft robots," *Nature*, vol. 521, no. 7553, 2015.

[257] R. V. Martinez, A. C. Glavan, C. Keplinger, A. I. Oyetibo and G. M. Whitesides, "Soft actuators and robots that are resistant to mechanical damage," *Advanced Functional Materials*, vol. 24, no. 20, pp. 3003–3010, 2014.

[258] H. Nakai, Y. Kuniyoshi, M. Inaba and H. Inoue, "Metamorphic robot made of low melting point alloy," in *IEEE/RSJ International Conference on Intelligent Robots and System*, Lausanne, Switzerland, October 2002.

[259] E. Steltz, A. Mozeika, N. Rodenberg, E. Brown and H. M. Jaeger, "JSEL: jamming skin enabled locomotion," in *IEEE/RSJ International Conference on Intelligent Robots and Systems*, St. Louis, MO, USA, October 2009.

[260] E. Brown, N. Rodenberg, J. Amend, A. Mozeika, E. Steltz, M. R. Zakin, H. Lipson and H. M. Jaeger, "Universal robotic gripper based on the jamming of granular material," *Proceedings of the National Academy of Sciences*, vol. 107, no. 44, pp. 18809-18814, 2010.

[261] N. G. Cheng, M. B. Lobovsky, S. J. Keating, A. M. Setapen, K. I. Gero, A. E. Hosoi and K. D. Iagnemma, "Design and analysis of a robust, low-cost, highly articulated manipulator enabled by jamming of granular media," in *IEEE International Conference on Robotics and Automation*, St. Paul, MN, USA, May 2012.

[262] V. Wall, R. Deimel and O. Brock, "Selective stiffening of soft actuators based on jamming," in *IEEE International Conference on Robotics and Automation*, Seattle, WA, USA, May 2015.

[263] A. Sadeghi, L. Beccai and B. Mazzolai, "Innovative soft robots based on electro-rheological fluids," in *IEEE/RSJ International Conference on Intelligent Robots and Systems*, Vilamoura, Algarve, Portugal, October 2012.

[264] C. Majidi and R. J. Wood, "Tunable elastic stiffness with microconfined magnetorheological domains at low magnetic field," *Applied Physics Letters*, vol. 97, no. 16, pp. 164104-1-164104-3, 2010.

[265] Y. Chen, J. Sun, Y. Liu and J. Leng, "Variable stiffness property study on shape memory polymer composite tube," *Smart Materials and Structures*, vol. 21, no. 9, pp. 094021-1-094021-9, 2012.

[266] X. Niu, X. Yang, P. Brochu, H. Stoyanov, S. Yun, Z. Yu and Q. Pei. "Bistable large-strain actuation of interpenetrating polymer networks," *Advanced Materials*, vol. 24, no. 48, pp. 6513–6519, 2012.

[267] K. Takashima, K. Sugitani, N. Morimoto, S. Sakaguchi, T. Noritsugu and T. Mukai, "Pneumatic artificial rubber muscle using shape-memory polymer sheet with embedded electrical heating wire," *Smart Materials and Structures*, vol. 23, no. 12, pp. 125005-1-125005-9, 2014.

[268] W. Shan, T. Lu and C. Majidi, "Soft-matter composites with electrically tunable elastic rigidity," *Smart Materials and Structures*, vol. 22, no. 8, pp. 085005-1-085005-8, 2013.

[269] B. Schubert and D. Floreano, "Variable stiffness material based on rigid low-melting-point-alloy-microstructures embedded in soft poly(dimethylsiloxane) (PDMS)," *RSC Advances*, vol. 3, no. 46, pp. 24671-24679, 2013.

[270] J. Shintake, S. Rosset, B. E. Schubert, D. Floreano and H. Shea, "Dielectric elastomer actuators for soft-grasping" in *International Workshop on Soft Robotics and Morphological Computation*, Ascona, Switzerland, July 2013.

[271] J. Wissman, L. Finkenauer, L. Deseri and C. Majidi, "Saddle-like deformation in a dielectric elastomer actuator embedded with liquid-phase gallium-indium electrodes," *Journal of Applied Physics*, vol. 116, no. 14, pp. 144905-1-144905-7, 2014.

[272] G. Kofod, W. Wirges, M. Paajanen and S. Bauer, "Energy minimization for self-organized structure formation and actuation," *Applied Physics Letters*, vol. 90, no. 8, pp. 081916-1-081916-3, 2007.

[273] M. Follador, A. T. Conn, B. Mazzolai and J. Rossiter, "Active-elastic bistable minimum energy structures," *Applied Physics Letters*, vol. 105, no. 14, pp. 141903-1-141903-4, 2014.

[274] S. Araromi, I. Gavrilovich, J. Shintake, S. Rosset and H. Shea, "Towards a deployable satellite gripper based on multisegment dielectric elastomer minimum energy structures," in *Proc. SPIE*, San Diego, CA, USA, March 2014.

[275] J. Shintake, B. Schubert, S. Rosset, H. Shea and D. Floreano, "Variable stiffness actuator for soft robotics using dielectric elastomer and low-melting-point alloy," Available: https://www.youtube.com/watch?v=y1KcaiKpzXU [Accessed September 2015].

[276] C. E. Doyle, J. J. Bird, T. A. Isom, J. C. Kallman, D. F. Bareiss, D. J. Dunlop, R. J. King, J. J. Abbott and M. A. Minor, "An avian-inspired passive mechanism for quadrotor perching," *IEEE/ASME Transactions on Mechatronics*, vol. 18, no. 2, pp. 506-517, 2013.

[277] J. C. Nawroth, H. Lee, A. W. Feinberg, C. M. Ripplinger, M. L. McCain, A. Grosberg, J. O. Dabiri and K. K. Parker, "A tissue-engineered jellyfish with biomimetic propulsion," *Nature Biotechnology*, vol. 30, no. 8, pp. 792–797, 2012.

[278] A. D. Marchese, R. K. Katzschmann and D. Rus, "Whole arm planning for a soft and highly compliant 2d robotic manipulator," in *IEEE/RSJ International Conference on Intelligent Robots and Systems*, Chicago, IL, USA, September 2014.

[279] A. J. Loeve, O. S. van de Ven, J. G. Vogel, P. Breedveld and J. Dankelman, "Vacuum packed particles as flexible endoscope guides with controllable rigidity," *Granular Matter*, vol. 12, no. 6, pp 543-554.

[280] A. Bicchi, "Hands for dexterous manipulation and robust grasping: a difficult road toward simplicity," *IEEE Robotics and Automation*, vol. 16, no. 6, pp. 652 - 662, 2000.

[281] G. J. Monkman, S. Hesse, R. Steinmann and H. Schunk, *Robot Grippers*, Weinheim: Wiley-VCH Verlag GmbH and Co. KGaA, 2006.

[282] G. Carbone, *Grasping in Robotics*, Berlin, Heidelberg: Springer-Verlag, 2013.

[283] R. Pfeifer and J. Bongard, *How the Body Shapes the Way We Think: A New View of Intelligence*, Cambridge, MA: MIT Press, 2006.

[284] S. Hirai, T. Tsuboi and T. Wada, "Robust grasping manipulation of deformable objects," in *IEEE International Symposium on Assembly and Task Planning*, Fukuoka, Japan, May 2001.

[285] A. M. Howard and G. A. Bekey, "Intelligent learning for deformable object manipulation," *Autonomous Robots*, vol. 9, no. 1, pp. 51-58, 2000.

[286] A.-M. Cretu, P. Payeur and E. M. Petriu, "Soft object deformation monitoring and learning for model-based robotic hand manipulation," *IEEE Transactions on Systems, Man, and Cybernetics, Part B: Cybernetics*, vol. 42, no. 3, pp. 740-753, 2012.

[287] H. Lin, F. Guo, F. Wang and Y.-B. Jia, "Picking up a soft 3d object by “feeling” the grip," *The International Journal of Robotics Research*, DOI: 10.1177/0278364914564232.

[288] D. Henrich and H. Wörn, Eds., *Robot Manipulation of Deformable Objects*, Berlin, Heidelberg: Springer-Verlag, 2000.

[289] G. Fantoni, M. Santochi, G. Dini, K. Tracht, B. Scholz-Reiter, J. Fleischer, T. K. Lien, G. Seliger, G. Reinhart, J. Franke, H. N. Hansen and A. Verl, "Grasping devices and methods in automated production processes," *CIRP Annals - Manufacturing Technology*, vol. 63, no. 2, pp. 679-701, 2014.

[290] T. Rienmüller and H. Weissmantel, "A Shape Adaptive gripper finger for robots," in *18th International Symposium on Industrial Robots*, Lausanne, Switzerland, April 1988.

[291] G. L. Kenaley and M. R. Cutkosky, "Electrorheological fluid-based robotic fingers with tactile sensing," in *IEEE International Conference on Robotics and Automation*, Scottsdale, AZ, USA, May 1989.

[292] G. J. Monkman, "Compliant robotic devices and electroadhesion," *Robotica*, vol. 10, no. 2, pp. 183-185, 1992.

[293] G. J. Monkman and P. M. Taylor, "Memory foams for robot grippers," in *5th International Conference on Advanced Robotics*, Pisa, Italy, June 1991.

[294] R. E. Pelrine, R. D. Kornbluh and J. P. Joseph, "Electrostriction of polymer dielectrics with compliant electrodes as a means of actuation," *Sensors and Actuators A: Physical*, vol. 64, no. 1, pp. 77-85, 1998.

[295] K. Asano, F. Hatakeyama and K. Yatsuzuka, "Fundamental study of an electrostatic chuck for silicon wafer handling," *IEEE Transactions on Industry Applications*, vol. 38, no. 3, pp. 840-845, 2002.

[296] H. Wang, A. Yamamoto and T. Higuchi, "A crawler climbing robot integrating electroadhesion and electrostatic actuation," *International Journal of Advanced Robotic Systems*, vol. 11, no. 191, pp. 1-11, 2014.

[297] H. Prahlad, R. Pelrine, S. Stanford, J. Marlow and R. Kornbluh, "Electroadhesive robots—wall climbing robots enabled by a novel, robust, and electrically controllable adhesion technology," in *IEEE International Conference on Robotics and Automation*, Pasadena, CA, USA, May 2008.

[298] G. Monkman, "Electroadhesive microgrippers," *Industrial Robot: An International Journal*, vol. 30, no. 4, pp. 326-330, 2003.

[299] Grabit Inc., "Products," Available: http://grabitinc.wpengine.com/products/#panelgrippers [Accessed September 2015].

[300] S. Song and M. Sitti, "Soft grippers using micro-fibrillar adhesives for transfer printing," *Advanced Materials*, vol. 26, no. 28, pp. 4901–4906, 2014.

[301] M. P. Murphy, B. Aksak and M. Sitti, "Gecko-inspired directional and controllable adhesion," *Small*, vol. 5, no. 2, pp. 170–175, 2009.

[302] S. Kim, M. Spenko, S. Trujillo, B. Heyneman, D. Santos and M. R. Cutkosky, "Smooth vertical surface climbing with directional adhesion," *IEEE Transactions on Robotics*, vol. 24, no. 1, pp. 65-74, 2008.

[303] A. Parness, D. Soto, N. Esparza, N. Gravish, M. Wilkinson, K. Autumn and M. Cutkosky, "A microfabricated wedge-shaped adhesive array displaying gecko-like dynamic adhesion, directionality and long lifetime," *Journal of The Royal Society Interface*, vol. 6, no. 41, pp. 1223-1232, 2009.

[304] S. A. Suresh, D. L. Christensen, E. W. Hawkes and M. Cutkosky, "Surface and shape deposition manufacturing for the fabrication of a curved surface gripper," *Journal of Mechanisms and Robotics*, vol. 7, no. 2, pp. 021005-1-021005-7, 2015.

[305] E. W. Hawkes, D. L. Christensen, A. K. Han, H. Jiang and M. R. Cutkosky, "Grasping without squeezing: shear adhesion gripper with fibrillar thin film," in *IEEE International Conference on Robotics and Automation*, Seattle, WA, USA, May 2015.

[306] K. Autumn and A. M. Peattie, "Mechanisms of adhesion in geckos," *Integrative and Comparative Biology*, vol. 42, no. 6, pp. 1081-1090, 2002.

[307] G. Monkman, P. Taylor and G. Farnworth, "Principles of electroadhesion in clothing robotics," *International Journal of Clothing Science and Technology*, vol. 1, no. 3, pp. 14-20, 1989.

[308] I. D. Johnston, D. K. McCluskey, C. K. L. Tan and M. C. Tracey, "Mechanical characterization of bulk Sylgard 184 for microfluidics and microengineering," Journal of Micromechanics and Microengineering, vol. 24, no. 3, pp. 035017-1-035017-7, 2014.

[309] H. A. Pohl, "Some effects of nonuniform fields on dielectrics," *Journal of Applied Physics*, vol. 29, no. 8, pp. 1182-1188, 1958.

[310] A. D. Moore, *Electrostatics and its applications*, New York: Wiley, 1973.

[311] A. Yamamoto, T. Nakashima and T. Higuchi, "Wall climbing mechanisms using electrostatic attraction generated by flexible electrodes," in *IEEE International Symposium on Micro-Nano Mechatronics and Human Science*, Nagoya, Japan, November 2007.

[312] R. Liu, R. Chen, H. Shen and R. Zhang, "Wall climbing robot using electrostatic adhesion force generated by flexible interdigital electrodes," *International Journal of Advanced Robotic Systems*, vol. 10, no. 36, pp. 1-9, 2013.

[313] V. Sabermand, Y. Hojjat and M. Hasanzadeh, "Study of parameters affecting the electrostatic attractions force," *International Journal of Electrical, Computer, Electronics and Communication Engineering*, vol. 8, no. 11, pp. 1702-1705, 2014.

[314] K. Yatsuzuka, F. Hatakeyama, K. Asano and S. Aonuma, "Fundamental characteristics of electrostatic wafer chuck with insulating sealant," *IEEE Transactions on Industry Applications*, vol. 36, no. 2, pp. 510-516, 2000.

[315] F. Ilievski, A. D. Mazzeo, R. F. Shepherd, X. Chen and G. M. Whitesides, "Soft robotics for chemists," *Angewandte Chemie International Edition*, vol. 50, no. 8, pp. 1890–1895, 2011.

[316] D. Petković, N. D. Pavlović, S. Shamshirband and N. B. Anuar, "Development of a new type of passively adaptive compliant gripper," *Industrial Robot: An International Journal*, vol. 40, no. 6, pp. 610-623, 2013.

[317] R. Deimel and O. Brock, "A novel type of compliant and underactuated robotic hand for dexterous grasping," *The International Journal of Robotics Research*, DOI: 10.1177/0278364915592961.

[318] O. A. Araromi, I. Gavrilovich, J. Shintake, S. Rosset, M. Richard, V. Gass and H. Shea, "Rollable multisegment dielectric elastomer minimum energy structures for a deployable microsatellite gripper," *IEEE/ASME Transactions on Mechatronics*, vol. 20, no. 1, pp. 438 - 446, 2015.

[319] S. Shian, K. Bertoldi and D. R. Clarke, "Dielectric elastomer based “grippers” for soft robotics," *Advanced Materials*, 2015 (in print).

[320] D. Ruffatto III, J. Shah and M. Spenko, "Optimization of electrostatic adhesives for robotic climbing and manipulation," in *ASME 2012 International Design Engineering Technical Conferences and Computers and Information in Engineering Conference*, Chicago, IL, USA, August 2012.

[321] D. Ruffatto III, J. Shah and M. Spenko, "Increasing the adhesion force of electrostatic adhesives using optimized electrode geometry and a novel manufacturing process," *Journal of Electrostatics*, vol. 72, no. 2, pp. 147–155, 2014.

[322] A. V. Mamishev, K. Sundara-Rajan, F. Yang, Y. Du and M. Zhan, "Interdigital sensors and transducers," *Proceedings of the IEEE*, vol. 92, no. 5, pp. 808-845, 2004.

[323] D. Floreano and R. J. Wood, "Science, technology and the future of small autonomous drones," *Nature*, vol. 521, no. 7553, pp. 460-466, 2015.

[324] A. Vankov, P. Huie, M. Blumenkranz and D. Palanker, "Electro-adhesive forceps for tissue manipulation," in *Proc. SPIE*, Bellingham, WA, USA, July 2004.

[325] H.-T. Lin, G. G. Leisk and B. Trimmer, "GoQBot: a caterpillar-inspired soft-bodied rolling robot," *Bioinspiration & Biomimetics*, vol. 6, no. 2, pp. 026007-1-026007-14, 2011.

[326] R. F. Shepherd, F. Ilievski, W. Choi, S. A. Morin, A. A. Stokes, A. D. Mazzeo, X. Chen, M. Wang and G. M. Whitesides, "Multigait soft robot," *Proceedings of the National Academy of Sciences of the United States of America*, vol. 108, no. 51, pp. 20400–20403, 2011.

[327] R. Chen, R. Liu, J. Chen and J. Zhang, "A gecko inspired wall-climbing robot based on electrostatic adhesion mechanism," in *IEEE International Conference on Robotics and Biomimetics*, Shenzhen, China, December 2013.

[328] J. Germann, M. Dommer, R. Pericet-Camara and D. Floreano, "Active connection mechanism for soft modular robots," *Advanced Robotics*, vol. 26, no. 7, pp. 785-798, 2012.

[329] E. P. Popov, *Engineering Mechanics of Solids*, 2nd ed., Upper Saddle River, NJ: Prentice Hall, 1998.

[330] G. A. Holzapfel, *Nonlinear Solid Mechanics: A Continuum Approach for Engineering*, Chichester: Wiley, 2000.

Jun Shintake

shintakejun@gmail.com

EDUCATION

Ph.D. in Microsystems and Microelectronics, 2015
École Polytechnique Fédérale de Lausanne, Lausanne, Switzerland
Thesis title: *Functional Soft Robotic Actuators Based on Dielectric Elastomers*

M.Eng. in Mechanical Engineering, 2011
University of Electro-Communications, Tokyo, Japan
Thesis title: *Development of Underwater Robots Using PZT Fiber Composites*

B.Eng. in Mechanical Engineering, 2009
University of Electro-Communications, Tokyo, Japan
Thesis title: *Precision Improvement of Gear Measurement Machine*

SKILLS

Simulation: ANSYS, COMSOL
Programming: MATLAB, C, C#, Arduino
Other: SolidWorks, Illustrator, Latex, Office

LANGUAGES

Japanese: Native
English: Fluent

PUBLICATIONS

Journal Papers

- **J. Shintake**, S. Rosset, B. Schubert, D. Floreano and H. Shea, "Versatile soft grippers with intrinsic electroadhesion based on multifunctional polymer actuators," *Advanced Materials*, DOI: 10.1002/adma.201504264.
- **J. Shintake**, S. Rosset, B. E. Schubert, D. Floreano and H. Shea, "A foldable antagonistic actuator," *IEEE/ASME Transactions on Mechatronics*, vol. 20, no. 5, pp. 1997-2008, 2015.
- S. Araromi, I. Gavrilovich, **J. Shintake**, S. Rosset and M. Richard, V. Gass and H. Shea, " Rollable multisegment dielectric elastomer minimum energy structures for a deployable microsatellite gripper," *IEEE/ASME Transactions on Mechatronics*, vol. 20, no. 1, pp. 438-446, 2015.
- S. Rosset, S. Araromi, **J. Shintake** and H. Shea, "Model and design of dielectric elastomer minimum energy structures," *Smart Materials and Structures*, vol. 23, no. 8, pp. 085021-1-085021-12, 2014.

Conference Papers

- **J. Shintake**, B. Schubert, S. Rosset, H. Shea and D. Floreano, "Variable stiffness actuator for soft robotics using dielectric elastomer and low-melting-point alloy," in *IEEE/RSJ International Conference on Intelligent Robots and Systems*, Hamburg, Germany, October 2015.

- **J. Shintake**, S. Rosset, B. Schubert, D. Floreano and H. Shea, "DEA for soft robotics: 1-gram actuator picks up a 60-gram egg," in *Proc. SPIE*, San Diego, CA, USA, March 2015.
- S. Araromi, I. Gavrilovich, **J. Shintake**, S. Rosset and H. Shea, "Towards a deployable satellite gripper based on multisegment dielectric elastomer minimum energy structures," in *Proc. SPIE*, San Diego, CA, USA, March 2014.
- **J. Shintake**, S. Rosset, D. Floreano and H. Shea, "Effect of mechanical parameters on dielectric elastomer minimum energy structures," in *Proc. SPIE*, San Diego, CA, USA, March 2013.
- W. Zhao, **J. Shintake**, A. Ming and M. Shimojo, "Structural design and dynamic analysis of robotic fish with piezoelectric fiber composite," in *IEEE 13th International Conference on Mechatronics / 9th France-Japan and 7th Europe-Asia Congress on Mechatronics*, Paris, France, November 2012.
- **J. Shintake**, A. Ming and M. Shimojo, "A novel propulsion method of flexible underwater robots," in *IEEE/RSJ International Conference on Intelligent Robots and Systems*, San Francisco, CA, September 2011.
- **J. Shintake**, A. Ming and M. Shimojo, "Development of flexible underwater robots with caudal fin propulsion," in *IEEE/RSJ International Conference on Intelligent Robots and Systems*, Taipei, Taiwan, October 2010.
- **J. Shintake**, A. Ming and M. Shimojo, "Development of Underwater Robots using Piezoelectric Fiber Composite -Diversification of Propulsion Movement by Single Fin Structure-," in *JSME/RMD International Conference on Advanced Mechatronics*, Osaka, Japan, October 2010. (Best Paper Nomination Finalist)

Conference Abstracts and Posters

- **J. Shintake**, S. Rosset, B. E. Schubert, D. Floreano and H. Shea, "Dielectric Elastomer Actuators for soft-grasping," in *International Workshop on Soft Robotics and Morphological Computation*, Centro Stefano Franscini (CSF), Monte Verità, Ascona, Switzerland, July 2013. (Best Contribution Award)
- **J. Shintake**, S. Rosset, D. Floreano and H. Shea, "A soft robotic actuator using dielectric minimum energy structures," in *International Conference on Electromechanically Active Polymer (EAP) transducers & artificial muscles*, Potsdam, Berlin, Germany, May 2012. (Best Poster Award)